EPFL

Thèse n° 7480

Structural architecture of the Neuronal-Glial-Vascular system

Présentée le 11 mars 2021

Centres pour la recherche
Projet Bluebrain
Programme doctoral en neurosciences

pour l'obtention du grade de Docteur ès Sciences

par

Eleftherios ZISIS

Acceptée sur proposition du jury

Prof. M. Herzog, président du jury
Prof. H. Markram, Dr D. Keller, directeurs de thèse
Dr H. Cuntz, rapporteur
Prof. S. Siegert, rapporteuse
Prof. D. Ghezzi, rapporteur

École
polytechnique
fédérale
de Lausanne

2021

To my parents and sister, for their love and support throughout my life.
To my amazing wife, Lida, whose unyielding patience, faith and encouragement have motivated me to complete this research.

Acknowledgements

First and foremost, I would like to thank Henry Markram, my thesis advisor, for giving me the opportunity to realize my PhD in the Blue Brain Project and for suggesting this beautiful and exciting topic, which kept me hooked for all these years. His feedback, insights, and ideas illuminated the path that lead to this thesis.

I am indebted to Julian Shillcock for receiving me in his team when I was a mere student assistant back in the day and for proposing a Ph.D. subject. Thank you Julian for the water-cooler conversations during coffee breaks before BBP moved to Geneva, but also for all the neat discussions to this day.

I am deeply grateful to Daniel Keller, my co-director, whose supervision helped me step-by-step reach my Ph.D. completion. Thank you Dan for being there throughout this journey, reading my unintelligible texts, and stoically listening to my numerous issues with code, analysis and writing. I would also like to extend my deepest gratitude to Kathryn Hess, my mentor and second co-director, for her support and making sure that everything goes like clockwork.

I feel the need to express my gratitude to Marc-Oliver Gewaltig, whose valuable advice greatly improved my presentations. From whom I learned how to build a story and convey the right message. I would also like to thank Rajnish Ranjan for helping me organize my candidacy presentation, and for his valuable biological insights and experience he shared with me.

I would like to thank Nicolas Antille, not only for his beautiful contributions to the visualization of the NGV, but for showing genuine interest in neuroscience and in how things should be right, not just look that way. Thank you Nicolas for the motivating discussions that gave rise to new, wonderful ideas and for making these mind-blowing posters for SfN during my first years in my PhD. I would also like to extend my thanks to the entire visualization team (Marwan Abdellah, Alessandro Foni, Cyrille Favreau,

Grigory Chevtchenko) to produce brilliant illustrations and movies in support of my work.

I cannot thank enough Mike Gevaert, Thomas Delemontex, and Arseny Povolotskiy for both their software design ideas and engineering work, which reshaped an NGV prototype into a maintainable production tool. For teaching me all the best practices in programming and for the countless hours you have spent on my code reviews. Thank you Mike for finding the time to answer all of my questions; I would still be struggling with git without you. Thank you, Thomas, for putting up with me and my strong opinions on the design of the NGV's user api.

Special thanks to Berat Denizdurduran for the discussions on various mathematical and algorithmic problems. Many a time we had stayed late, scribbling on the whiteboard behind Berat's desk, careful not to erase the super long derivations that lived there.

I would like to express my deep gratitude to the HPC team, the hard work of which made my research and contributions possible. Thank you Adrien Devresse, Tristan Carel, Pramod Kumbhar, Fernando Pereira, and Matthias Wolf, for personally helping me in times of need. And of course I cannot thank the HPC team without thanking James King, the king of simulation. His in-depth knowledge and skills pave the road for functional large scale models of the NGV.

Many thanks to my colleagues in BBP (Nancy Chalimourda, Taylor Newton, Jay Coggan, Michael Reimann, Shrikanth Ramaswamy, Werner Van Geit, Christina Colangelo, Csaba Ero, Luc Guyot, Danny Dyer, Alexis Arnaudon, Stephanie Battini) and LNMC (Rodrigo Perin, Mirjia Herzog, Julie Meystre) for all the good moments! Thank you Giueseppe Chindemni and Armando Romani for the valuable Italian lessons. I have never learned so fast a language before.

My deepest thanks and love to my parents and sister, who always believed in me. Time flies, and before you know it, you are away from home for almost ten years. However, they have always been by my side, and will always be. I also look forward to the day that my sister, Maria, will beat me in chess. Many thanks to all my friends outside BBP, who kept me sane all these years.

Progress in research is made by standing on the shoulders of giants. Thank you Lida for all these weird questions that went both ways. All these long walks discussing and exploring all sorts of ideas were invaluable. Without the faith you had put in me and your support, I would never have completed this work.

Abstract

Brain functionality relies on the neuronal-glial-vascular (NGV) ensemble for energy support. However, the details of the complex biological mechanisms involved in these processes and the microscopic interactions between these three components are not yet fully understood. Astrocytes, an essential component of the NGV ensemble, extend ramified processes to the vasculature and to neuronal synapses to provide neuronal energy support, homeostatic control, and multi-directional signaling with the vasculature, neurons, and neighboring astrocytes. As key links between the components of the NGV circuitry, the astrocytes are essential for drug delivery in the brain and are involved in the progression of neurodegenerative diseases. Therefore, comprehensive models of the neuronal-glial-vascular (NGV) ensemble are essential for understanding the role of astrocytes in the formation and function of the complex networks within the brain and its pathological conditions. A complete computational model of this ensemble has not yet been developed.

This thesis presents the first model of a data-driven digital reconstruction of the neuronal-glial-vascular (NGV) ensemble at a micrometer anatomical resolution. Combining the sparse literature data and the few available detailed biological reconstructions, I have computationally generated the structural architecture of a neocortical NGV circuit that forms a functional column of the juvenile rat neocortex and consists of neurons, protoplasmic astrocytes, and the microvasculature, including their pairwise connectivities. This data-driven approach allows for incremental refinement as more experimental data become available, new biophysical models get published, and new questions arise. The NGV circuit is validated against a plethora of literature sources to ensure its biological fidelity: it successfully reproduces the spatial organization of the astrocytes, their morphological characteristics as well as their volume occupancy, and the overlap with their neighbors.

The power of the computational model of NGV lies in its ability to serve as a framework for addressing long-standing questions that cannot be experimentally investigated due to

the complexity of the microscopic systems and the limitations of current techniques to observe all components simultaneously. In this thesis, I have performed experiments to investigate why astrocytes acquire their particular shapes, the organizational principles of NGV that lead to the observed biological network architectures, and the effect of astrocytic density on endfoot organization. The circuit's structural analysis showed that astrocytes optimize their positions and spacing from each other to provide the vasculature with a uniform coverage for trophic support and signaling. By increasing the density of astrocytes in NGV circuits, I discovered a limit in astrocyte's ability to make perivascular projections because of the vascular spatial occupancy, which constrains the extent of astrocyte morphology. Thus, their role in linking vasculature to neurons constrains their organization via the proportional relationship of density and microdomain shrinkage due to contact spacing.

By addressing these questions, I demonstrated how this model can serve as an exploratory tool that provides a window into the complexity of the NGV architecture.

Abstract

Le cerveau repose sur le système neuronal-glial-vasculaire (NGV) afin d'assurer son apport énergétique. Malgré cela, le détail des mécanismes biologiques complexes impliqués dans ces processus ainsi que les interactions microscopiques liant ces trois composants sont encore mal compris de nos jours.

Les astrocytes, composant essentiel de l'ensemble NGV, étendent des protubérances ramifiées au système vasculaire ainsi qu'aux synapses neuronales afin de fournir un soutien énergétique aux neurones. Ils permettent aussi un contrôle homéostatique ainsi qu'une transmission multidirectionnelle avec le système vasculaire, les neurones et les astrocytes voisins. En tant que liens clé entre les différents composants du circuit NGV, les astrocytes ont un rôle particulièrement important pour l'administration de médicaments dans le cerveau et sont impliqués dans la progression des maladies neurodégénératives. Par conséquent, des modèles complets de l'ensemble neuronal-glial-vasculaire (NGV) sont essentiels afin de comprendre le rôle des astrocytes dans la formation et le fonctionnement des réseaux complexes de cellules composant le cerveau ainsi que ses conditions pathologiques. Cependant, à ce jour, aucun modèle complet de cet ensemble n'a été développé. Cette thèse présente le premier modèle de reconstruction numérique de l'ensemble neuronal-glial-vasculaire (NGV) basé sur des données à une résolution anatomique micrométrique.

En combinant les données de la littérature et les rares reconstructions biologiques détaillées disponibles, j'ai pu générer un modèle numérique de l'architecture structurelle d'un circuit néocortical NGV. Ce circuit synthétique reproduit une colonne fonctionnelle du néocortex du rat juvénile et se compose de neurones, d'astrocytes protoplasmiques, d'une micro-vascularisation ainsi que de leurs connections respectives. Il est à noter qu'un des avantages de cette approche axée sur les données, est qu'elle permet un affinement progressif du modèle à mesure que de nouvelles données expérimentales deviennent disponibles, que de nouveaux modèles biophysiques sont publiés et que de nouvelles questions se posent. Afin d'assurer la fidélité biologique du circuit NGV produit, celui-ci a

été confronté et comparé à de nombreuses sources littéraires. Il reproduit notamment avec fidélité les caractéristiques essentielles des astrocytes : leur organisation spatiale, leurs caractéristiques morphologiques, leur occupation volumique ainsi que le chevauchement entre astrocytes voisins. Une des forces de ce modèle numérique réside aussi en sa capacité à servir de cadre pour répondre à des questions plus larges, parfois anciennes, qui ne peuvent pas être étudiées expérimentalement notamment en raison de la complexité des systèmes microscopiques, la difficulté pour les techniques biologiques actuelles à observer tous les composants et leurs interactions simultanément.

Dans cette thèse, j'ai aussi réalisé plusieurs études dont le but est de chercher à comprendre quels sont les mécanismes qui poussent les astrocytes à acquérir leurs formes particulières, à comprendre les principes organisationnels du système NGV menant aux architectures de réseaux biologiques observées et à estimer l'effet de la densité astrocytaire sur l'organisation des "endfeet" liens entre les astrocytes et le système vasculaire. En répondant à ces questions, je montre ainsi en quoi ce modèle peut être utiliser comme un puissant outil d'exploration, offrant une vue sur la complexité de l'architecture NGV.

Contents

List of Figures

List of Tables

1

Introduction

> *"Nature uses only the longest threads to weave her patterns, so each small piece of her fabric reveals the organization of the entire tapestry."*
>
> – Richard P. Feynman

As these lines are being read our brain engages neurons and glia to perform information processing, which eventually increases the neuronal metabolic energy demand leading to local increases and decreases in the diameter of the proximal vessels (Gordon et al., 2007) to balance out demand. The complex structural organization of the two dominant cell classes in the brain, neurons and glia, allows us to think and go on with our daily routines is known as the neuronal-glial-vascular (NGV) system.

Neurons, the principal subjects of neuroscientific research, are electrically excitable cells composed of the soma, dendrites, and axons (Fig. 1.1A). Dendrites collect both excitatory and inhibitory signals, which are integrated into the axon hillock. When the membrane potential exceeds a certain threshold, an action potential is created, which is electro-chemically transmitted across the neuron's axon to other neurons via synapses. Neuronal synapses are typically formed between the postsynaptic dendritic spines and the presynaptic axonal boutons. They are classified into excitatory and inhibitory synapses depending on the effect of the neurotransmitter that is released. The most common excitatory and inhibitory neurotransmitters are glutamate and γ-aminobutyric acid (GABA) respectively.

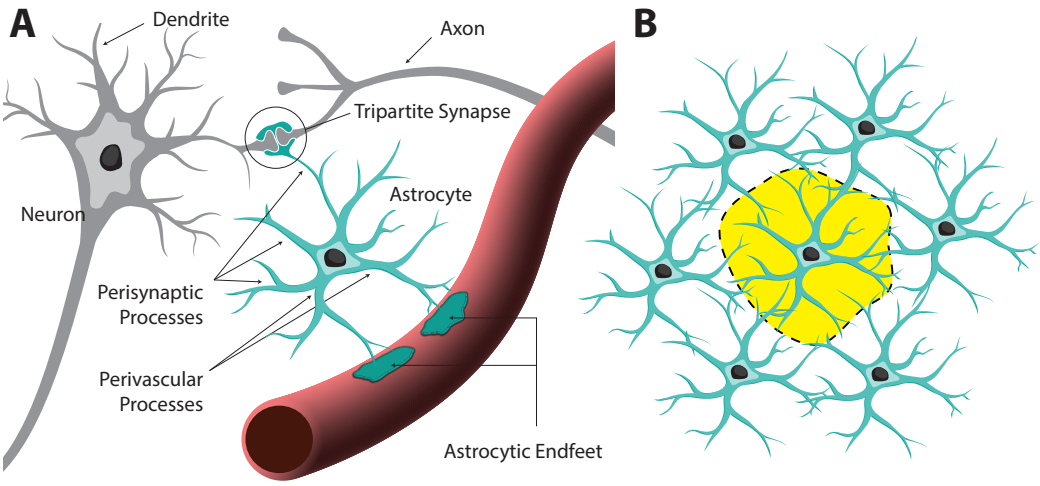

Figure 1.1 Overview of the neuronal-glial-vascular architecture system. (a) Astrocytes contact and wrap around synapses and project their perivascular processes to the surface of the vasculature, where they form endfeet. (b) Astrocytes form anatomically exclusive domains with minimal overlap with their neighbors. (c) In-silico or digital morphologies are tree structures that connect to a central soma geometry.

At the time of their discovery, glia were thought to be merely the "glue" of the brain, a belief that inspired their naming by pathologist Rudolf Virchow (Virchow, 1859). Yet, over the past decade research has challenged earlier dogma and shown the nature of glia to be as intricate as that of their well-studied neighbors, the neurons. Astrocytes are classified into two main categories, fibrous and protoplasmic, according to their morphological phenotype and anatomical location. This classification is usually attributed to Ramón y Cajal, however the distinction had already been observed by neuroanatomists that preceded him, such as Andriezen (1893) and Kölliker (1896). Fibrous astrocytes extend straight processes, and they are mainly located in the white matter, while protoplasmic astrocytes possess spongiform phenotypes and are mainly located in the gray matter. In the CNS, there are three types of glia: astrocytes, oligodendrocytes, and microglia. This work focuses on the gray matter and the most well studied and functionally important glial type: the protoplasmic astrocyte.

Protoplasmic astrocytes radially extend between five and ten primary processes (Calì et al., 2019; Damoiseaux and Greicius, 2009; Di Benedetto et al., 2016; Moye et al., 2019; Tsai et al., 2009; Wilhelmsson et al., 2006), which ramify progressively into finer and finer branches, uniformly occupying their entire spatial extent (Bushong et al., 2002, 2004; Ogata and Kosaka, 2002), which can reach an edge-to-edge distance up to 60 µm (Medvedev et al., 2014; Ogata and Kosaka, 2002). This spongiform morphology forms anatomically exclusive regions with neighboring astrocytes, covering the entire

neuropil in a tiling organization that is known as microdomains (Bushong et al., 2002, 2004)(Fig. 1.1B), with six to fifteen neighbors each (Xu et al., 2010). They form a thin overlapping interface in their periphery where they adhere to their neighbors, establishing sub-cellular highways via process-to-process gap junction channel connections (CX43, CX30) (Rohlmann and Wolff, 1996; Wolff et al., 1998). Neighboring microdomains form a minimally overlapping interface of interdigitating processes that cover approximately 5% of the neighboring astrocytic territories and has been observed across brain regions and species (Bushong et al., 2002, 2004; Halassa et al., 2007a; Hara et al., 2017; Khakh and Sofroniew, 2015; Nimmerjahn et al., 2004; Sofroniew and Vinters, 2010). Fine astrocytic leaflet-like processes, known as perisynaptic processes (PAPs), wrap around the presynaptic and postsynaptic nerve terminals of synapses forming tripartite units (Araque et al., 1999; Halassa et al., 2007a) and it has been reported that one rodent astrocyte is in contact with as many as 100,000 synapses (Bushong et al., 2002). One to five thick processes project to capillaries, arterioles and venules, apposing firmly on their adluminal surface (Abbott et al., 2006; Schmechel and Rakic, 1979), forming rosette-like structures (Kacem et al., 1998), which cover more than 60% of the vasculature surface (Korogod et al., 2015). Astrocytic endfeet, pericytes, the endothelial tube, and its basement membrane are the main components of the blood-brain-barrier (BBB) composition. The BBB combined with astrocytes and neurons is known as the neurovascular unit (Serlin et al., 2015; Woolsey et al., 1996).

At the synapse level, protoplasmic astrocytes maintain synaptic fidelity by preventing neurotransmitter accumulation and spillover. Glutamate or GABA, after being released from the presynaptic terminal, they are quickly cleared from the interstitial space (Schousboe et al., 2013) by PAPs, which convert them into the non-neuroactive glutamine (Sonnewald and Kondziella, 2003; Waagepetersen et al., 2005) and then shuttle them back to the presynaptic terminal where they are transformed into glutamate (glutamine synthetase pathway; Van den Heuvel et al. (2004)) in glutamatergic neurons or further metabolized into GABA (glutamate decarboxylase pathway; Martin and Rimvall (1993)) in GABAergic neurons. Disruption or abnormal function of this mechanism has been reported in a number of disorders, including epilepsy (Petroff et al., 2002), amyotrophic lateral sclerosis (Rothstein et al., 1992, 1995) and Alzheimer's disease (Hynd et al., 2004; Tannenberg et al., 2004). Astrocytes also regulate the excess K^+ released by neuronal activity, a process known as K^+ buffering, which is achieved via two main mechanisms: K^+ uptake and K^+ spatial buffering (Amédée et al., 1997). K^+ uptake is achieved by temporary uptake of K^+ by adjacent astrocytes, accompanied by the influx of anions (e.g. Cl^-) and/or the efflux of cations (e.g. Na^+) to preserve electroneutrality, and subsequent

release of K^+ back into the extracellular space (Henn et al., 1972; Hertz, 1965). K^+ spatial buffering is the distribution of K^+ to far regions with low K^+ concentration via the astrocytic syncytium (Orkand et al., 1966), which has the tendency to remain isopotential due to the gap junctional coupling of tiling microdomains (Ma et al., 2016). Disruption in the normal K^+ clearance mechanisms has been linked with disorders such as Alzheimer's disease (Olabarria et al., 2010), Rett syndrome (Turovsky et al., 2015) and Huntigton's disease (Tong et al., 2014).

Unlike neurons, astrocytes are not electrically excitable cells. They exhibit a different form of excitability, which relies on the dynamics of the free cytosolic calcium (Cornell-Bell et al., 1990). For instance, at glutamatergic synapses, the release of glutamate from the pre-synaptic terminal activates G-protein-coupled receptors in the astrocytic membrane (Panatier et al., 2011; Wang et al., 2006). This activates phospholipase C (PLC) and the generation of inositol triphosphate (IP_3), which induces Ca^{2+} mobilization from ER stores by binding to IP_3R receptors (Golovina and Blaustein, 2000; Sheppard et al., 1997). IP_3 may inter-cellularly transport to neighboring astrocytes via gap junctions, and activate IP_3Rs and Ca^{2+} release, which may regenerate IP_3 (Ullah et al., 2006) and continue the cycle. Increases of astrocytic Ca^{2+} concentration have been found to trigger glutamate release to the extracellular space (Bezzi et al., 1998; Parpura et al., 1994). In general, astrocytic secretion of gliotransmitters (amino acids, peptides and ATP) is achieved by exocytosis (Bergersen et al., 2012; Bezzi et al., 2004; Jorgačevski et al., 2017), diffusion through connexin hemichannels and pannexins (Bergersen et al., 2012; Stout et al., 2002) and a wide variety of transporters (Verkhratsky and Zorec, 2020). With all this sophisticated signalling machinery at their disposal, involvement of astrocytes in synaptic plasticity is inescapable (Allen and Barres, 2005; López-Hidalgo and Schummers, 2014).

Signaling at the tripartite synapse and throughout the syncytium are not the only signaling systems that astrocytes mediate. ICWs can propagate through the perivascular process to the endfoot compartment in which Ca^{2+} may generate arachidonic acid (AA) from phospholipase A_2 (PLA_2) (Farooqui et al., 1997). AA may subsequently be converted to epoxyeicosatrienoic acids (EETs) and prostagladins (PGs), which along with the release of K^+ contribute to vasodilation (Mishra et al., 2011). AA may also diffuse into smooth muscle cells or pericytes and be converted to 20-HETE to induce vasoconstriction (Imig et al., 1996). Increased local metabolic demand due to neuronal activity results in local blood flow increase (Bonvento et al., 2002). Glucose crosses the BBB and into the astrocytic endfeet via glucose transporters (GLUTs; Leino et al. (1997))

and is rapidly distributed throughout the astrocytic syncytium (Beckmann et al., 2019; Parpura et al., 2012). Glucose may either be stored as glycogen for future metabolic demands (Brown, 2004; Brown and Ransom, 2015) or be converted to lactate, which is then shuttled into neurons via monocarboxylate transporters (MCTs; Halestrap and PRICE (1999)). Neurons then convert it to pyruvate and subsequently to ATP in the mitochondria (Magistretti and Allaman, 2015; Magistretti et al., 1999). This energy provision model is known as the astrocyte-neuron lactate shuttle hypothesis (ANLSH; Pellerin and Magistretti (1994)). Due to the critical role of the BBB and the neurovascular unit in brain, disruption or disintegration of the neurovascular structural integrity, such as changes in vasculature coverage and BBB disintegration, have been linked with disorders such as major depressive disorder (Najjar et al., 2013; Rajkowska et al., 2013; Rial et al., 2016) and Alzheimer's disease (Zlokovic, 2011).

These are some of the key physiological mechanisms of NGV function, driven by the anatomical organization of the NGV system. There are numerous studies on the multi-directional signaling among neurons, astrocytes, and the vasculature; however, the NGV interactions are still poorly understood. Brain homeostasis, NGV synaptic modulation and plasticity, energy provision and on-demand support, and high-level information processing requires a detailed understanding of the structural NGV foundations that is currently missing. Studying each mechanism by dissociating structural and functional components provide only a restricted view of the pathology in question. Neurodegenerative disorders arise from the interaction of multiple pathophysiological mechanisms on the network level, rather than isolated processes in a specific locale (Braak and Braak, 1997). However, large-scale analysis of connectivity is difficult to do, limited by the resolution of the equipment and the quality of the experiment (Sharma et al., 2009). Thus, computational models of brain anatomy and physiology may assist in the detailed understanding of the structural and functional foundations that give rise to the observed healthy and pathological epiphenomena.

Computational neuroscience has made astounding progress since the creation of the first data-driven biological neuronal model in the 1950s by Hodgkin and Huxley (Hodgkin A. L. and Huxley A. F., 1952) and the subsequent introduction of multi-compartmental modeling of digitally-reconstructed neuronal morphologies. A digital reconstruction of a morphology is a 3D trace, made with computer-microscope interfaces or from skeletonization of image stacks (Donohue and Ascoli, 2011; Halavi et al., 2012). The branching morphology is represented as a sequence of segments (truncated cones) that capture the X, Y, Z coordinates, cross-sectional diameter, and connectivity links. Biologically realis-

tic morphologies allow for compartmental biophysical models, capturing the non-linear dynamics arising from the distribution of ion channels throughout their compartments. The branching structure of neuronal morphologies is believed to play an important role in the computational tasks of the neuronal networks (Cuntz et al., 2007; van Elburg and van Ooyen, 2010). Similarly, the branching topology and geometry of astrocytic morphologies are important for driving the propagation of calcium-induced waves that have been found to contribute to information processing (Araque et al., 2014; Cornell-Bell et al., 1990; Hamilton and Attwell, 2010; Volterra and Meldolesi, 2005). However, the densely ramified nature of protoplasmic astrocytes leads to digital reconstructions that are but a fraction of the complete morphology, with the most commonly used marker, GFAP, revealing only the main cell skeleton (Kulkarni et al., 2015). Electron microscopy (3DEM), on the other hand, can provide the ultrastructure required for capturing the nanoscopic astrocytic processes but at the cost of low throughput (Calì et al., 2019).

In this thesis, I present a large-scale algorithmic approach with which I generated for the first time the structural architecture of the NGV components in the gray matter of the P14 rat neocortex: 88541 neurons, 14648 protoplasmic and the cerebral microvasculature, including their pairwise connectivities for the P14 rat neocortex at a micrometer anatomical resolution. I used sparse data that is distributed across numerous studies to build a digital reconstruction (see table 2.1 for a summary of model parameters) that is consistent with a vast body of literature and therefore allows reasonable predictions of numbers and locations of astrocytes and astrocytic processes supporting different neurons, spatial domains of astrocytes and their overlapping regions, as well as the number of locations of end-feet connecting to the vasculature by each astrocyte and together. The digital reconstruction of the NGV ensemble provides a resource and foundation for understanding the anatomical principles and geometric constraints for interpretations of their functional role in supporting brain function.

In the first chapter, the NGV circuit building algorithms are presented. The NGV circuit was generated by first populating an existing neuronal circuit (Markram et al., 2015) with the cerebral microvasculature and astrocytic somata, the position and dimensions of which were determined with a novel algorithm that reproduced spatial density and dispersion, avoiding collisions with other somata or the vasculature. The placement model used cortical cell densities from Appaix et al. (2012), nearest neighbor distribution profiles from López-Hidalgo et al. (2016) and soma dimensions distribution was fit from a collection of radii measurements of various studies (Bagheri et al., 2013; Bindocci et al., 2017; Bushong et al., 2004; Calì et al., 2019; Lee et al., 2016; Puschmann et al., 2014). Next,

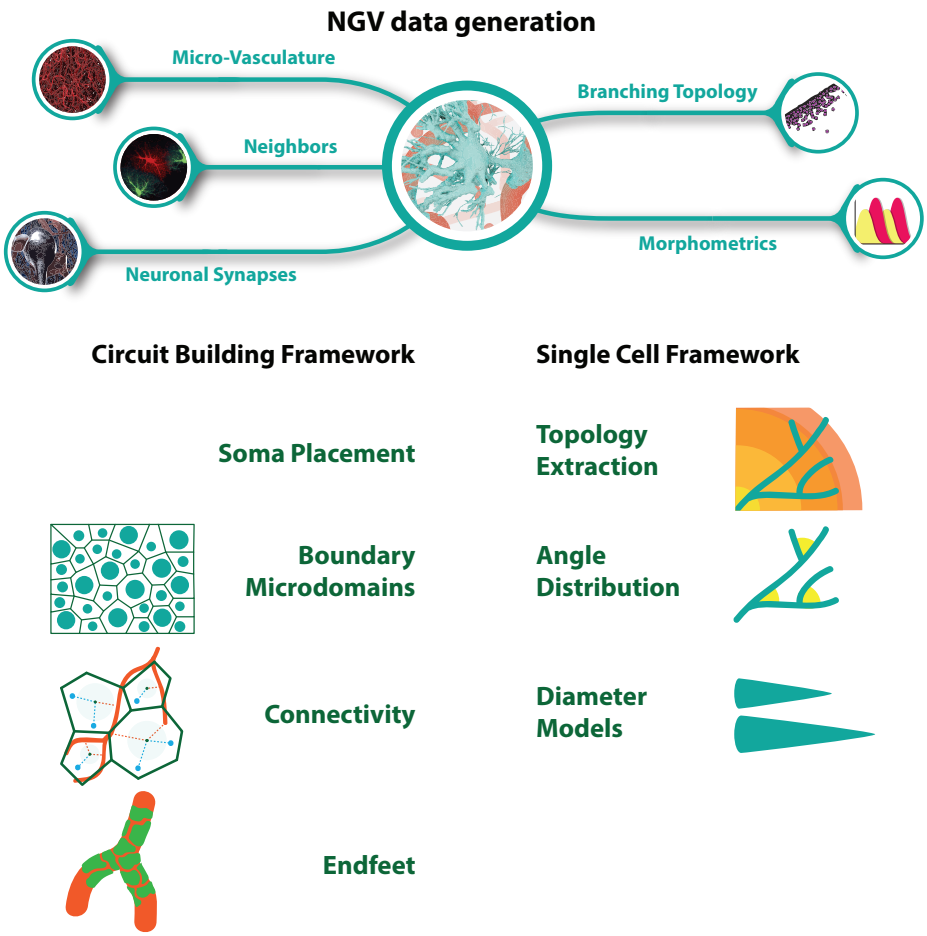

Figure 1.2 NGV Data Framework Components

the cortical space was partitioned into tiling polygons, which represented the astrocytic microdomains, providing an overlapping coverage of the neuropil equal to 5% of each domains volume (Bushong et al., 2002, 2004). Using the microdomains as the reachable space for each astrocyte, I developed methods to create connections to the vasculature (endfeet) and neuronal synapses. The surface geometry of the endfeet connections was then reconstructed by growing 2D meshes on the vasculature's surface. Following the astrocytic morphology synthesis, which is addressed in chapter 2, the syncytial (glial-glial) connectivity was established from the neighboring astrocytes' touches. NGV connectivity model was fit on data of linear density of astrocytic endfeet per vasculature µm (McCaslin et al., 2011), number of endfeet per astrocyte (Calì et al., 2019; Moye et al., 2019) and synapse fraction subsets from Witcher et al. (2007). Endfeet reconstruction target area and thickness distributions were fit on data from Calì et al. (2019) and Wang et al.

(2020). The NGV circuit was validated against numerous literature sources to ensure its biological fidelity. Validation was performed on cell density, dispersion and soma dimensions, microdomain volumes, number of perivascular and perisynaptic branches, soma to soma distance distributions between neurons and astrocytes, endfeet surface area, thickness distribution, and path distance to the vasculature.

In the second chapter, I addressed the issue of the small number of astrocytic reconstructions by developing a novel morphology synthesis algorithm, which combined the branching topology (Kanari et al., 2018) from experimental reconstructions (Calì et al., 2019) with an adaptation of the space colonization algorithm from the work of Runions et al. (2005) on trees. The new algorithm used neuronal synapses as attraction seeds to compute branching directions and all the circuit building's geometrical constraints. Topological and geometric properties were extracted from experimentally reconstructed astrocyte morphologies and subsequently encoded into persistence barcodes. Each barcode contained the start and end path distance of the branch from the neuronal soma, taking into account the branches' topology in the tree. The first step in the synthesis process was the generation of the trees' starting orientations, based on the microdomain orientation and equidistribution of processes. The tip of each section was influenced by three factors: targeting, history, and closest synapse influence. Branching of a growing section was determined from the persistence barcode, which was selected randomly for each tree from the pool of available barcodes, and the branching directions were computed from the attraction of synaptic point cloud, repulsion from closest morphology points in combination to the type of the process. Perivascular processes were additionally attracted by the endfoot target, which dominated their growth until they reached their targets. Finally, radii were distributed on the skeleton trees, encoding the branches' segment volumes, accompanied by a second number, the perimeters, which independently quantified the respective segment surface area (non-conical approximation). The topological synthesis was validated for its ability to synthesize accurate astrocyte morphologies from a single barcode and from a pool of barcodes embedded in the circuit context.

In the last chapter, I explored the predictive power of the NGV circuit by investigating the compositional and organizational principles that govern the underlying biological complexity. First, I analyzed the co-localization of astrocytic somata, large vessels, capillaries, and endfeet targets on the vasculature's surface in search of the dominating element in the endfeet organization. Then, I extracted the total lengths, surface areas, and volumes of the segments of neurons, astrocytes, and the vasculature to explore the composition of geometrical features in the neocortical space and their relationship.

Focusing around the central player of the NGV, the astrocyte, I extracted statistics surrounding its incident connectivities, opening a window to the NGV network organization. Finally, the NGV model exploration was extended to the generation of multiple circuits of increasing densities to investigate the astrocyte numbers effect on the endfeet connectivity and the microdomain packing.

The NGV framework provides the infrastructure to build NGV circuits, the parameters of which may represent different animals, ages, experiments, and pathologies. Thus, it provides a resource for investigating the interactions between neurons, astrocytes, and the vasculature, as a whole, without isolating its functional components and interfaces. A large-scale anatomical reconstruction of such a complex organization has not been possible before; however, it is essential to understand how our brain works in health and disease. Most importantly, the NGV framework enables the simulation of the physiology throughout an entire region, embedded in its actual cortical space with a biologically realistic spatial architecture, and offers the possibility to shed light on unknown questions about the microscopic interactions in the brain.

2

Building the NGV network architecture

2.1 Digital microvascular network skeleton and surface meshing

A digital reconstruction of a rat cerebral vasculature dataset was produced by Reichold et al. (2009). Cylindrical blocks of the rat's somatosensory cortex vasculature were scanned using synchrotron-based X-ray tomographic imaging at the TOMCAT beamline (Swiss Light Source). High energy beams (20KeV) irradiated the tissue with a resolution of (700 nm), resulting in grayscale image stacks, which were segmented into binary images and subsequently converted into midlines (skeleton) using custom software for artifact removal and skeletonization.

The dataset consists of point samples linked together with edges (Fig. 2.1A). Each point is acquired with a diameter which represents the width of the cross section. Two consecutive points constitute a segment in the morphology (Fig. 2.1B), and consecutive segments form a morphological section (Fig. 2.1B). There are two representations of the skeleton dataset that are encountered: The point representation, in which a node is a single point in the morphology and an edge links two points, and the section representation, in which an entire section is clustered into a node and the edges linking sections together. Depending on the nature of the algorithm one or the other representation may be favorable for efficiency or memory consumption. Geometric discontinuities due to the

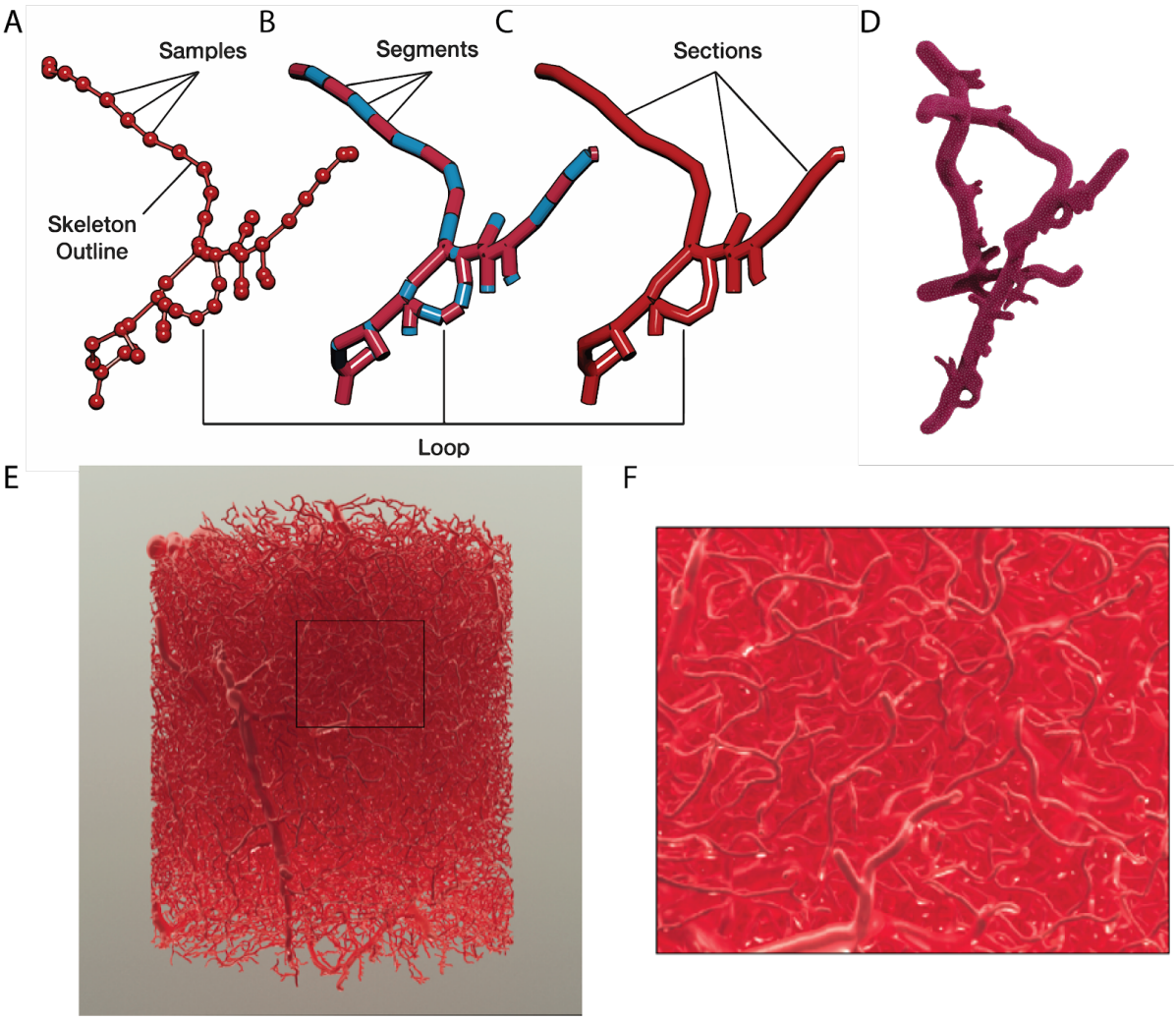

Figure 2.1 Vasculature meshing (A) The vasculature dataset consists of points with a diameter linked by edges. (B) Two consecutive points linked by an edge are defined as a segment. (C) A chain of consecutive points between two forking points is defined as a section. (D) Generated surface mesh with overlaid triangles. (E-F) Original vasculature dataset mesh.

reconstruction process that resulted in small gaps in the skeleton were connected based on the closest distance between components (see supplementary 6.3).

In the NGV framework, I distinguish between two types of datasets: the vasculature skeleton and the surface mesh. Although the majority of the steps in the circuit building pipeline used the skeleton of the cerebral microvasculature, the endfeet surface reconstruction required a more detailed representation of the surface geometry. Thus, starting from the skeletonized dataset we generated a triangular discretization of the surface geometry with variable resolution. The surface mesh is generated based on implicit structures (Fig. 2.1D), known as meta-objects (Oeltze and Preim, 2004), allowing for

the creation of highly-detailed meshes of vasculature datasets (Fig. 2.1E,F) (Abdellah et al., 2020).

2.2 Voxelized virtual brain atlas with 3D density profiles

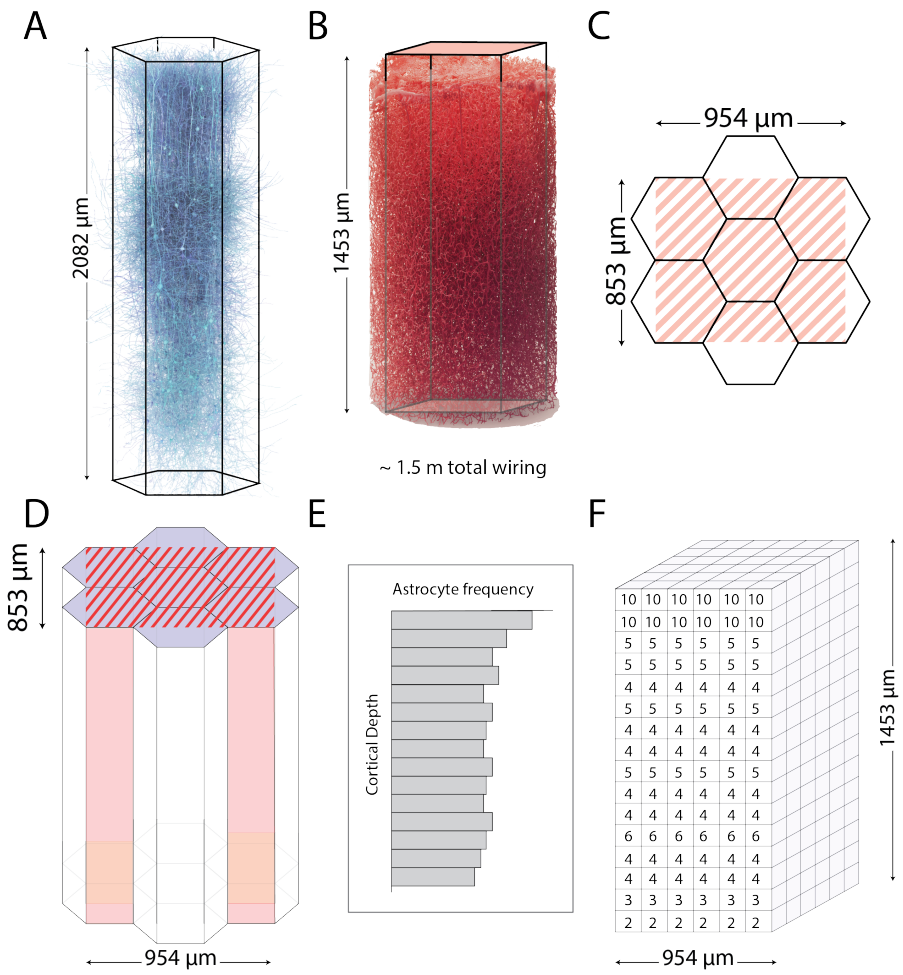

Figure 2.2 The creation of a brain atlas virtual circuit for the NGV requires the co-localization of seven microcircuits (A) and the microvascular dataset (B). The bounding box for the NGV circuit is the co-occupied space for both neuronal and vascular datasets (C,D). (E) 1D astrocyte frequency profile. (F) Rectangular grid with astrocyte counts, interpolated from the frequency profile

To create an NGV circuit, the extend of its spatial embedding, i.e. its bounding region, must be determined. An atlas is a voxelized region equipped with circuit building essential information, such as brain region annotations, densities, cell types etc. (Erö et al., 2018). I manually constructed a virtual 3D atlas for the NGV, due to differing coordinate systems of the vasculature and the neuronal mesocircuit datasets. The microvasculature

dataset was defined in a coordinate system where the z coordinate corresponded to the cortical depth of 1453 µm. The neuronal mesocircuit (Markram et al., 2015), which was comprised of seven microcircuits (Fig. 2.2A) hexagonally tiled, extended down to deep cortical layer 6 at 2082 µm across the y axis. Performing translation and rotation transformations I aligned the vasculature dataset to match the neuronal coordinate system, ensuring overlapping medial axes across y (Fig. 2.2C) and aligned the tops of both datasets at the pia. Due to the difference in height (vascular 1453 µm vs. neuronal 2082 µm), layer 6 was omitted from the NGV circuits, because there was no vasculature wiring covering that region. The spatial intersection of the aligned datasets (Fig. 2.2D) resulted to a bounding region of 954 µm × 853 µm × 1453 µm, which was used throughout the framework.

The voxelized atlas was constructed as a grid spanning the bounding region, in which the voxel y dimension (depth) was chosen to reflect the discretization resolution of the input frequency profile, which was 5 µm. A cell frequency profile is an 1D histogram of the number of astrocytes per mm^3 binned across the cortical depth (Appaix et al., 2012). Not having bin dimensions available for the lateral dimensions, x and z voxel size was arbitrarily selected to be 10 µm. The astrocytic frequencies were mapped to the 3D voxelized grid, by assigning a constant frequency on the xz plane and the profile values to the voxels in the y-direction (Fig. 2.2F).

2.3 Context aware placement of somata

An unordered set of positions (point pattern) $\mathbf{p} = \{p_1, p_2, ..., p_n\}$ can be modelled as a realisation of the Gibbs spatial point process $\mathbf{P}$ with a general probability density function (Dereudre, 2019; Ruelle, 1999):

$$f(\mathbf{p}) = \frac{1}{Z} h(\mathbf{p}) \qquad h(\mathbf{p}) = exp(-U(\mathbf{p})) \tag{2.1}$$

where $h(\mathbf{p})$ is the unnormalized density, U denotes the energy or potential of the point set interactions, and Z is a normalizing constant. Astrocytic somata in the neuropil exhibit a non-uniform laminar organization which can be modeled via a first order intensity $\lambda(p_i)$, which expresses the number of somata per unit of volume. Their contact spacing behavior on the other hand can be modeled as a second order pairwise repulsion interaction $r(\|p_i - p_j\|)$ for every $i \neq j$. Thus,

$$U(\mathbf{p}) = \sum_{i=1}^{n} \left(-\lambda(p_i) + \sum_{j \neq i} r(\|p_i - p_j\|) \right) \tag{2.2}$$

In order to simplify the combinatorial nature of the pairwise interaction we will instead switch to a repulsive influence exclusively from the nearest neighbor. Furthermore, a simple $1/r$ repulsion will be used:

$$\sum_{j \neq i} r\left(\|p_i - p_j\|\right) \sim r\left(\min_{j \neq i} \|p_i - p_j\|\right) \qquad r(d) = \frac{r_0}{d} \tag{2.3}$$

assembling all the above the unnormalized Gibbs density of the spatial point process for astrocytic somata point patterns has the form:

$$h_g(\mathbf{p}) = exp \sum_{i=1}^{n} \left(\lambda(p_i) - \frac{r_0}{\min_{j \neq i} \|p_i - p_j\|} \right) \tag{2.4}$$

We can now add further constraints on the soma generation by creating hybrid unnormalized densities. A constraint can be thought as a conditioning event $\mathcal{A}$ which is expressed by the indicator function $h_i = \mathbf{1}\{\mathbf{p} \in \mathcal{A}\}$. Conditioning events include out of the bounding box restriction and overlapping with other geometrical elements, such as astrocytic or neuronal somata and the vasculature.

The resulting hybrid unnormalized density:

$$h(\mathbf{p}) = h_g(\mathbf{p}) \prod_{i=1}^{k} h_i(\mathbf{p}) \tag{2.5}$$

For the overlap is not sufficient to check if the placement of a new point collides with another geometric entity. An astrocytic soma has volume, thus we can interpret it as a sphere of a certain radius. When a placement trial is taking place, the radius is sampled from a truncated normal biological distribution and then the check for the overlap is performed.

In order to simulate the generation of a point pattern we need to form the Papangelou conditional intensity, which is the ratio of the density function with a new position u and without it:

$$\lambda_p(u, \mathbf{p}) = \frac{f(\mathbf{p} \cup \{u\})}{f(\mathbf{p})} = \frac{h(\mathbf{p} \cup \{u\})}{h(\mathbf{p})} \tag{2.6}$$

It is evident that the normalizing constant is not included in this formulation.

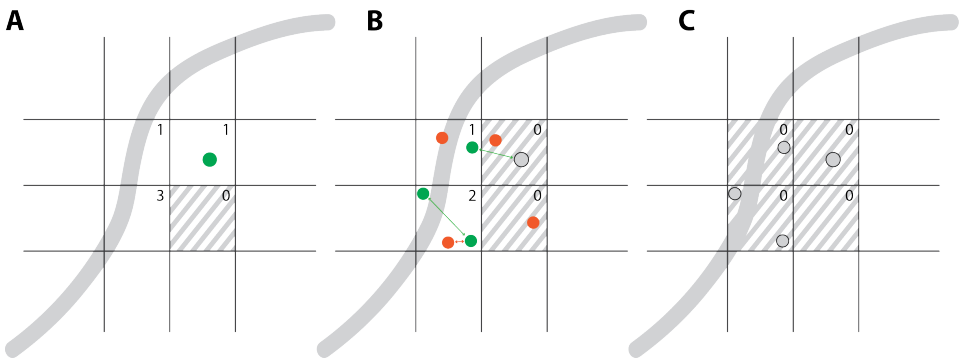

Figure 2.3 Placement steps: Green circles represent valid soma placement trials, red the invalid and gray the accepted ones from the previous step. Similarly, green and red lines represent valid and invalid nearest distance evaluations respectively. The continuous gray line represents the geometry of a vessel, which crosses the grid and influences placement. (A) The astrocytic density is converted into astrocyte counts, which are reduced when a soma is placed into the respective voxel group. (B) A placement trial is rejected if it takes place into a maxed-out voxel, or if it collides with other geometrical entities. (C) Placement finishes when either all the voxels have been filled or there is no available space to put more somata.

The placement algorithm starts by clustering the voxels intro groups G_i of equal intensity d_i and the total count of the cells in each group N_{G_i} is estimated:

$$N_{G_i} = N_{v \in G_i} \times V_{\text{voxel}} \times d_i \tag{2.7}$$

Each time a soma is placed the respective voxel count is reduced by one (Fig. 2.3A-B). For each placement trial, a position is chosen uniformly from the non-occupied voxels and a radius is sampled from a normal distribution with mean $\mu = 5.6$ and standard deviation $\sigma = 0.7$, extracted from literature data. If there is no collision of the trial sphere with the vasculature skeleton, neuronal somata or already placed astrocytic somata, the energy functional is evaluated and the trial is accepted or rejected according to the Metropolis-Hastings algorithm. If not accepted, a new position / radius combination is generated and the procedure repeats until all voxels have reached their total numbers.

The algorithm finishes when all cell counts have been filled or there is no available space left (Fig. 2.3C).

2.4 Generation of microdomain organization

Although astrocytes are a vastly heterogeneous population derived from embryonic(Ge et al., 2012; Magavi et al., 2012) and postnatal progenitors (Gressens et al., 1992; Levison and Goldman, 1993) (Clavreul et al., 2019), their final morphological types mainly depend on the interactions with the surrounding environment and especially with their astrocytic neighbors. They evenly space with each other via a repulsion process known as contact spacing (Distler et al., 1991), and do not seem to macroscopically interact with neuronal structures (Chang Ling and Stone, 1991; Tout et al., 1993). Formation of microdomains leads to a non-uniform nearest neighbor distance distribution (Lanjakornsiripan et al., 2018; López-Hidalgo et al., 2016).

Microdomains were generated as a geometrical abstraction of the available bounding space of an astrocyte. In biology, the domain arises from the extent of the morphology (Bushong et al., 2002; Distler et al., 1991), while in the in-silico model the bounding domain was generated first, and the morphology was afterward grown in its available space.

Given a set of points $\{p_i\}_{i=1}^{k}$ (generators) that belongs to a closed set $\bar{\Omega} \in \mathbb{R}^d$ the Voronoi volume V_i that corresponds to the generator p_i is defined by (Du et al., 1999):

$$V_i = \left\{p \in \Omega : d_i(p, p_i) < d_j(p, p_j),\ \forall\, j \neq i\right\} \tag{2.8}$$

where d_i is a distance metric. In the conventional Voronoi diagram the euclidean distance is used, however variations and generalizations have been made (Dobrin, 2005), therefore it is important that we choose the appropriate model that is required by our problem.

The Voronoi regions $\{V_i\}_{i=1}^{k}$ constitute a tessellation of Ω if $V_i \subset \bar{\Omega}$ for $i = 1, ..., k$, $V_i \cap V_j = \varnothing$ for $i \neq j$, and $\bigcup_{i=1}^{k} \bar{V}_i = \Omega$. A bisector b is defined as the equidistant boundary between two generators p_i and p_j:

$$b(p_i, p_j) = \left\{p : d_i(p, p_i) = d_j(p, p_j),\ \forall j \neq i\right\} \tag{2.9}$$

In order to account for the specific nature of our problem, a way for each generator point to influence its neighborhood is required due to the fact that astrocytic volumes exhibit variability. Thus, instead of point generators we introduce spherical ones $\{s_i\}_{i=1}^{k} = (p_i, r_i)$ where the squared distance from a point p to s_i and the respective Voronoi (Laguerre) area $L(s_i)$ will be:

$$s_i(x) = ||x - p_i||^2 - r_i^2 \qquad L(s_i) = \{x : s_i(x) < s_j(x),\ \forall j \neq i\} \tag{2.10}$$

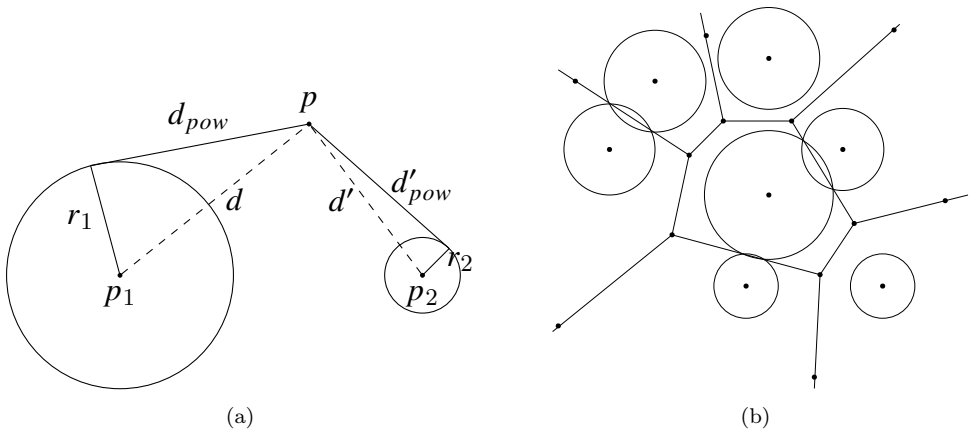

Figure 2.4 (a) Power distances d_{pow} and d'_{pow} for the circles $s_i = (p_i, r_i)$. (b) An example power diagram for seven generator circles

which can be interpreted as the squared length of the tangent on the sphere s_i with radius r_i given through the Pythagorean theorem (Figure 2.4 (a)). By extension it is evident that if the pairwise powers are equated the bisector between two generator spheres s_i and s_j, $b(s_i, s_j)$ is always a hyperplane. An interesting aspect of the power diagram (Aurenhammer, 1987; Tóth, 1977) that was described above, is that two sphere generators that intersect lead to a bisector that goes through their intersecting points (Fig. 2.4 (b)). Astrocytic domains behave in a similar manner by competing for extending their spatial coverage but pushed back by the influence of neighboring astrocytes.

In my framework, the Laguerre tessellation of the microdomains is computed using the Voro++ library (Rycroft, 2009) on the positions and radii of the astrocytic somata, generated during the cell placement step (see section 2.3). The microdomains data structure consists of three datasets: points, triangles and neighbors. Querying the data structure allows for the extraction of the surface mesh of a domain (points, triangles) and its neighbors as calculated from the tessellation algorithm.

To mimic the overlapping nature of the microdomains the polygons of the resulting tessellation were uniformly scaled and the overlap was calculated using Monte Carlo integration. For P14 rats this overlap is approximately 5% of the domain volume (Ogata and Kosaka, 2002). The rest of the sections will refer to the overlapping microdomains, whenever they are mentioned.

2.5 NGV Connectivity

Three types of connectivities are reconstructed via the NGV circuit building pipeline: gliovascular connections (astrocyte-vasculature endfoot), the neuroglial connections (astrocyte-neuron tripartite synapse) and glial connections (astrocyte-astrocyte gap junctions). The generated microdomains were used to specify the accessible space for each astrocyte, allowing queries for the geometrical elements withing their boundaries. To optimize the spatial search queries of the point clouds, R-Tree (Beckmann et al., 1990) spatial data structures were built for the neuronal synapses and the vasculature skeleton.

Gliovascular

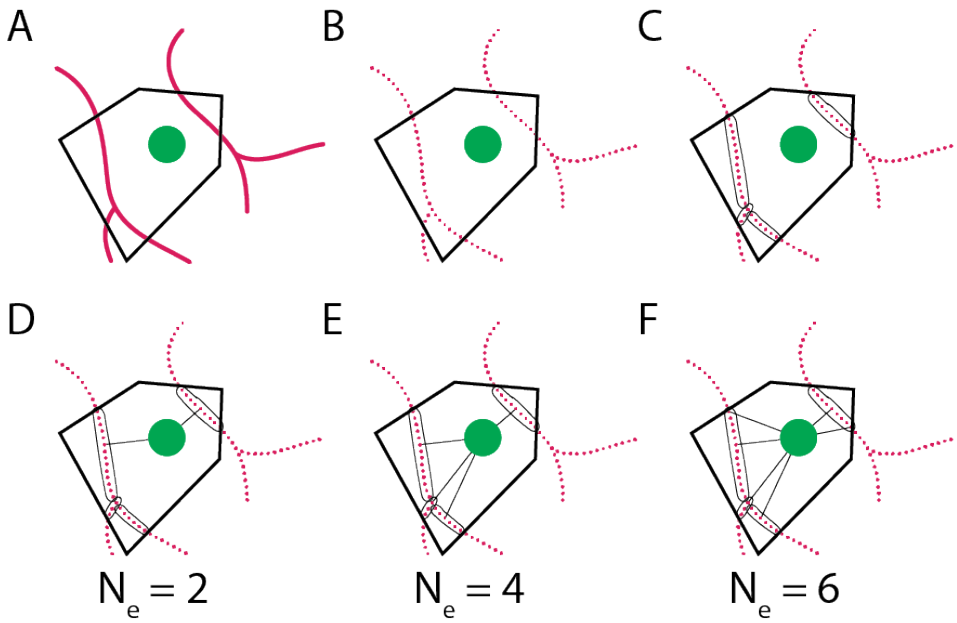

Figure 2.5 Algorithmic overview of gliovascular connectivity. (A-B) Potential targets are distributed on the vascular skeleton. (B-C) The targets included in the astrocyte microdomain are grouped by their section id. (D-E) If the number of endfeet is smaller that the number of components, the closest vertex from the closest components is assigned to them. (F) Otherwise, after assigning the closest vertex from each component, the algorithm iterates over each group finding a vertex that maximizes its distance to the closest selected target.

A set of points $P = \{ p_1, p_2, ..., p_n \}$ was distributed on the skeleton of the vasculature (Fig. 2.5A,B), according to a linear frequency of $0.17\,\mu m^{-1}$ (McCaslin et al., 2011), representing potential endfeet locations. For each astrocyte, a spatial query was performed using the microdomain boundary to find the potential points included in the respective domain. The selection of the actual endfeet targets from the potential point cloud of endfeet locations is realised via the reachout algorithm, which draws a number for the endfeet number $N_e \sim \mathcal{N}(\mu_e, \sigma_e^2)$, where (μ_e, σ_e) are input parameters. The reachout algorithm first generated N_G groups, clustering the points by the vasculature section (for vasculature morphology definitions see section 2.1) they belong to , creating one group per section (Fig. 2.5C). The groups are then sorted by distance of the soma x_s to the closest point in each group. If $N_e \leq N_g$, then the closest point in the closest components are assigned as endfeet targets (Fig. 2.5D). Otherwise, the points are selected one at a time from each group, starting from the closest point of the closest group. When one point has been selected from each group, the algorithm iterates again over the groups selecting the points that maximize the distance to the already selected nearest neighbor (Fig. 2.5E,F). In the end, from the lines that connect the soma to the selected endfeet target locations, the intersection with the surface of the vasculature is calculated, generating the respective endfoot target on the surface of the vasculature.

Based on literature data, each astrocyte was assigned a number of endfeet, ranging from 1 to 5 (Moye et al., 2019). The optimization choices of the reachout algorithm were based on observations on experimental astrocyte reconstructions: endfeet processes minimize their distance to the vascular site (Kacem et al., 1998), maximize the distance to nearby endfeet sites and target different branches (Calì et al., 2019).

Neuroglial

The centroids of the synaptic connections were calculated by averaging the presynaptic and postsynaptic terminal locations for each synapse present in the neuronal circuit (Markram et al., 2015) (Fig. 2.6A). For each astrocyte, a spatial query was performed using the microdomain boundary to find the subset of the synapse centroids included in the respective domain (Fig. 2.6B). From these, a 60% random subset was selected to match the experimental observations (Reichenbach et al., 2010) (Fig. 2.6C). The synapse points were used as attractors for the astrocyte morphogenesis algorithms (see section , Fig. 2.6D).

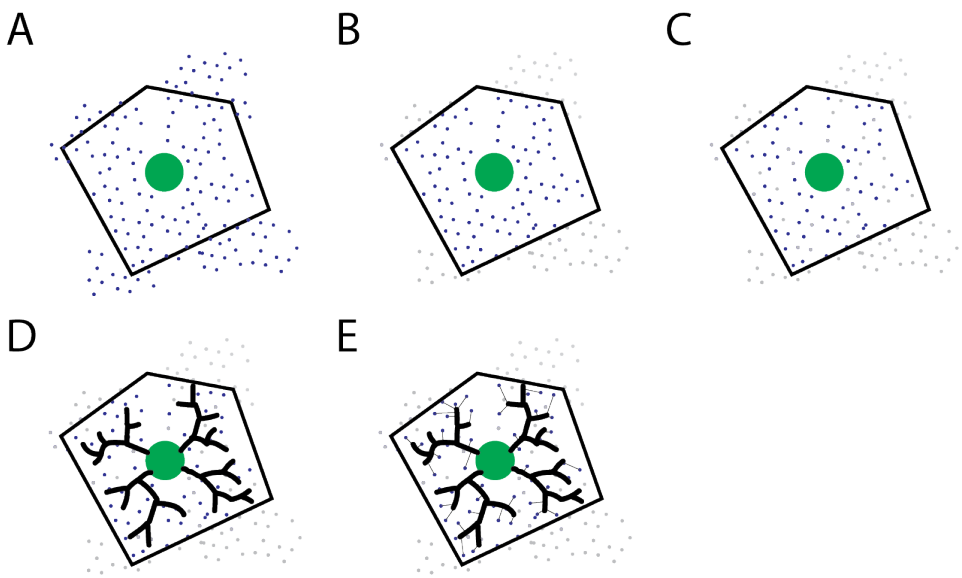

Figure 2.6 Algorithmic overview of the computation of neuroglial connectivity. (A-B) First the synapse centroids included in each astrocytic microdomain are found. (C) A 60% is selected. (D) The morphology grows, using the synapses as attraction points. (E) For each synapse the closest segment is annotated.

Following the generation of the astrocyte morphologies, the neuroglial connectivity is updated by finding for each centroid in the synaptic cloud the closest morphological segment in the morphology (Fig. 2.6E).

Glialglial

The gap junctions between neighboring astrocytes were determined as touches between neighboring colliding morphologies of the grown astrocytes, using the process of touch-detection as presented in Markram et al. (2015)). For this step, the full-grown astrocyte morphology was required.

2.6 Endfeet surface reconstruction

Astrocytes extend processes that abut on the vascular surface, wrapping around it, forming specialized anatomical structures known as endfeet (Kacem et al., 1998; Oberheim et al., 2009). These diffusion-limited compartments (Nuriya and Yasui, 2013) provide a vasculature coverage that ranges from 60-99% depending on the fixation method (Korogod et al., 2015; Mathiisen et al., 2010). Furthermore, in experiments detaching endfeet from the vessel wall using laser ablation, neighboring astrocytic endfeet recovered the available area (Kubotera et al., 2019) without overlapping. Thus, in order to model the astrocytic endfoot geometry based on the sparse studies on their structure, I created an

algorithm that grows in parallel astrocytic endfeet on the vascular surface, growing into their available space without overlapping.

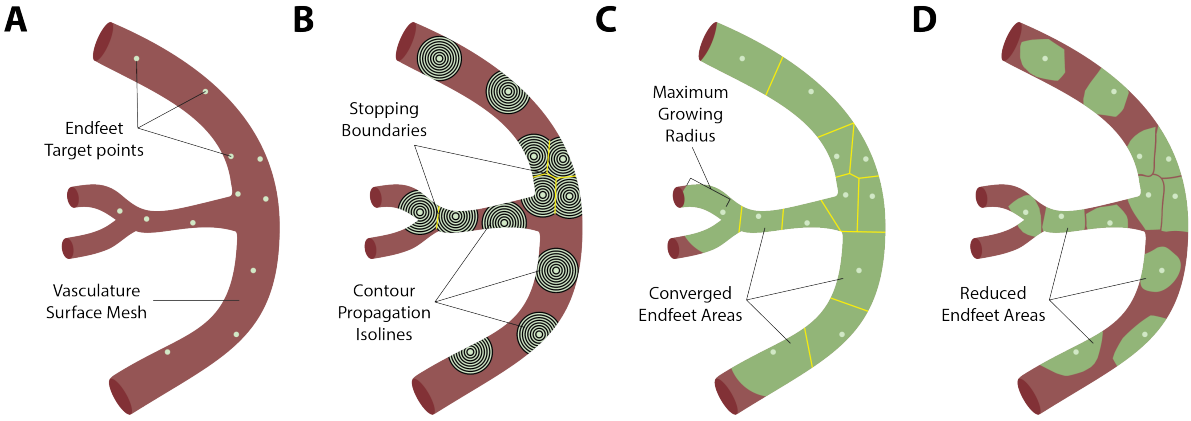

Figure 2.7 Endfeet areas growth algorithm. (A) The endfeet target points on the surface of the vasculature are determined from the gliovascular connectivity. They play the role of the starting seeds for the growing algorithm. (B) Waves propagate isotropically, following the geodesics of the vascular surface, until they either reach an already occupied area or exceed a maximum growing radius (C). (D) The converged areas are then shrank to match the area distribution from the experimental profile.

The surface geometry of the endfeet wrapping around the vasculature was generated from the positions on the surface of the vasculature (endfeet target sites; Fig. 2.7A), which have previously been assigned in the gliovascular connectivity step. From each endfoot target site, the endfeet area is grown isotropically covering the vessel surface (Fig. 2.7B) until it collides with another endfeet area, or until it reaches a maximum radius (Fig. 2.7C). The growth is considered competitive because all the endfeet are growing simultaneously restricting the area they are grown into from neighboring endfeet. After the simulation has converged I pruned the overshoot surfaces (Fig. 2.7D) so that they match the experimental distribution of endfeet areas which is approximately 200 μm^2 (Calì et al., 2019).

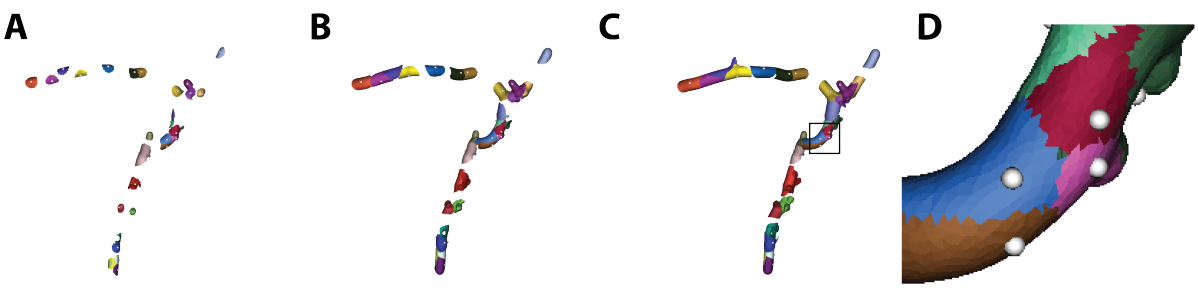

Figure 2.8 Example of endfeet area reconstruction. (A-C) Simulation steps of growing areas and closeup (D) of their convergence.

The growth of an endfoot was modelled as a contour or wave that starts on the endfoot target point and expands following the surface geodesics. More specifically, such a growth "colors" the vertices of the mesh that belong to the endfoot as it grows. The contour evolution was simulated via the solution $t(x)$ to the eikonal equation:

$$
\begin{aligned}
|\nabla_S t(\mathbf{x})| &= \frac{1}{f(\mathbf{x})}, \ \forall \mathbf{x} \in \mathcal{S} \subset \mathbb{R}^3 \\
\phi(x) &= 0, \ \forall \mathbf{x} \in \partial S
\end{aligned} \tag{2.11}
$$

which is first-order partial differential equation, where S is the vasculature surface, a 2D smooth and closed manifold in $\mathbb{R}^3$, ∇_S is the gradient in the tangent plane to the manifold, $t(x)$ is the distance or travel time from the source and $f(\mathbf{x})$ is the speed of travel. Thus, $t(x)$ provides the time that an interface (contour) will need to reach $\mathbf{x}$ from the initial location ∂S. We are particularly interested in the simplified form where $f(\mathbf{x}) = 1$ and equation 2.11 is converted to the signed distance function from the boundary ∂S.

In our use case, in which we want to model the growth of an endfoot on the vasculature manifold, the boundary ∂S corresponds to the endfoot target $\mathbf{x}_e$. Thus, the eikonal equation gives the travel times from the endfoot target to any point on S along the geodesics of its surface. Generalizing this to multiple endfeet targets, would require to calculate the travel times from each surface point to each endfoot target.

To approximate the solution of 2.11 on triangulation S_T of the surface S, which is comprised of nodes x_i, I implemented the fast marching method for triangulated surfaces (Fu et al., 2011). Each node is assigned a value T_i that corresponds to its travel time, which are initially set to $+\inf$ except for the endfoot's one which is 0. Using the one-ring neighbors for each node, the approximated solution of the travel T_i at node x_i is calculated from as the minimum of shortest path distances calculated from all the triangles in then neighborhood.For a triangle (v_1, v_2, v_3), if v_1 and v_2 are upwind of v_3, there is a characteristic line of the gradient $\nabla_S t(\mathbf{x})$ that passes from v_3 and crosses the base of the triangle $\vec{e}_{1,2} = v_2 - v_1$ at x_λ. Thus, the travel time at T_3 is given by:

$$
\begin{aligned}
T_3 &= T_\lambda + T_{\lambda,3} \\
T_3 &= T_1 + \lambda\,(T_2 - T_1) + \|\vec{e}_{1,3} - \lambda \vec{e}_{1,2}\|
\end{aligned} \tag{2.12}
$$

which is derived from the fact that the approximation is linear, thus $T_\lambda = T_1 + \lambda T_{1,2}$ and $T_{\lambda,3} = f\|\vec{e}_{\lambda,3}\| = \|\vec{e}_{\lambda,3}\|$, because we have set the speed function to 1. To represent the gradient characteristic, λ should minimize T_3 and must be in the range $[0, 1]$. See supplementary section 6.2 for the derivation of the solution.

In order to introduce the notion of multiple endfeet growing in parallel, each node x_i on S_T was assigned an endfoot group G_i. Thus, upon initialization all endfoot nodes are assigned $T_i = 0$ and $G_i = i$, where $i = (0, 1, 2, ..., N_{endfeet})$. A priority queue was implemented that allowed to update first the nodes with the smallest travel time at each iteration, simulating the propagation of wavefronts. As nodes were updated with the shortest travel time to the nearest endfoot nodes, the group label of that endfoot was assigned to them and if the node had already a group assigned, the update stopped. This allowed the propagation of the "endfoot waves" on S_T competitively as they were allows to propagate to nodes that were not already captured from a neighbor. The algorithm finished when there were no more vertices in the priority queue to update.

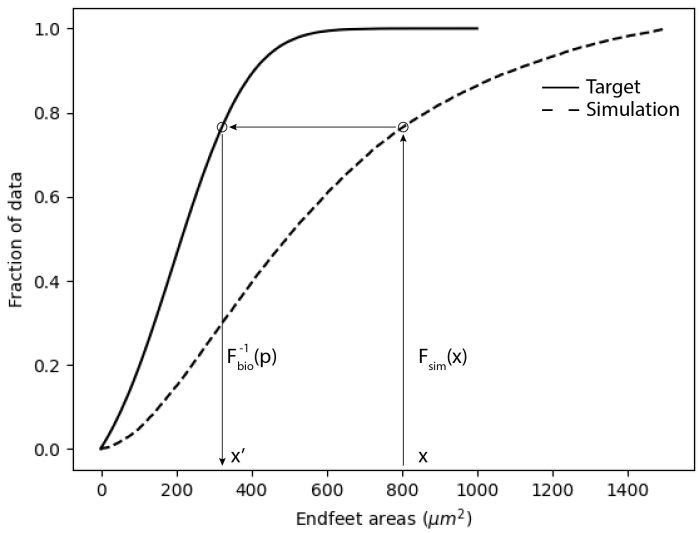

Figure 2.9 Diagram of the are transformation from the simulation area distribution to the target one extracted from the literature via the inverse CDF transform.

The endfeet meshes were reconstructed from the nodes in each group G_i. Due to the fact that the areas of the endfeet covered almost entirely the vasculature surface, a pruning procedure was introduced in order to match a target area distribution, extracted from the literature. Thus, given a target cumulative distribution F_{bio} and the empirical distribution from the simulation $\hat{F}_{sim}$, overshoot endfeet areas A_i were transformed into the respective target ones A'_i via the cumulative inverse transform:

$$A_i' = F_{bio}^{-1}\left(\hat{F}_{sim}(A_i)\right) \tag{2.13}$$

To match the new pruned areas, the geometry of the endfoot meshes was pruned using the travel times that were calculated in the previous step. For each triangle in the endfoot mesh the average travel time was calculated from its vertices and the triangles with the highest travel times were removed one by one until the target area was reached. In other words, the meshes shrunk, starting from the periphery until the target area was approximately reached.

2.7 Programming environment and framework

The NGV circuit building framework was written in Python3 following a component-based design. A component is defined as a standalone processing step with strictly-defined inputs and outputs. The execution of a component may depend on the output files of more than one other component. This relationship between components results in an acyclic graph of dependencies (DAG), which is managed by the Snakemake workflow engine (Köster and Rahmann, 2012). There are a total of thirteen processing steps as shown in Figure 7, and three main data categories in the framework: external inputs, cell-related data, connectivity-related data. External inputs are separated into input datasets and configuration parameters. Input datasets, such as the region of interest, astrocytic densities, the vasculature, etc., represent all the data that is used by the NGV framework. Configuration parameters include algorithm constants and NGV profile density distributions, which configures how the framework consumes the external datasets and how the algorithms are set. Different species, ages, and pathologies each have distinct profiles that need to be parameterized first in order to generate a representative NGV circuit. NGV cells and connectivities are stored in the SONATA network specification (Dai et al., 2020), as nodes and edges in HDF5 binary files. Blue Brain's libSONATA library provides support for the reading and writing of HDF5 node and edge datasets.

Each network entity collection, such as neurons and glia, is stored as a node population. Each cell in the node population is identified by an identifier (index). Node populations include attributes related to their spatial embedding (soma position, soma radius, orientation, layer, etc.), their morpho-electrical characteristics (morphological type, electrical type, etc.), and other information which emerges from the circuit building, such as the morphology filepath. Astrocytes, which are stored as glia with an ASTROCYTE morphological type, map to an additional dataset: the microdomains.

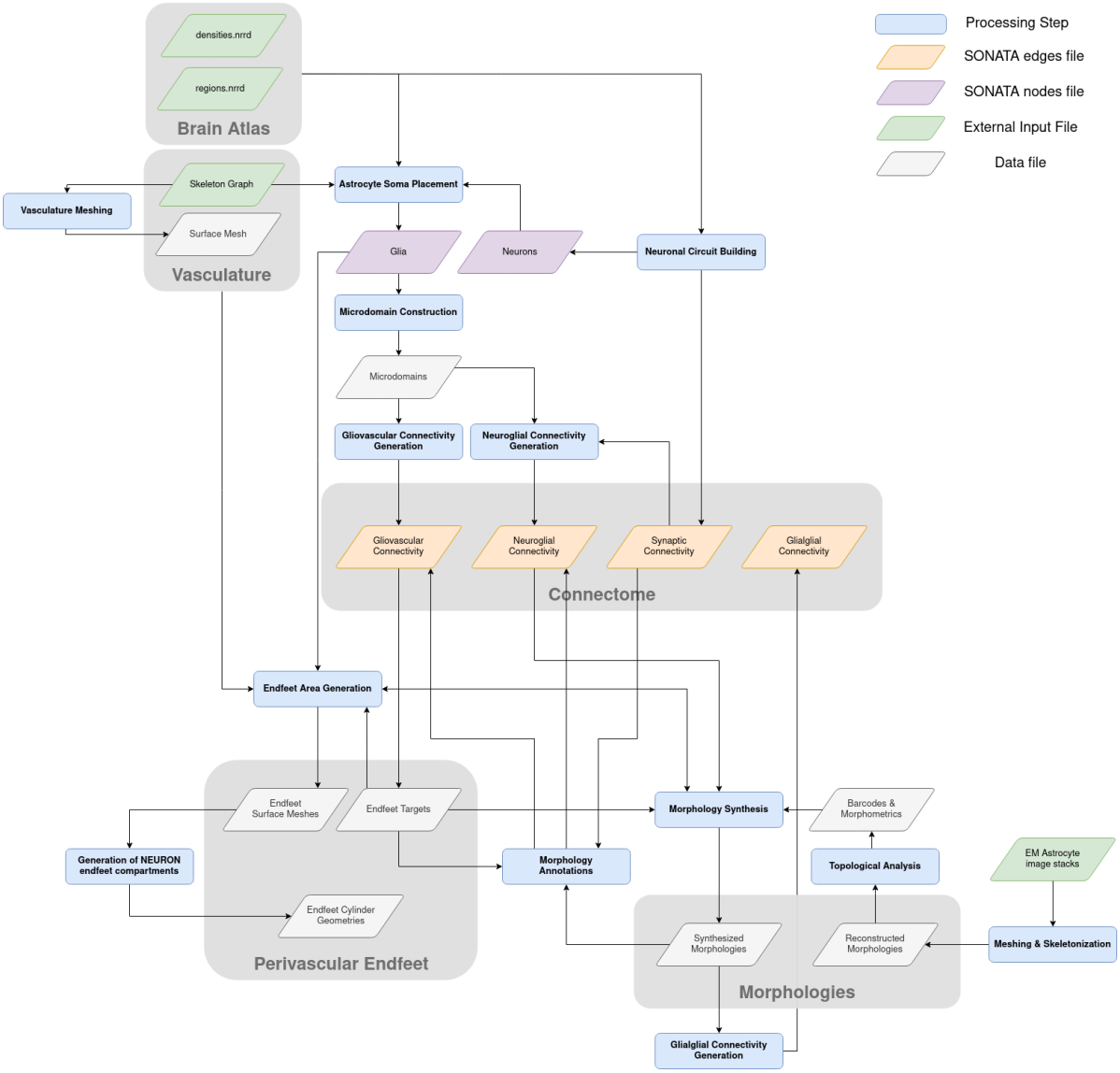

Figure 2.10 The main input datasets to the ngv frameworks are the brain atlas intensity and region of interest, the vasculature skeleton and surface mesh, the neuronal population from the neuronal circuit building pipeline and the astrocyte reconstructions required for synthesis. Each step also requires parameters for its algorithms that comprise the parameter profile. The data outputs from the framework are split into 3 categories: node populations and their properties (e.g. microdomains for astrocytes), edge populations or connectivities and their properties (e.g. endfeet areas for gliovascular connectivity) and synthesized morphologies.

Connectivity between two node populations is registered as an edge population. The NGV architecture is established by four edge populations: synaptic, neuroglial, gliovascular, and glial-glial. Synaptic connectivity was produced during the neuronal circuit building pipeline and is an input for the NGV building along with the neuronal node population. Neuroglial, gliovascular and glial-glial connectivities represent the connections between

neurons and astrocytes, astrocytes and the vasculature and astrocytes and their neighbors respectively. The gliovascular edge population also stores an endfoot identifier, which provides access to the endfeetome data structure containing the mesh of the endfeet that have been grown on the surface of the vasculature.

2.8 Results

2.8.1 NGV circuit

Input data	Type	Values	Units	Range	References
General					
Vasculature	morphology file	–	–	–	Reichold et al. (2009)
Neuronal circuit	circuit	–	–	–	Markram et al. (2015)
Cell Placement					
Astrocyte density profile	binned histogram	from file	astrocytes/mm^3	–	Appaix et al. (2012)
Soma radius distribution	normal	$\mu = 5.6$ $\sigma = 0.7$	µm	$0.1 < x < 20$	Bushong et al. (2004) Bagheri et al. (2013) Puschmann et al. (2014) Lee et al. (2016) Bindocci et al. (2017) Calì et al. (2019)dat
Nearest neighbor distance	number	30	µm	–	Appaix et al. (2012) López-Hidalgo et al. (2016)
Microdomains					
Overlap	Number	5	%	–	Bushong et al. (2002, 2004) Ogata and Kosaka (2002) Wilhelmsson et al. (2006)
Connectivities					
Linear density	number	0.17	µm^{-1}	–	McCaslin et al. (2011)
Number of endfeet	normal	$\mu = 2$ $\sigma = 1$	–	$1 < x < 5$	Calì et al. (2019) Moye et al. (2019)
Synapses subset fraction	number	60	%	–	Witcher et al. (2007) Ventura and Harris (1999)
Endfeet surface reconstruction					
Target area distribution	normal	$\mu = 192$ $\sigma = 160$	µm^2	$0 < x < 1000$	Calì et al. (2019) Wang et al. (2020)
Thickness distribution	normal	$\mu = 0.97$ $\sigma = 0.1$	µm	$0.01 < x < 2.0$	Calì et al. (2019)
Morphology Synthesis					
Reconstructed morphologies	morphology file	–	–	–	Calì et al. (2019)
Perisynaptic targeting	number	0.01	–	–	–
Perivascular targeting	number	0.07	–	–	–
Perisynaptic randomness	number	0.3	–	–	–
Perivascular randomness	number	0.25	–	–	–
Segment length	normal	$\mu = 0.1$ $\sigma = 0.001$	–	–	–
Endfoot attraction	function	–	–	$0 < x < 1$	see supplementary 6.1
Kill distance factor	number	15.0	–	–	–
Influence distance factor	number	30.0	–	–	

Table 2.1 NGV model parameters and input data.

The bounding region extended to 954 µm × 1453 µm × 853 µm, which corresponded to a total volume of approximately 1.18 mm^3. The NGV circuit consisted of a total of 14648 astrocytes and 88541 neurons, which formed 9.2 million neuroglial, 30172 gliovascular and 3.5 million glialglial connections. The vasculature had a total length of 1.37 m, total surface area of 23.82 mm^2 and a total volume of 0.04 mm^3, occupying approximately 3.5% of the bounding regions volume. A summary of the model parameters can be found in table 2.1.

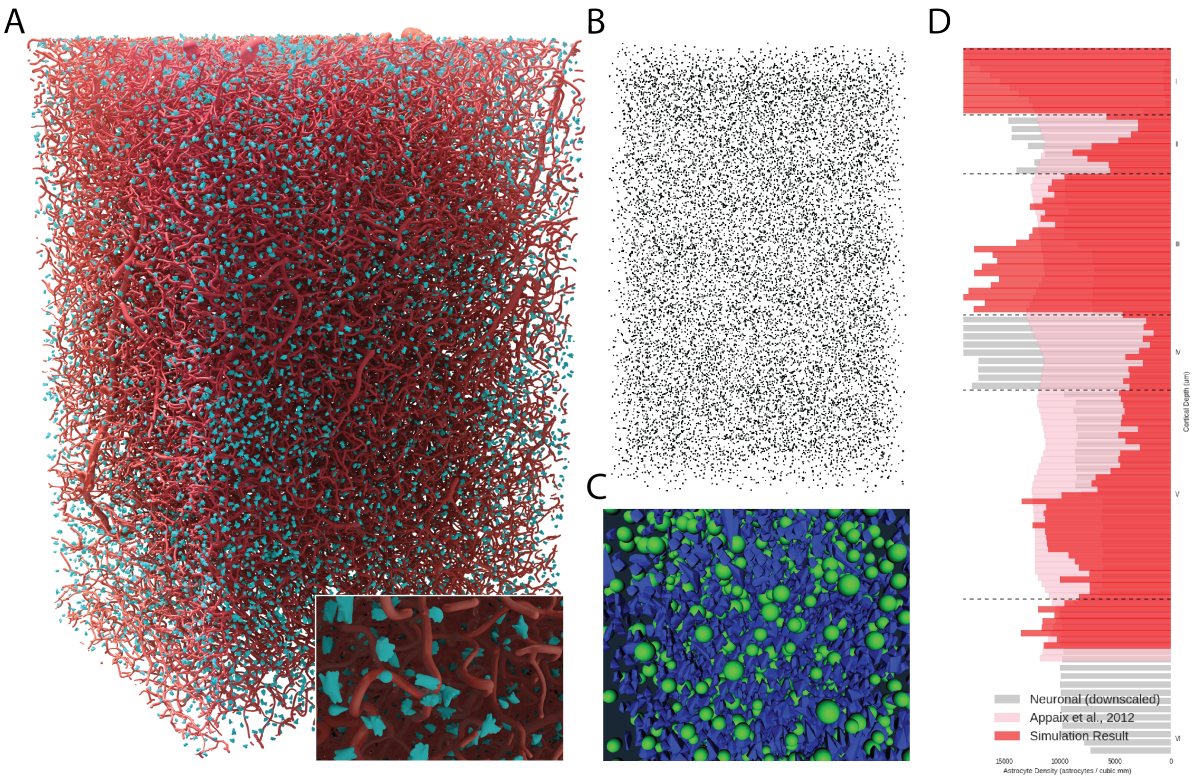

Figure 2.11 Illustrations of the somata distribution in the NGV circuit. (A) Illustration of vasculature mesh (red) and astrocytic somata (turquoise). (B) Evenly distributed astrocytic somata, unaffected by vasculature geometry. (C) Neuronal somata convex hulls (blue) restrict astrocytes (green) from being placed according to their densities and distancing. (D) Cortical depth histograms of neurons (black), expected (pale red) and resulting astrocyte numbers (red).

The astrocytic somata were distributed avoiding collisions with the geometry of the vasculature (Fig. 2.11A), delimited by the bounding box. Due to the low volume occupancy of the microvascular network, the placement of the somata was unobstructed. In addition, the differing diameters of pial and penetrating arteries and veins didn't affect the even distribution of the somata and no prominent clustering was observed (Fig. 2.11B). However, the consideration of neuronal somata introduced areas where it was impossible to place astrocytic somata (Fig. 2.11D), introducing spatial biases in the

distribution of the astrocytes (Fig. 2.11D). Therefore, instead of placing the astrocytes before the neurons, the astrocytes were placed first and neurons second. The rationale behind this choice is twofold: the high neuron to astrocyte ratios (Herculano-Houzel, 2014) and the strict tiling organization of astrocytes (Bushong et al., 2002).

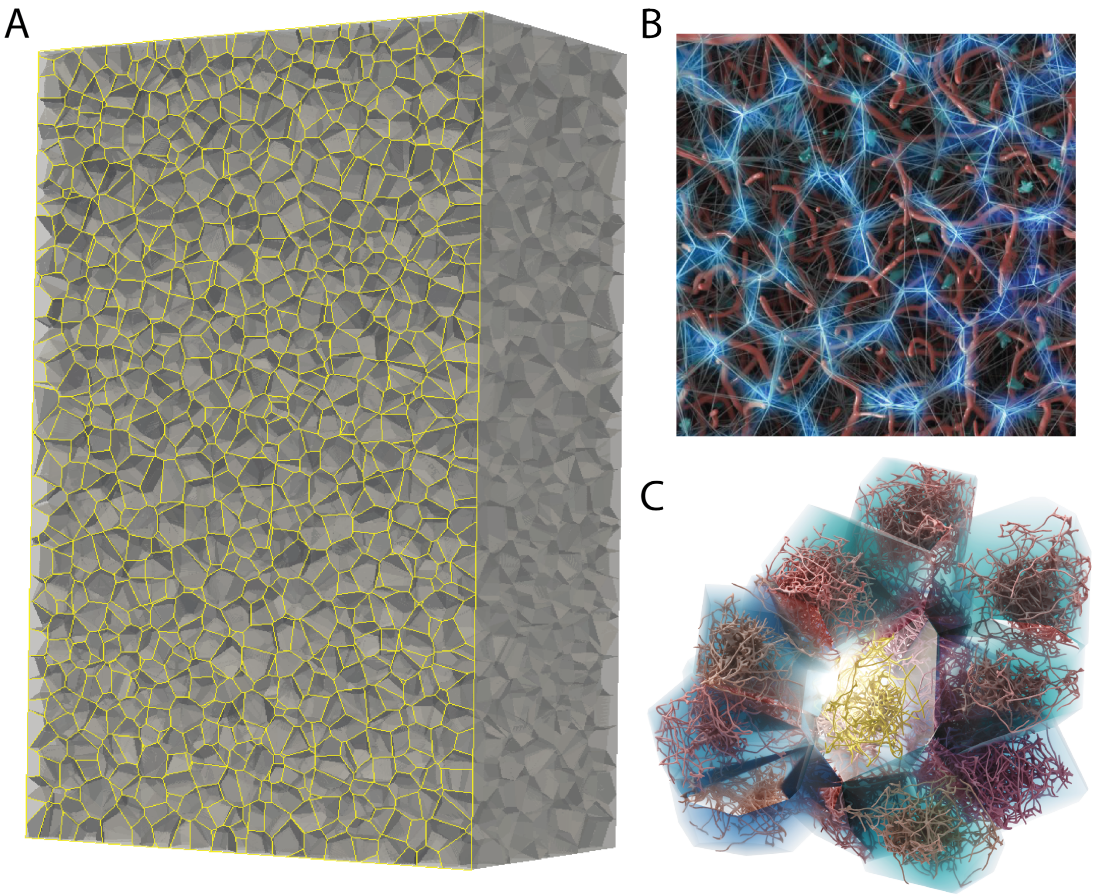

Figure 2.12 Illustrations of the microdomains in the NGV circuit. (A) Cross section of the microdomain tessellation geometry without other entities. (B) Overlay of microdomain edges with astrocytic somata (turquoise) and vasculature (red). (C) Example of microdomain neighborhood, populated with random trees

The generation of the microdomains tiles the entire bounding region (Fig. 2.12A), creating the polygonal boundaries for each astrocyte. Due to the existence of the boundary, an outer layer of boundary microdomains was created, intersecting with the walls. Given that these microdomains were not reflecting biological structures, they were omitted from the analyses. The rest intersected with the vascular wiring (Fig. 2.12B) and neuronal synapses, compartmentalizing them. Each microdomain was surrounded by a neighborhood of domains (Fig. 2.12B), which shared polygonal faces (tessellation bisectors). A limitation of such a modelling approach is that the average size of the

domains is inversely proportional to the average density of astrocytes. While this works well within the biological ranges of astrocytic densities, more complex use cases involving empty regions of cells, would require the creation of "ghost" somata so that the correct size domains are generated. Otherwise, the domains would extend until a neighbor is found on the other side of the empty region.

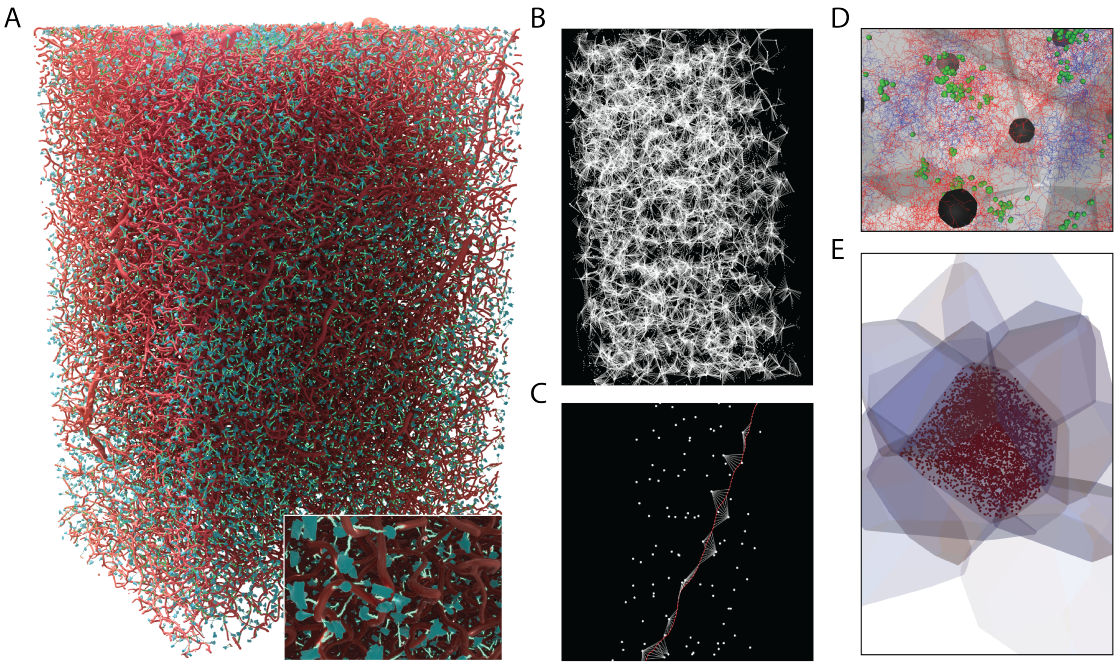

Figure 2.13 Illustrations of the connectivity in the NGV circuit. (A) Astrocytic somata (turquoise), vasculature (red) and biased random walks (green) connecting the somata to the surface targets on the vasculature. (B) Connectivity to potential targets distributed on the vasculature and on a single artery (C). (D) Glial-glial connections (green) between an astrocyte and all its neighbors. (E) Synapses (red) that are contained into a single microdomain, surrounded by its neighbors.

In order to demonstrate the gliovascular connections, biased random walks grew from the soma towards the targets, which can be seen in figure 2.13A. Connections to potential targets within their domains was illustrated in figure 2.13B for the whole circuit and for a single artery (Fig. 2.13C). Glial-glial connectivity required the full morphologies to establish the touch space between the processes of neighboring astrocytes (Fig. 2.13D). Synapse-astrocytes connections on the other hand were calculated from the microdomain extents (Fig. 2.13E), and after the full morphologies were grown, the specific segment annotation to the closest synapse was made.

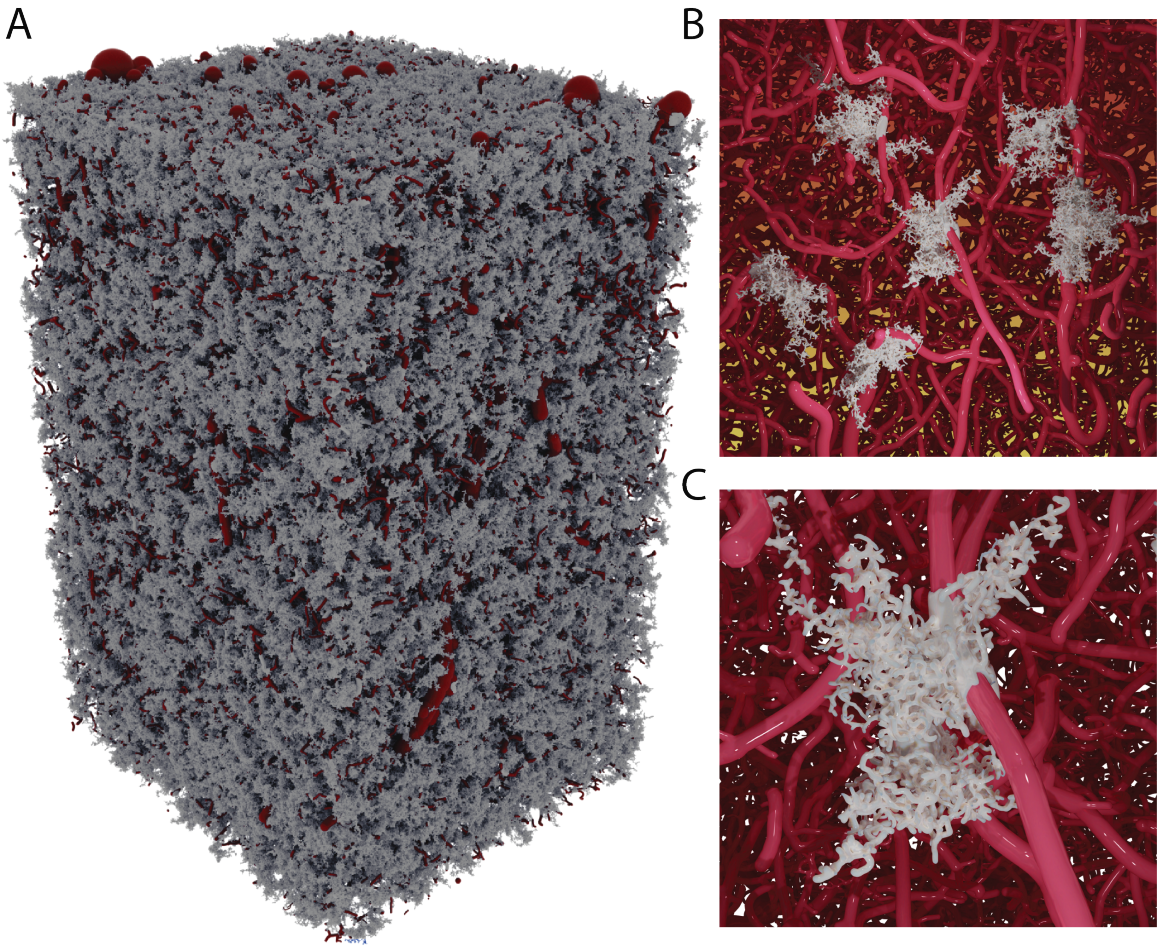

Figure 2.14 Illustrations of the circuit with the grown morphologies. (A) Overview of the astrocytic circuit. (B) A group of five astrocytes with their endfeet. (C) Closeup of a single astrocytic morphology and its endfoot on the surface of the vasculature.

The 14648 astrocytic morphologies were grown independently of each other and in parallel, distributed into 36 cores (Fig. 2.14A). Due to the microdomain boundaries partitioning the space, each astrocyte had a spatial boundary to grow into without requiring real-time feedback concerning the growing of its neighbors. In this model the growing processes did not avoid geometrical elements in space, because of the costly spatial intersection queries which skyrocketed the computation time of synthesis. New, more optimized approaches are required to introduce collision detection while growing trees. Therefore, astrocytic processes were intersecting with the vasculature morphology in my model (Fig. 2.14C).

The NGV circuit build produced approximately 860GB of data, of which 25GB corresponded to the astrocyte related datasets and the rest to the neuronal ones (Markram

et al., 2015). The framework required approximately 18 hours to complete on 36 cpu cores. Taking into account that morphology synthesis was the slowest step in the framework, using more cores would significantly reduce the running time.

2.8.2 Network validation

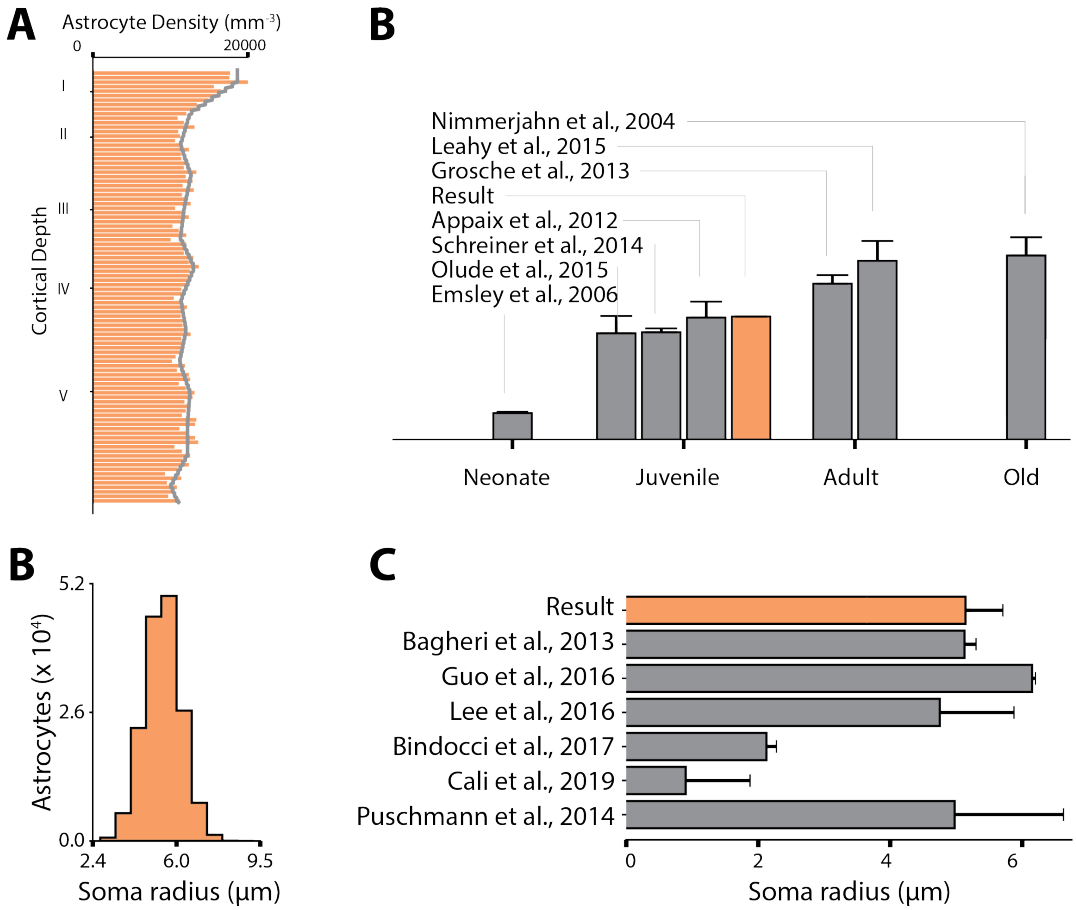

Figure 2.15 (A) Astrocyte density histogram (orange) compared to the input density profile (gray). (B) Average circuit density (orange) compared to reported values (gray) for different animal ages. (C) NGV circuit somata radii histogram. (D) Comparison of average soma radius with reported values (gray)

To ensure biological fidelity, I validated that input constraints could be reproduced for each step in the circuit building process, and compared structural measurements with respective ones extracted from the literature and experimental data. Astrocytes were placed according to the densities reported in (Appaix et al. (2012); Fig. 2.15A), measuring an average density of 12 241 mm^{-3} ranging from 9367 mm^{-3} to 21 479 mm^{-3}, which in a total number of 14648 astrocytes. The y-coordinates of the generated somata positions were binned and the density histogram was calculated as the number of cells in each bin divided by the respective bin volume. The model accurately reproduced

the density distribution of the input profile (Fig. 2.15A), corresponding to juvenile rat brain slices. Other studies presented similar numbers: $(10\,700 \pm 1750)\,\mathrm{mm}^{-3}$ in Olude et al. (2015) in african giant rats and $(10\,800 \pm 400)\,\mathrm{mm}^{-3}$ (Schreiner et al., 2014) in mice. Astrocytic density increases from $(2666 \pm 133)\,\mathrm{mm}^{-3}$ in neonates (Emsley and Macklis, 2006), to $(15\,696 \pm 860)\,\mathrm{mm}^{-3}$ (Grosche et al., 2013) and $(18\,000 \pm 2000)\,\mathrm{mm}^{-3}$ (Leahy et al., 2013) in adults. Densities in old rodents have been found to slightly increase $(18\,350 \pm 1141)\,\mathrm{mm}^{-3}$ (Nimmerjahn et al., 2004) compared to adult animals. Therefore, our model produced astrocyte numbers within the range encountered in literature (Fig. 2.15B), reflecting experimental numbers found in juvenile rodents. In addition, switching the density profile it is possible to reproduce different density profiles, or scale the existing ones (see section 4.2). The soma dimensions were sampled from the normal distribution which was created from averaging radii collected from various literature sources (Bagheri et al., 2013; Bindocci et al., 2017; Lee et al., 2016; Puschmann et al., 2014). The resulting distribution of the astrocytic somata had a mean $\mu_r = 5.5$ and a standard deviation $\sigma_r = 0.7$ (Fig. 2.15B). An improved quantification of the astrocytic radii is required for juvenile rats, because of the largely different values that are encountered in the literature that do not seem to agree with each other.

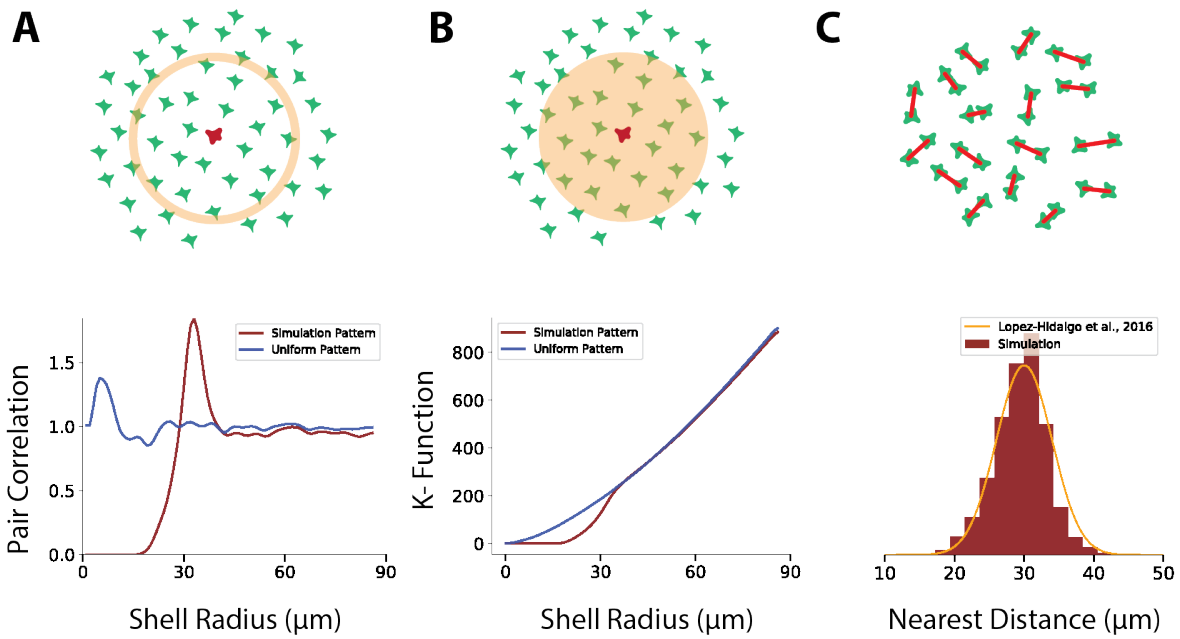

Figure 2.16 Spatial analysis of the point patterns corresponding to astrocytic somata. (A) Pair correlation function. (B) Ripley's K-function. (C) Distance distribution from each astrocytic soma to its closest neighbor, compared to the input profile (orange) from Lopez-Hidalgo et al. 2016.

Next, I validated the spatial association of the somata to verify whether they were evenly distributed. The simulation of contact spacing is essential for the formation of

microdomains (Tout et al., 1993). I validated the repulsion model using three measures: pair correlation function (PCF), Ripley's K-function (Dixon, 2014) and nearest neighbor distribution. The PCF expresses the probability of finding one point a given distance from another point. Using the repulsive model, I found that the highest probability to find a soma at a distance around another soma was at 30 µm (Fig. 2.16A). In contrast, when the placement was ran without repulsion the respective PCF exhibited a small peak around 5 µm, the average radius of the astrocytic somata, rising from the algorithm's restriction for somata overlapping. Ripley's K-function is a similar spatial analysis method that uses a cumulative cover to describe the clustering or dispersion of a spatial point pattern. A random point sample is represented as a diagonal line, whereas clustered patterns move the line above the diagonal and disperse patterns move it below. Therefore, it was verified that astrocyte somata exhibit a disperse organization, while the non-repulsive placement demonstrated and almost diagonal trend, except from a small disperse deviation at very small distances because of the soma sizes. Finally, the nearest neighbor distribution explicitly quantified the distance of each soma to its closest neighbor, matching the input distribution at 30 µm. Thus, all three measures verified that astrocytes were accurately spaced with respect to the target nearest neighbor distribution. Due to the fact that the repulsion functional can take any form, repulsive behavior is not the only possibility with this placement model. For example the spring and Lenard-Jones potentials have been successfully tested as well. In addition, more complex potentials that allow for repulsion and/or attraction to more than one types of elements (e.g. astrocytes and vasculature) can naturally extend the current model.

The average microdomain volume was 81 725 µm^3, ranging from 11 697 µm^3 to 266 599 µm^3, whereas the overlapping microdomains were measured at an average of 86 106 µm^3, ranging from 12 324 µm^3 to 280 890 µm^3. The overlapping distribution exhibited a small shift to the right, because of the higher domain volumes 2.17A., for juvenile animals the volume distribution of the domains compared to a tight tessellation was negligibly different. In literature studies, ages seem to be a determining factor in the size of the microdomains. Studies using adult animals report volumes from 16 400 µm^3 to 31 000 µm^3 (Bagheri et al., 2013; Grosche et al., 2013; Mishima and Hirase, 2010; Scofield et al., 2016; Wilhelmsson et al., 2006). On the other hand, juvenile rodents microdomain volumes have been observed to range between 65 900 µm^3 and 86 700 µm^3 (Bushong et al., 2002; Ogata and Kosaka, 2002). The NGV model produced domain volumes that corresponded to juvenile astrocytic densities, capturing the magnitude of the respective studies. In the work of Lanjakornsiripan et al. (2018) specialized techniques were used to explore the astrocytic morphology, identifying a volume distribution ranging from 40 000 µm^3 to 180 000 µm^3.

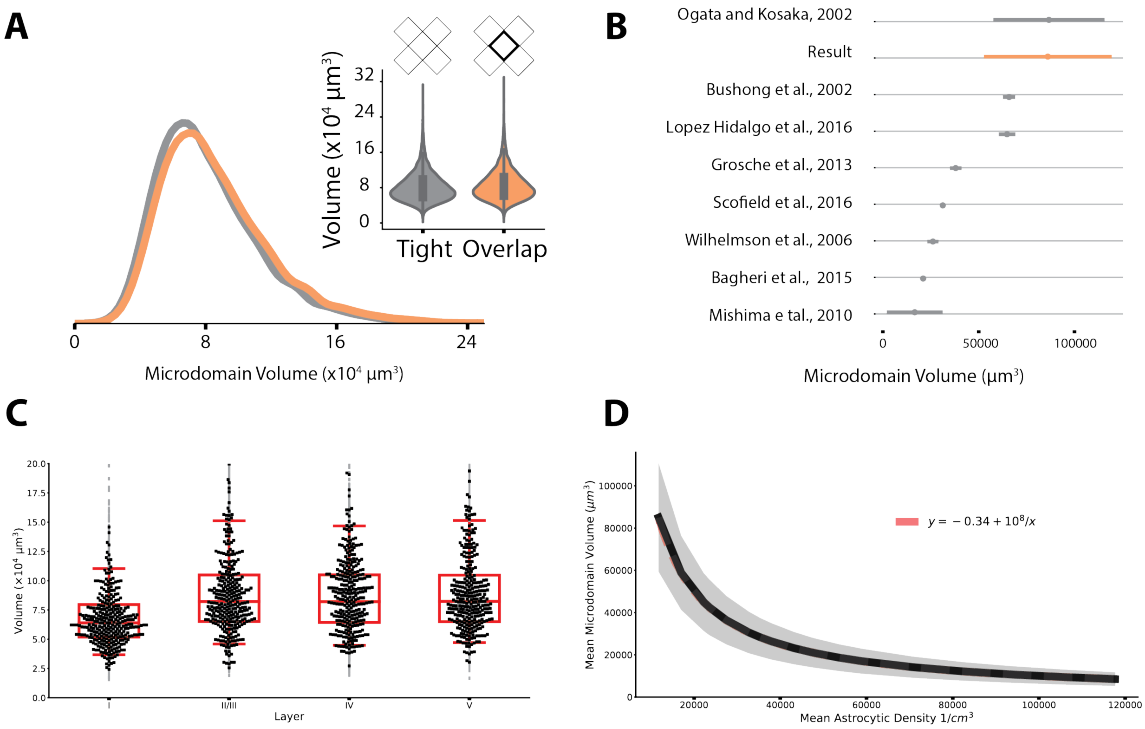

Figure 2.17 NGV microdomains analysis and validation. (A) Volume distribution of the regular (gray) and overlapping (orange) tessellations. (B) Comparison of NGV microdomain volumes (orange) with literature sources. (C) Per layer microdomain volume distributions and their repsective box plots (red). (D) Scaling relationship between average microdomain volume and average astrocyte density.

The most notable result of their quantification was that layer I astrocytes exhibited significantly lower volume than the rest of the layers. The NGV circuit reproduced this observation, which resulted from the significantly higher densities in layer I (Fig. 2.17C). As a matter of fact the average size of the domains decreases as the average astrocyte density increases (Fig. 2.17D; see also section 4.2 for the effect of the density change to structural architecture). In my model the average microdomain volume $\bar{V}$ scaled down with average density $\bar{d}$ as follows: $\bar{V} = -0.34 + \frac{10^8}{\bar{d}}$. This result provides an invaluable insight: the contact-spacing organization of astrocytes in biology induces constraints of purely geometric nature. This allows for the abstraction of astrocytes into mathematical entities, i.e. tessellation regions, verifying my initial assumption that astrocytic domains can be modelled as such.

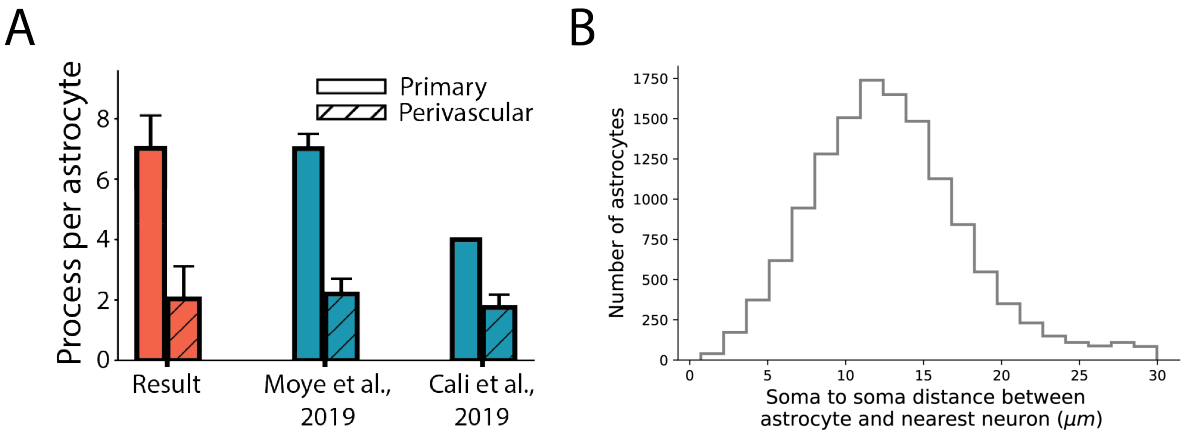

Figure 2.18 Validation of astrocytic processes and association with neurons. (A) Average number of processes (primary and perisynaptic) per astrocyte for the NGV circuit (salmon) and literature sources (turquoise). (B) Histogram of the distances for each astrocytic soma to the closest neuronal soma.

In the NGV circuit the number of perivascular processes was constrained for juvenile rodents at 2 ± 1 processes. These numbers are in accordance with literature measurements (Calì et al., 2019; Moye et al., 2019). Furthermore, the number of primary processes in the NGV was measured to as 6.5 ± 1 processes (Fig. 2.18A). To validate the spatial relationship between neurons and astrocytes, for each astrocyte the distance to the closest neuronal soma was calculated (13 ± 5) µm, ranging from 0.7 µm to 30 µm (Fig. 2.18B). The distribution falls within the range of literature observations, that is from 5 µm to 30 µm for three types of inhibitory neurons (Refaeli et al., 2020).

The endfeet surface meshes, initially covered 91.1% of the vasculature surface. Studies using chemical fixation for their tissues reported a 70% – 100% coverage (Kacem et al., 1998; Korogod et al., 2015; Mathiisen et al., 2010; Simard et al., 2003) of the vasculature by perivascular endfeet. However, Korogod et al. (2015) showed that chemical fixation induces swelling of the astrocytic compartment, leading to increased coverage. They reported that coverage of the vasculature by astrocytic endfeet was (62.9 ± 1.5) % using cryo-fixation, which is more likely to preserve the anatomical structures of the neocortex. An unconstrained simulation of growing the NGV endfeet surfaces produced a full coverage of the vasculature, however in order to generate a biologically plausible distribution the areas were pruned according to the reported endfeet area distribution in Calì et al. (2019). After the pruning, the resulted endfeet mesh area distribution was (225 ± 132) µm^2 in the range $[0, 1000]$ µm^2 (Fig. 2.19), matching the respective biological values (Calì et al. (2019); Fig. 2.19B). The total area of the pruned meshes covered a 30% of the total vasculature (Fig. 2.19C), less than half than the coverage reported by Korogod

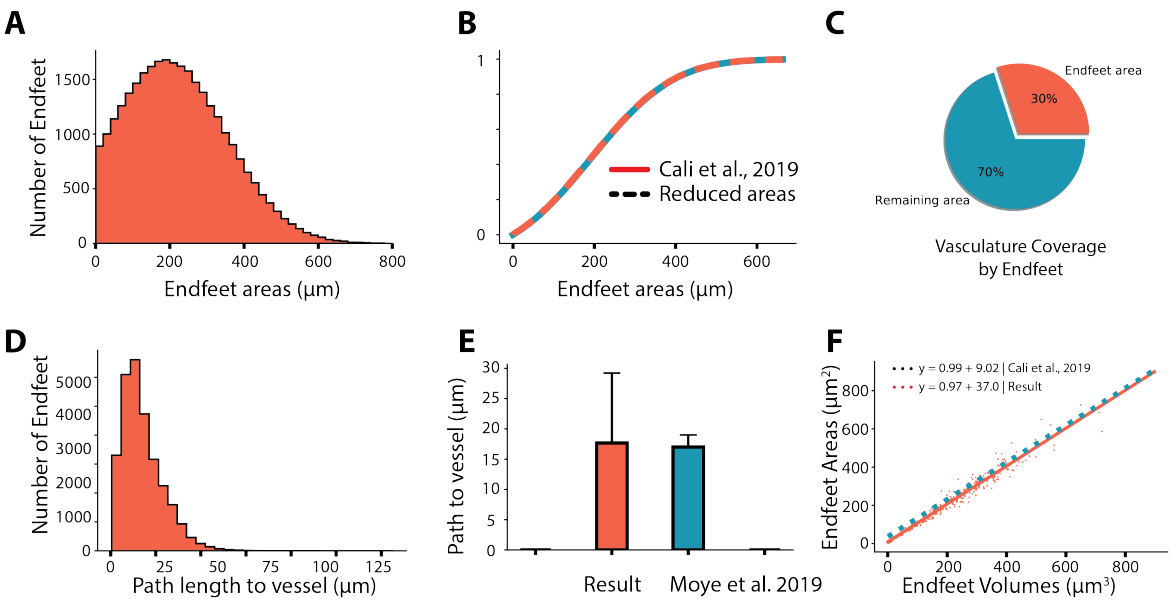

Figure 2.19 Validation of astrocytic endfeet surface meshes and processes. (A) Endfeet surface area distribution. (B) Cumulative distribution comparison between the resulting surface areas and the target ones. (C) Coverage percentage of the vasculature surface (turquoise) by the endfeet areas (salmon). (D) Shortest path length of the endfeet perivascular processes from the surface of the astrocytic soma to the surface of the vasculature. (E) Comparison of the average path length in the NGV (salmon) to the values reported by Moye et al., 2019 (turqoise). (F) Relationship between endfeet surface areas and thicknesses in the NGV circuit (salmon) and in the work of Cali et al., 2020 (turquoise).

et al. (2015). This discrepancy could be due the very few data points from which the endfeet area distribution was generated (n=7) assuming normality. The shortest path length from the soma to the surface of the vasculature was measured to be 17.23 µm on average, ranging from 0.41 µm to 110 µm (Fig. 2.19). The average path length is in agreement with the respective measurement in the work of Moye et al. (2019). However, the values were exponentially distributed resulting in a tail that increased the standard deviation of the measurements. Lastly, I validated the relation between the surface area and thickness of the endfeet geometries and validated that they were in agreement with the relationship from the study of Calì et al. (2019) (Fig. 2.19).

3

Morphological synthesis of astrocytes

3.1 Beyond neuronal synthesis

The digital reconstruction of neuronal morphologies has been gradually advancing towards high-throughput, single-neuron level and whole-brain techniques (Economo et al., 2016; Ueda et al., 2020). However, a cost-effective, large-scale, fast and highly-detailed approach is still a challenge to this day, and although there is a plethora of neuronal reconstructions available (Ascoli et al., 2007), their number is many orders of magnitude smaller than what is required to populate large scale digital circuits (Egger et al., 2014; Markram et al., 2015; Oberlaender et al., 2012).

Astrocytes pose an even greater challenge in reconstruction because of their spongiform, highly-ramified morphologies (Bushong et al., 2002). The most common approaches utilize markers that partially stain the astrocytic skeleton, such as GFAP or S100b, which capture the primary, secondary and possibly tertiary branches of the morphology (Kayasandik et al., 2020; Kulkarni et al., 2015; Lanjakornsiripan et al., 2018; Tavares et al., 2017), omitting the finer processes. Ultra-structural techniques, such as 3DEM, succeed in capturing the fine details in astrocytes, but are limited to oligocellular volumes (Calì et al., 2019; Coggan et al., 2018; Kasthuri et al., 2015). Because of the lack of sufficient numbers of detailed astrocytic reconstructions, building of large-scale networks of neurons and glia cells relies heavily on an algorithmic approach. In order to digitally generate astrocytic morphologies, an appropriate algorithm is required, which is able to generate unlimited numbers of digital morphologies that are statistically indistinguishable from their biological counterparts, and also retain the branching pattern that are observed in the specific morphological cell types.

In the previous decades, the problem of generating realistic digital cellular morphologies, has been tackled from many different directions (Ascoli et al., 2001; Burke et al., 1992; Cuntz et al., 2010; Hillman, 1979; Marinov et al., 2020), focusing into neuronal structures in particular. Bottom-up approaches emulate growth by simulating the underlying molecular mechanisms, while top-bottom algorithms capture the phenomenological behavior of structural growth, reducing it to deterministic or generative (Ascoli et al., 2001; Koene et al., 2009) mathematical models. Biophysically realistic models (Zubler and Douglas, 2008) will not be in the focus of this thesis because of their computational complexity that renders them unsuitable for the generation of large-scale circuits comprised of millions of cells.

The first phenomenological modelling approaches were based on Lindenmayer systems (Lindenmayer, 1968), reproducing the self-similar branching topology of neuronal morphologies (Smith et al., 1996) by recursively repeating a spatial code or seed (Pellionisz, 1989). However, deterministic fractal structures might look neuronal-like but they don't capture the morphological characteristics and variability of neurons, which originate from their genetic morphological phenotype (Jan and Jan, 2010; Tavosanis, 2012) and interaction with their environment (Landgraf and Evers, 2005; McAllister, 2000; Scott and Luo, 2001) respectively.

Subsequent generative models introduced the extraction of statistical measures from biological reconstructions that can be classified into two main categories: geometric and topological features. Examples of geometric measures are the branch diameter, total length, opening angles, radial and path distances. Examples of topological features are branch orders, number of bifurcations and terminations, fractal dimension etc. Statistical sampling from morphometrical distributions was combined with L-systems (Ascoli and Krichmar, 2000; Hamilton, 1993; Lien et al., 2003; McCormick and Mulchandani, 1994; Torben-Nielsen et al., 2008) or stochastically growing the morphology segment by segment (Eberhard et al., 2006; Kassraian-Fard et al., 2020; Koene et al., 2009; Lindsay et al., 2007; Wolf et al., 2013) using forward stepping rules.

The feature space of a morphology is not a well-defined entity, given that there are countless morphometrics that can be extracted, the significance of which depends on the underlying mechanisms that are sought to be understood. Therefore, generative models that sample from morphometrics define an ill-posed problem that raises the question what is the optimal selection of features and their implicit correlations that need to be implemented to reflect the branching topology of the morphology but not the intra-class variability (i.e. overfitting), which brings us back to the classification

problem (Hernández-Pérez et al., 2019). For this reason a novel algorithm was created that extracts the topological profiles of morphologies (Kanari et al., 2018) and uses them to stochastically grow new trees that capture both the statistics and the topology of the population (Kanari et al., 2020). While topological neuron synthesis has proved useful for the generation of cortical dendrites, astrocytic morphology exhibits a number of additional properties that need to be addressed. Astrocytes, more similarly to axons of neurons, take into account contextual cues during their growth. As a result a synthesis that is guided by external information is required for the computational generation of accurate astrocytic morphologies.

Although the generative approach of statistical sampling could reproduce a number of statistical properties, the morphologies were usually generated in vacuum, without being aware of physical constraints and cues. A different generative approach, proposed by Luczak, simulated neuronal growth as a diffusion-limited aggregation, demonstrating the effect of competition over resources and the spatial distribution of the latter could explain the space-delimited morphogenesis of dendrites (Luczak, 2006, 2010). In another study, Cuntz and colleagues generated morphologies, embedded in space, as a combination of a minimum spanning tree and wiring optimization constraints on a point cloud of static resources (Cuntz et al., 2010) and showed that co-synthesis can be realized as a competition over shared resources. Spatially embedded seeds were also present in the work from Runions and colleagues. Their approach grew trees based on their local proximity to the attraction seeds, which were subsequently consumed allowing for the exploration of the space for the rest of the available resources (Runions et al., 2007), instead of using the points clouds as nodes comprising the tree morphology. Other contextual cues, such as the influence of a morphology from its own processes (self-avoidance) and external molecular gradients (Grueber and Sagasti, 2010) that affect the shape of the neuronal morphology, were phenomenologically modelled as self-referential forces and successfully explained some characteristics of dendritic morphologies (Memelli et al., 2013).

Astrocytes assume complex stellate morphologies of densely ramified processes, which are distinguished into perivascular and perisynaptic depending on whether they project to vessels or not. An example of a reconstructed astrocyte morphology can be seen in Figure 3.1. The branching of astrocytic processes, unlike dendritic morphologies, exhibit locally dense regions that depend on the embedding within the brain volume and are attributed to interactions with adjacent brain structures, such as the vasculature and the proximal neurons. Studies have identified molecular mechanisms that drive endfeet

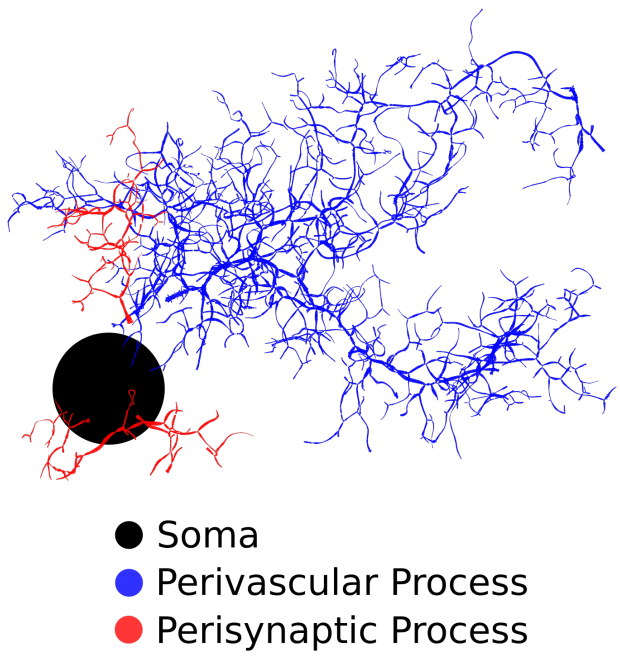

Figure 3.1 Illustration of an astrocyte morphology with perivascular (blue) and perisynaptic (red) processes attached to the soma (black). Experimental morphology data from Calì et al. (2019)

growth (Goldman and Chiu, 1984) and by extension the blood-brain-barrier maturation (Simard et al., 2003).

During development, complex molecular mechanisms take place that could explain the complexity of the morphologies of astrocytes. However, the full extent of these processes is still largely unknown. Radial glial cells (RGCs) are generated from neuroepithelial cells of the embryonic neural tube, the embryonic precursor of the CNS. They extend two processes without collateral branches, one to the ventricular wall and the other one towards the pia. Astrocytes develop from RGCs via two pathways: from glial progenitor and intermediate progenitor cells (Zarei-Kheirabadi et al., 2019). RGCs attach to the vasculature early on and they may retain these connections after differentiation to mature astroglia (Schmechel and Rakic, 1979; Zerlin and Goldman, 1997), which is promoted by the 2-way mutual induction between astrocytes and the vascular endothelium (Estrada et al., 1990; Mi et al., 2001). Due to these complex molecular mechanisms that are involved in the formation of astrocytic morphologies, the shapes of astrocytes are highly diversified and difficult to formalize and recreate with any of the described models.

In literature, there is no prior work on the in-silico synthesis of astrocytic morphologies. The most relevant work is that of Savtchenko et al. (2018), in which nanoscopic segments were stochastically added to reconstructed astrocytes from 3D EM stacks. However, this approach added branches to already existing morphologies, using an incremental strategy. Therefore it cannot be considered as a synthesis technique due to the requirement of an EM reconstruction as a starting point of the algorithm in order to create a single in-silico cell. This algorithm cannot be used for the generation of multiple unique morphologies.

In this work I built a new synthesis model, suitable for astrocytes, which combined the topological synthesis approach of Kanari et al. (2020) with a seed-based approach, inspired by the space colonization algorithm (Runions et al., 2005, 2007). A few different components of astrocyte morphologies needed to be addressed, such as the interaction with neuronal synapses to reproduce perisynaptic processes and the targeting of vasculature to generate accurate perivascular processes. Synapses extracted from the neuronal connections of a digitally reconstructed network played the role of an attraction point cloud, which guided the growth of the perisynaptic processes. Targeting to vasculature sites was addressed by introducing an attraction force field for the perivascular processes.

3.2 Topological analysis of reconstructed astrocytic morphologies

The first step in synthesizing accurate morphologies of any brain cell is understanding the properties of the reconstructed population. We start from the traditional morphological analysis, which consists of the extraction of morphometrics (Ascoli et al., 2008), i.e. features that correspond to different properties of the geometry and topology of a cell. A variety of tools have been proposed for the extraction of morphometrics from neurons (Bozelos et al., 2016; Parekh and Ascoli, 2013; Scorcioni et al., 2008). Due to the differences in the file format of astrocytes, the tools needed to be adapted to work for glia cells. For this reason, the tool NeuroM was used for the morphological analysis of neurons.

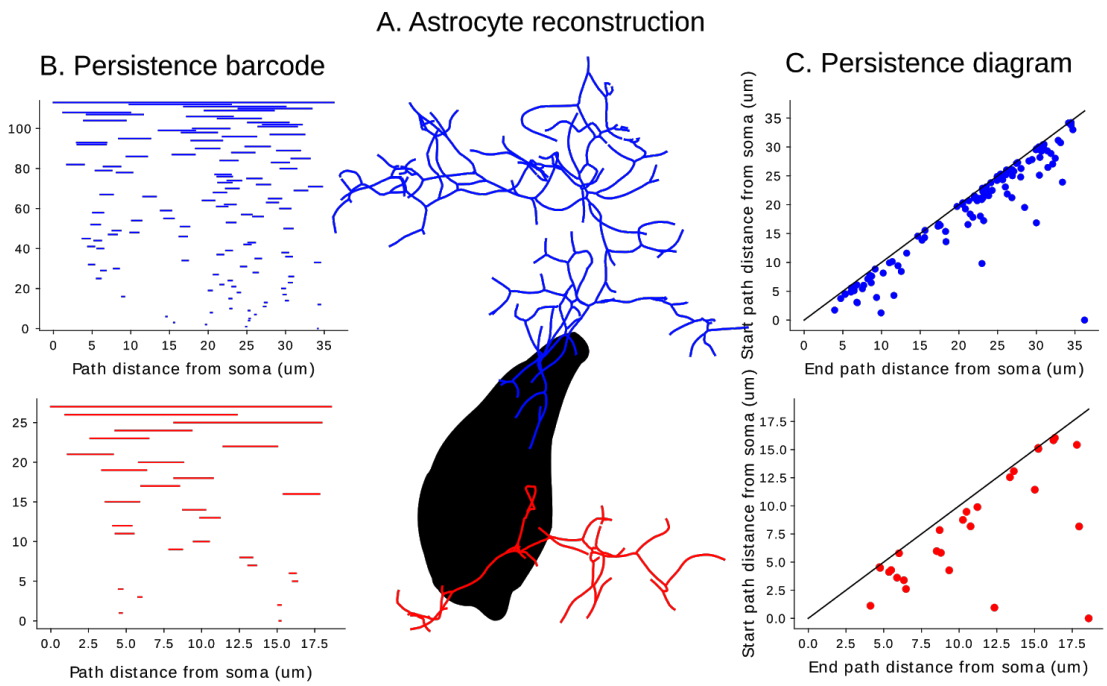

Figure 3.2 Topological analysis on perivascular (blue) and perisynaptic (red) astrocytic processes. (A) Two small branches were selected for demonstration purposes from an experimentally reconstructed astrocyte morphology. (B) Each tree is decomposed into persistent components, which are represented as a horizontal lines marking the birth and death path distance in microns for which the component remains alive. The barcode in (B) can also be represented as points in persistence diagram (C), where birth and death of each component are shown as X and Y coordinates. The diagonal in a persistence diagram corresponds to points that have equal birth and death times.

A topological analysis of neurons has been proposed by the Topological Morphology Descriptor (TMD) (Kanari et al., 2018), which encodes both the topological and the geometric properties of morphologies into a single descriptor, the persistence barcode (Fig. 3.2B). The persistence barcode of a neuron represents each branch within a biological tree as a pair of numbers which encode the start and end path distance of the branch from the neuronal soma, taking into account the topology of the branches within the tree.

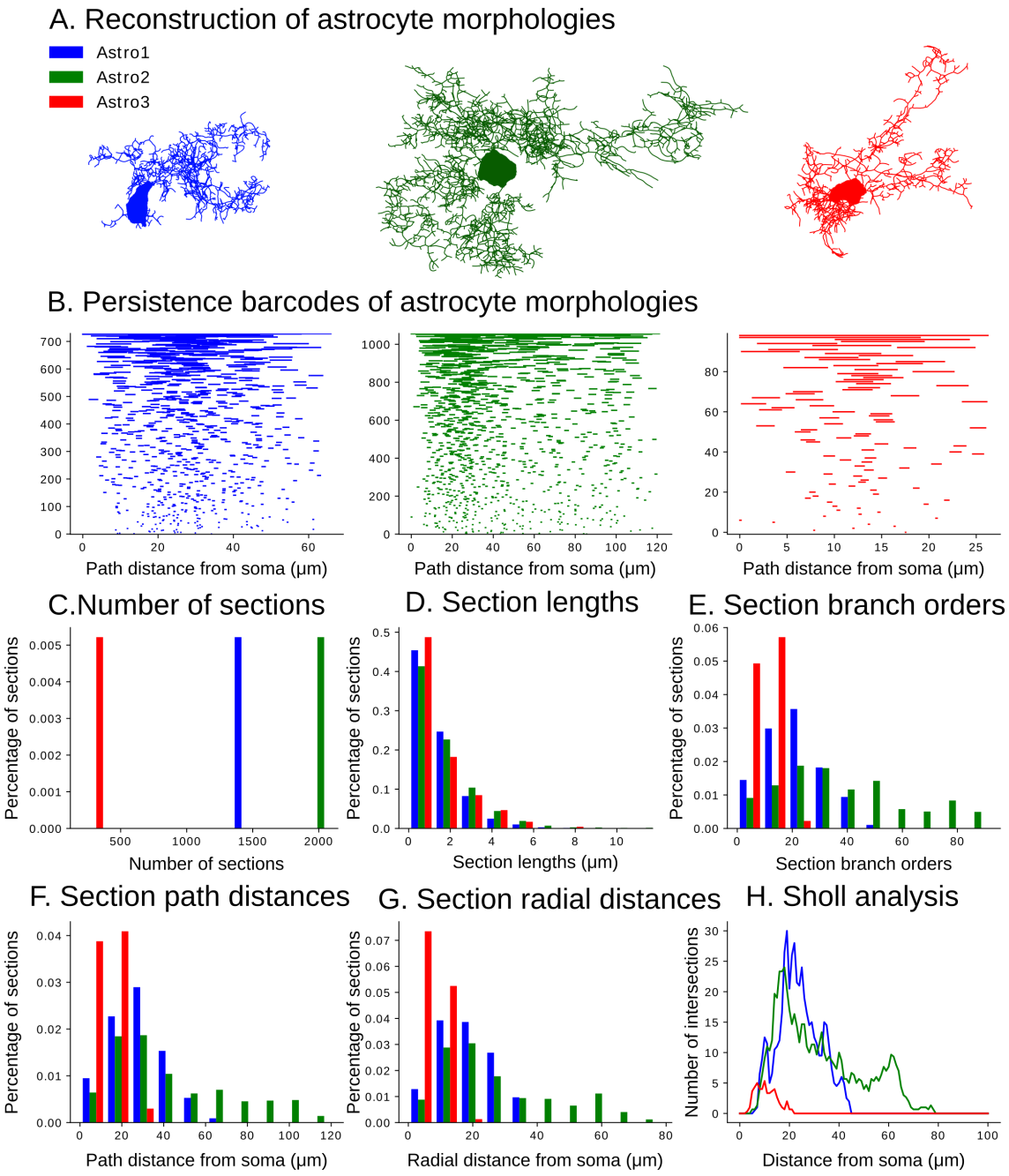

Figure 3.3 Morphological comparison of astrocyte reconstructions. A. Examples of single cell reconstructions of astrocytes (individual cells illustrated in blue, green, red). B. The corresponding barcodes of the perivascular processes. Basic morphometrics (C-H) of perivascular processes for the three astrocyte reconstructions illustrated in A.

The algorithm that extracts the TMD of a geometric tree starts by traversing all the termination nodes, or leaves, of the tree. Initially, the barcode is empty. For each

termination, the algorithm proceeds recursively along the path towards the root of the tree, i.e. the soma of the cell, and computes a reference distance, such as path or radial distance from the soma. At each bifurcation point, a bar is added to the barcode, which corresponds to the smallest branch between the two, in terms of the reference distance. Each bar encodes the start and end distance of the respective branch. The process continues until only one branch remains in the tree that extends from the maximum distance all the way to the root, this generates the final bar in the barcode which is the largest one. Since astrocytes have exactly the same tree structure as neurons (they consist of bifurcations or fork points and terminations and there exists a single reference root) the same process can equivalently be used for the representation of an astrocyte with a single topological descriptor (Fig. 3.2).

Equivalently to the persistence barcode, the persistence diagram represents the pairs of start - end distances in a two dimensional plane (Fig. 3.2C). Each persistence diagram can also be converted into a persistence image, by generating Gaussian kernels around each point in the persistence diagram and summing up their contributions into a discretized ($x-$ coordinate in M bins and $y-$ coordinate in N bins) $M \times N$ matrix $p_{kl} = (p^{00}, p^{01}, ..., p^{MN})$, where p^{kl} represent the density of points at the pixel that corresponds to the location (k, l) of the persistence diagram.

The topological difference between two persistence images, named the topological distance of two diagrams or barcodes, is defined as the sum of the absolute difference between the pixel values in the two images of identical dimensions.

$$d(Im_1, Im_2) = \sum_{0 \leq l \leq M, 0 \leq k \leq N} |p_1^{kl} - p_2^{lk}|$$

Since the value of each pixel is normalized so that the sum $\sum_{0 \leq l \leq N, 0 \leq k \leq N} p^{lk} = 1$, the difference between the pixels can take values between $(-1, 1)$.

Given two populations of astrocytes of sizes N_R, N_S, we can generate two sets of persistence images:

$$\begin{aligned} P_1 &\rightarrow \{Im_0, Im_1, \ldots, Im_{N_R}\} \\ P_2 &\rightarrow \{Im_0, Im_1, \ldots, Im_{N_S}\} \end{aligned} \tag{3.1}$$

We can then define the topological distance between the two population as the average over all the distance combinations:

$$d_T = \frac{1}{N_R \times N_S} \sum_{0 \leq i \leq N_R, 0 \leq j \leq N_S} d(Im_i, Im_j) \tag{3.2}$$

The definition of the topological distance between two populations will be used for the assessment of the quality of synthesized astrocytes in terms of their topological properties.

3.3 Topological synthesis

Apart from the challenges encountered at the description of neuronal morphologies, astrocytes present some additional obstacles. The extremely limited number of astrocytic reconstructions with sufficient details renders any statistical analysis a challenge by itself. In (Kanari et al., 2020), the authors claim that neurons with less than 5 cells are hard to describe and computationally generate due to lack of sufficient inputs. Yet, we are facing an impossible problem: to extract meaningful descriptions from only three complete reconstructions. A morphological analysis of key morphometrics of the three available reconstructions (Fig. 3.3) reveals the limitations of the most common synthesis techniques to be applied on astrocytes. The cells present high variance on basic morphometrics, such as number of sections, branch orders and distribution of path and radial distances. As a result, the description of these cells with common population measurements would not be possible as the variance is orders of magnitude higher that the average values.

A synthesis algorithm based on the topological properties of a neuron has been proposed by Kanari et al. (2020). It has been shown that the persistence barcode of different neuronal cell types is sufficient to capture the different growth mechanisms that lead to the distinct shapes of dendrites (Kanari et al., 2020). The topological barcodes of astrocytes(Fig.3.3B) can capture the key properties of their morphologies. For example, the number of branches is reflected in the number of bars in the barcode (Fig. 3.3B and C) and the path and radial distances in the extends of the branches (Fig. 3.3B and F). Therefore, TMD is a useful descriptor for the complex morphologies of astrocytes. Can this technique be used to synthesize cells with similar morphological properties to the population of reconstructed morphologies?

The TMD of astrocytes is used to define the bifurcation and termination probabilities of each branch during synthesis; the coupling of these probabilities provides a method

to implicitly reproduce key correlations between morphological features. In addition to the TMD, we need to extract some morphological features that are not encoded in the branching topology of the tree such as soma size, trunk orientation, and thickness of branches.

3.4 Space colonization terminology

A space colonization strategy (Runions et al., 2005, 2007), grows tree structures that are embedded in space competing for resources, in a similar fashion to the work of Cuntz (Cuntz et al., 2010). The main difference between these two approaches is that in the case of the space colonization algorithm the tree grows its points towards the average of the nearest attraction points (resources), instead of using them as nodes of the tree itself. Summarizing the space colonization steps: In each iteration, for each node the attraction points that are closer than an influence distance d_i are found. For each node a new direction is calculated from the average of the unit vectors to its closest points and a new point is added. Once the points are created, the attraction points that are closer to the tree nodes than kill distance d_k are removed.

The tree growing approach of the space colonization algorithm is conceptually compatible with the growing of stochastic trees, allowing for a more natural addition to TNS for encompassing spatial embedding. However, given that the algorithm generates multiple points and by extension multiple branches at each step, a major restructuring is still required, so that it is possible to work with segment by segment grown binary trees.

The influence and kill distances, which depend on the segment length L, are defined:

$$d_k = \alpha_k L d_i = \alpha_i L \tag{3.3}$$

where, α_k, α_i are the influence and kill factors respectively. Astrocyte synthesis employs a variable segment length, therefore the aforementioned factors are the parameters that will be chosen, while the length distribution is determined from the tree barcodes (see section 3.6).

The synaptic point cloud for each astrocyte is determined during the neuroglial generation stage of the NGV circuit building (see section 2.5). Thus, each astrocyte has access to a

set of attraction points, which will be used as the point cloud for the space colonization component of astrocyte synthesis.

3.5 Initiation of processes on soma

The first step of growing virtual trees is to calculate the starting point x_0 on the surface of the soma, which is represented as a sphere. During cell placement the position x_s and radius r_s of each astrocyte is calculated, and endfeet targets are generated during the gliovascular connectivity step. The microdomain tessellation is also required because it reflects the extents of each cell. Thus, each microdomain is available as a set of points and triangles.

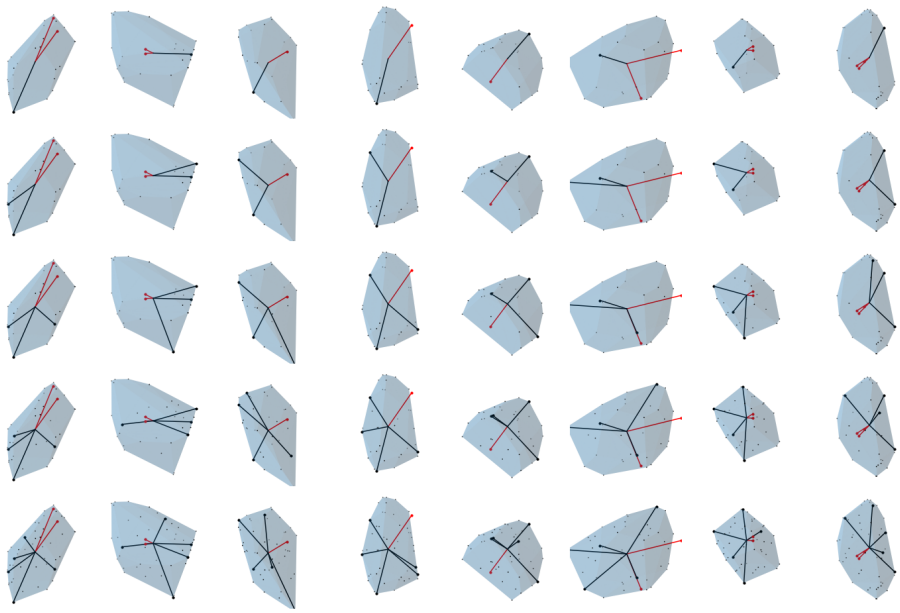

Figure 3.4 Examples of domain orientation for varying numbers of perivascular (red) and perisynaptic (black) processes.

Perivascular initial points are created first because of their dependence on the endfeet targets, which are already predetermined. An endfoot target x_t is assigned to each perivascular tree, the initial point of which is calculated:

$$d_0^{perivascular} = \frac{x_t - x_s}{\|x_t - x_s\|} \tag{3.4}$$

$$x_0^{perivascular} = d_0^{perivascular} r_s \tag{3.5}$$

Sampling from the number of primary process distribution, the total number of processes for the cell is drawn. If the total number is higher than the number of perivascular processes, then the number of perisynaptic processes is calculated from their difference. The goal for estimating the initial points for perisynaptic trees is twofold: evenly distributing the points so that the trees don't overlap and influencing their location with respect to the microdomain anisotropy. The microdomain triangles are barycentrically subdivided the number of vertices is increased tenfold, creating a dense sampling of points on the surface of the domain. The vectors from the soma center to the vertices of the triangles, that are created from the subdivision process on the domain surface, constitute the orientation vectors $V = \{ v_1, v_2, ..., v_n \}, v_i \in R^3$, from which the perisynaptic orientations will be chosen. The set of chosen orientations C is initially populated with the endfeet orientations from the previous. At each iteration a perisynaptic orientation is estimated by maximizing the cost function below and is added to C.

$$v = \underset{v \in (V-C)}{\arg\max}\, J(v) \tag{3.6}$$

$$J(v) = (1-\alpha)\frac{\sum_{v_k \in C} \theta(v, v_k)}{|C|} + \alpha \frac{\|v\|}{l_{max}} \tag{3.7}$$

$$\theta(v, u) = \frac{1}{\pi} \arccos(v \cdot u) \tag{3.8}$$

where α is the mixing factor and chosen to be 0.05, l_{max} is the maximum length of the vectors in V, and $\theta(v, u)$ the normalized squared angle function. The selection of the mixing factor prioritizes equidistribution over length bias, so that orientations are evenly distributed apart from the longest vectors that influence significantly the orientation choice. The process continues until all orientations are calculated and each perisynaptic point are calculated:

$$d_0^{perisynaptic} = \frac{v}{\|v\|} \tag{3.9}$$

$$x_0^{perisynaptic} = d_0^{perisynaptic} r_s \tag{3.10}$$

In figure 3.4, examples of orientations can be seen for varying numbers of perivascular and perisynaptic processes.

3.6 Elongation

Elongation is the process responsible from the creation of consecutive points that grow a tree. A pair of points that is created defines a segment, the length of which is sampled from a normal distribution, $L \sim \mathcal{N}(\mu_{seg}, \sigma^2_{seg})$, the mean of which are estimated from the smallest bars in the input barcode of the trees.

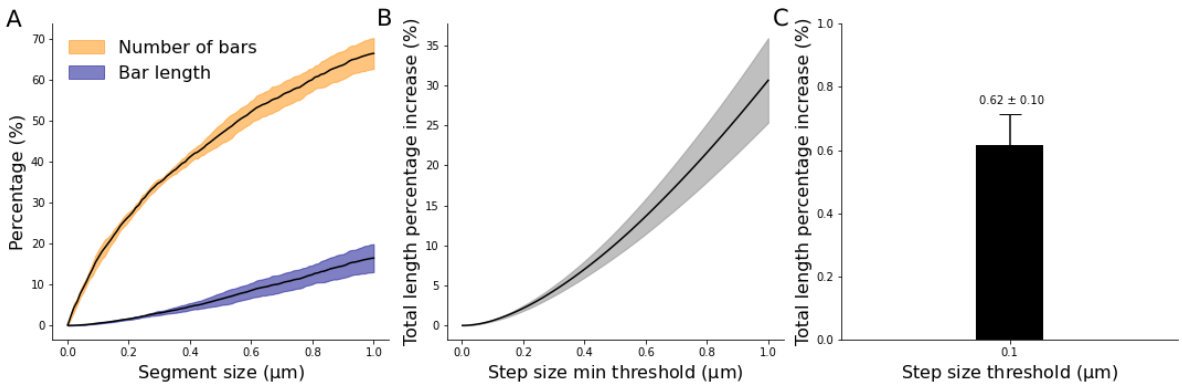

Figure 3.5 Bar length distributions. (A) Cumulative percentage of persistence bars that are smaller than segment size. (B) Total length increase in morphology with respect to minimum segment length and the exact value for segment length of 0.1 µm

In order to estimate the mean segment length, the cumulative percentage of the number of bars and bar lengths that are smaller than the segment size was plotted (Fig. 3.5A). Only a small fraction of bars (<10%) were smaller that 0.1 µm, indicating a good choice for the segment length threshold. The goal of this curation process isn't the removal of the smaller bars as it would remove branching points altering the topology, but rather the scaling of the bars below the threshold. The effect of the bar scaling was investigated in figure 3.5B, where the total length change of the morphology is plotted with respect to the chosen threshold and shows a negligible increase in total length which was quantified as (0.6 ± 0.1)µm (Fig. 3.5C). A small $\sigma_{seg} = 0.001$ was chosen to allow for a small amount of variability.

A segment also assumes a direction D_{seg}, which is a weighted sum of different contributions, giving rise to the phenomenological behavior of the cell growth. In previous work focusing on neuronal synthesis (Kanari et al., 2020; Koene et al., 2009) the direction of the segment is a weighted sum of three unit vectors: the cumulative memory M, a random vector R and a target vector T. Cumulative memory sums all previous directions, exponentially decreasing the contributions so that previous directions far in the past are quickly forgotten. The targeting vector T is calculated during branch splitting and remains unchanged during elongation.

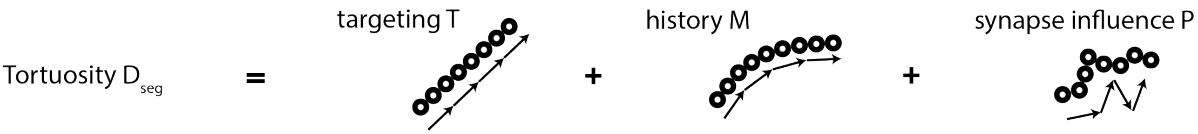

Figure 3.6 Section tortuosity is a combination of three contributions in astrocyte synthesis: targeting, history and influence from the point cloud

In this work, the stochastic interaction with the environment is not captured by a random contribution, sampled uniformly from the unit sphere, but by the unit direction to the nearest synaptic seed in the point cloud. Therefore, the segment direction, known as tortuosity, takes the form (see Fig. 3.6):

$$D_{seg} = \tau T + \mu M + \rho P \qquad \tau + \mu + \rho = 1 \tag{3.11}$$

The interplay between targeting τ and randomness ρ factors determine the degree of tortuosity of the processes. All parameters take values from the interval $[0, 1]$, therefore a configuration, for example, of $(\tau, \mu, \rho) = (1, 0, 0)$ would produce straight processes that follow the initial branching direction and exhibit no tortuosity. On the other hand, a configuration $(\tau, \mu, \rho) = (0, 0, 1)$ would generate processes the direction of which will be exclusively dependent on the closest synaptic seed. The history contribution induces a rigidity effect to the growth of the processes that reflects their intrinsic structural properties.

Following the calculation of the new direction a new point is created if it doesn't collide with the microdomain boundary. If it does collide a termination signal is sent and the elongation is stopped for the specific process. Otherwise, all the synaptic points that are closer to the new point than a kill distance $d_k = \alpha_k L$ are removed from the point cloud. The astrocyte synthesis algorithm grows the morphology trees in turn, growing by one segment each tree sequentially before growing the next segment from the same tree. This ordering of growth ensures that all trees grow simultaneously completing for the same resources, instead of favoring the growth of the tree that grows first.

3.7 Branching and termination

3.7.1 TMD dependent probabilities

The basic principle for the tree growth can be summarized by the following steps: the tree has a probability to bifurcate and to terminate associated to the path distance from the

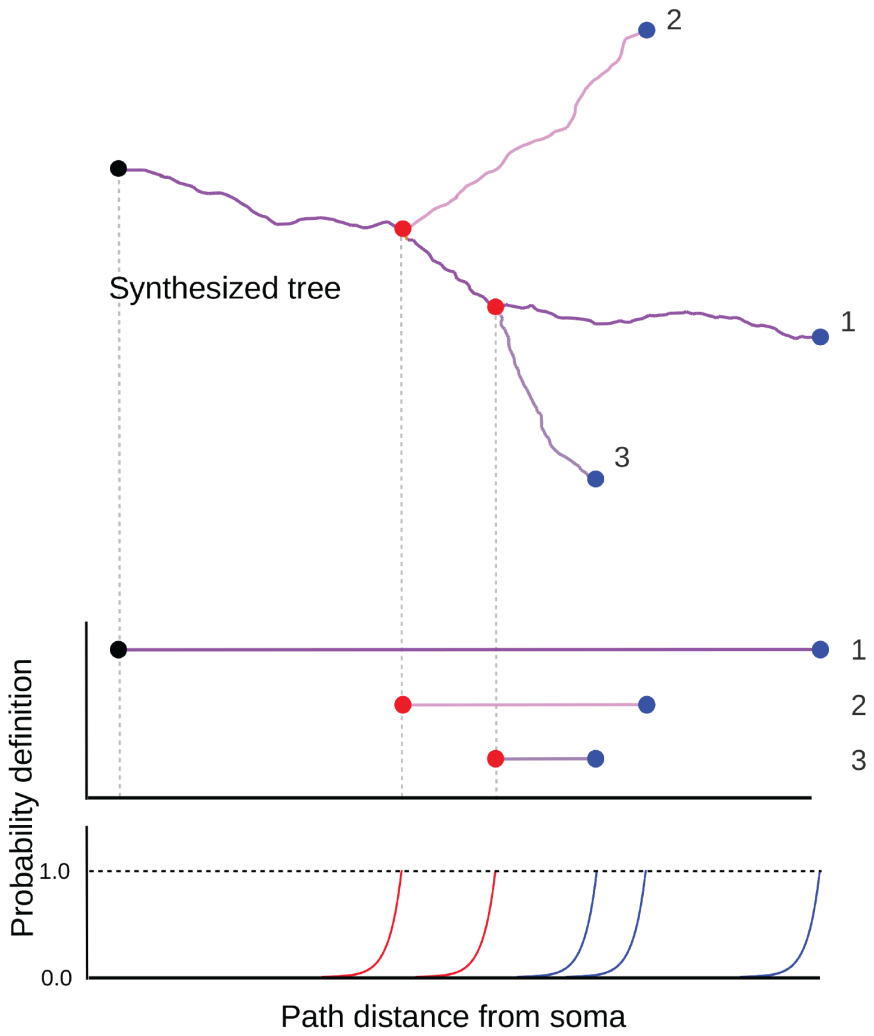

Figure 3.7 Topological branching and termination based on TMD probabilities. Example of a tree (on top) that is synthesized, bifurcations are annotated in red, terminations annotated in blue. On the bottom the corresponding persistence barcode defines two independent probabilities (to bifurcate in red, to terminate in blue) that the growth algorithm respects during synthesis.

soma 3.7. During the growth process, the topological barcode, which is extracted from the reconstructed morphology population, determines these probabilities to terminate or bifurcate. Similarly to neuronal synthesis, the bifurcation / termination probabilities depend exponentially on the path distance of the growing tip from the soma 3.7. This means that when the growing tip approaches the target bifurcation or termination distances as defined from the barcode, the probability to bifurcate or terminate increases exponentially until it reaches 1 after the target distance is surpassed.

3.7.2 Branching of astrocytes

Each growing branch of the astrocyte is assigned one of the following three "growing" types: major, secondary and endfoot. These types are essential to the growing process, because they allow different behaviors to be captured. Major sections represent the primary processes of the astrocytes that initially grow radially outwards and then ramify into the secondary branches. The first section that is generated from the initiation process out of the soma (see section 3.5), is always assigned the major type. Let a growing tip x of a branch with targeting direction $\hat{d}$ and a growing type, which encounters a splitting event mandated by the barcode. The aim of the splitting algorithm is to generate the the targeting directions $\hat{d}_1$, $\hat{d}_2$ and growing types for the children branches.

The splitting algorithm for perisynaptic processes utilizes two of the three growing types: major and secondary. The children sections receive a (major, secondary) pair if the parent is major or a (secondary, secondary) pair otherwise. The procedure uses the mean segment length μ_{seg} to determine the kill $d_k = \alpha_k \mu_{seg}$ and influence $d_i = \alpha_i \mu_{seg}$ distances, which are ubiquitous in the spatial queries around the growing tip. The repulsion points $P_R(x)$ around the tip x are defined as the subset of the morphology points P_M that are closer to x than the kill distance d_k:

$$P_R(x) = \{\, p \mid \|p - x\| \leq d_k \,\forall\, p \in P_M \,\} \tag{3.12}$$

If $P_R(x)$ is not empty, the repulsion vector is calculated by averaging the unit directions multiplied with an exponentially decaying contribution that is a function of their respective lengths:

$$\vec{r}(x) = \frac{1}{|P_R(x)|} \sum_{p \in P_R(x)} \frac{p - x}{\|p - x\|} e^{-\frac{\|p-x\|}{d_k}} \tag{3.13}$$

The repulsion contribution has a decay rate $\frac{1}{d_k}$ (see figure 3.8), utilizing the kill distance instead of an extra parameter, which makes a reasonable choice while reducing the parameter space.

The calculation of the first of the two child unit directions $\hat{d}_1$ depends on the growing type of the current section. If the current section has major type then $\hat{d}_1$ is the normalized sum of the branch direction $\hat{d}$ and the repulsion vector $\vec{r}(x)$:

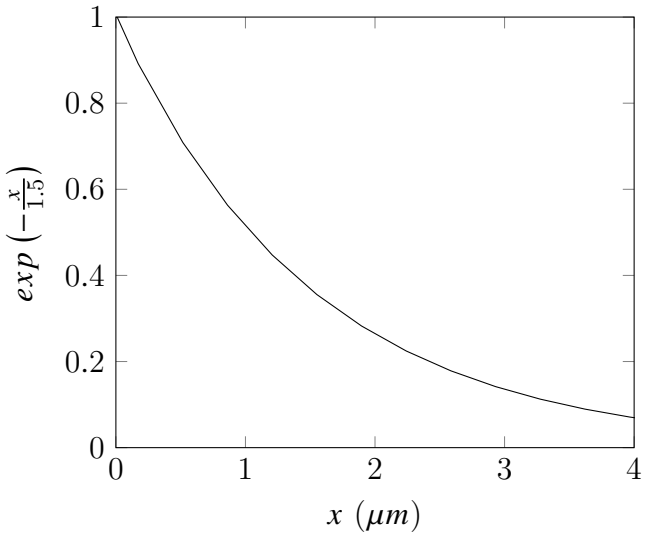

Figure 3.8 Example of repulsion contribution in the distance interval $[0, 4]$ for a kill distance $d_k = 1.5$ μm

$$\hat{d}_1 = \frac{\hat{d} - \vec{r}(x)}{\|\hat{d} - \vec{r}(x)\|} \tag{3.14}$$

If the parent is a secondary section, first the set $P_A(x)$ of attraction points in the tip proximity are determined as the points in the synaptic point cloud P_S that are closer to the tip x than the influence distance d_i:

$$P_A(x) = \{\, p \mid \|p - x\| \leq d_i \,\forall\, p \in P_S \,\} \tag{3.15}$$

and the first direction is calculated as the direction to the closest attraction point s.

$$s = \underset{s \in P_A(x)}{\arg\min} \|s - x - \vec{r}(x)\| \tag{3.16}$$

$$\hat{d}_1 = \frac{s - x - \vec{r}(x)}{\|s - x - \vec{r}(x)\|} \tag{3.17}$$

The second direction $\hat{d}_2$ is always calculated as the direction to the seed that is at the largest angle with the first direction $\hat{d}_1$.

$$s = \underset{s \in P_S(x)}{\arg\min} \left(\frac{s - x - \vec{r}(x)}{\|s - x - \vec{r}(x)\|} \cdot \hat{d}_1 \right) \tag{3.18}$$

$$\hat{d}_2 = \frac{s - x - \vec{r}(x)}{\|s - x - \vec{r}(x)\|} \tag{3.19}$$

The splitting algorithm for perivascular trees is an extension of the perisynaptic strategy with the addition of the attraction mechanics to the endfeet targets. Each tree is assigned an endfoot target x_t, which is initially active. An active target attracts major section processes of the perivascular tree until the target is reached. A bias is added to the direction $\hat{d}_1$ of the major processes:

$$\hat{d}_t = \frac{x_t - x}{\|x_t - x\|} \tag{3.20}$$

$$\hat{d}'_1 = \frac{\alpha \hat{d}_t + (1 - \alpha)\hat{d}_1}{\|\alpha \hat{d}_t + (1 - \alpha)\hat{d}_1\|} \tag{3.21}$$

where α is the target proximity factor (see supplementary section 6.1 for the derivation), which depends on the ratio of the distance from the soma to the endfoot target and the distance from the growing tip to the endfoot target.

If a growing tip x is in proximity of the endfoot target, then $\hat{d}_2$ is replaced by the direction to the target $\hat{d}_t$ and that child section is assigned the endfoot growing type which has the sole responsibility to grow towards the endfoot point.

3.8 Surface area and volume distribution

Due to a high surface-to-volume ratio in astrocytes processes, it is difficult to capture their membrane geometry using a cylinder representation. For this reason, the volume and surface of segments are separately encoded in their diameters and perimeters respectively. The model for generating synthetic diameters for astrocytes is based on the neuronal algorithm (Kanari et al., 2020). First, distributions of the model parameters are obtained from a fit to the available reconstructed astrocytes. Then, diameters are generated using parameters sampled from these distributions. The model parameters include the sibling ratio (ratio between diameters of daughter branches), diameter power relation (to model

the relative diameters between parent and daughter branches), taper rates, trunk and terminal diameters. See for example (Ascoli et al., 2008) for more details one these parameters. We deviate from the neuronal diameter model by allowing for negative taper rates, to obtain increasing and decreasing diameters with path distances. Along the neurites, diameters are bound by the trunk and terminal diameters, sampled for each neurite, while the other parameters are sampled at each segment or bifurcation.

Regarding the distribution of perimeters on the synthesized astrocytes, we extracted the diameter-perimeter pair values from the digital reconstructions and fit a linear regression model:

$$P_i = \beta_0 + \beta_1 D_i + \epsilon_i \tag{3.22}$$

where P_i, D_i are the perimeter and diameter respectively and ϵ_i the variation or noise in the data. Thus, following the diametrization process we assigned the perimeters using the linear predictor function shown above.

3.9 Results

First, I generated a number of clones (see section 3.9.1) from the available astrocyte reconstructions to ensure that the qualitative features observed in biological reconstructions can be reproduced by the proposed algorithm. As illustrated in Figure 3.9, the astrocytes reach the selected targets and present highly branching properties that are similar to their biological counterparts. Then, a full circuit of astrocytes 3.9.2 was generated and selected morphologies are presented in Figure 3.12. In both cases, the cloned and the circuit morphologies, the synthesized astrocytes present highly dense branching that spans the extents of their processes. Therefore, the proposed algorithm is suitable for the computational generation of cells that consist of highly branching, a qualitative property that is essential for reproducing the morphologies of astrocytes.

NGV circuit building generates 10000 astrocytes in approximately 6 hours in one cluster node with 32 cpus. From these, 5 hours were spent in morphology synthesis and the rest in the network data generation steps. Synthesis being the most computationally demanding stage, has been implemented to run in parallel. The current implementation uses only one node in a high-performance computing cluster, however it could use thousands to scale for bigger circuits. It is possible with my framework to create thousands of unique morphologies of astrocytes in a few hours, whereas weeks of work if not months are

required to reconstruct a single astrocyte and its environment experimentally, an issue which is apparent by the scarcity of astrocytic morphologies in the literature (Calì et al., 2019; Holst et al., 2016). In addition, the parallelized implementation of synthesis allows for the scaling of the circuit to millions of morphologies, limited only by the number of computing resources.

Another advantage of the NGV framework is that each astrocyte is "optimized" for the specific space it occupies, taking into account the synapses in its neighborhood, connections to the vasculature and homotypic neighbors. Even if thousands of astrocytes were reconstructed, they would only be suitable for the specific location and surrounding environment they have been extracted from. Experimentally reconstructing an entire region or brain down to the micrometer scale would address this problem, however it would generate one NGV circuit instance out of infinite variations that can be generated with my framework. Nevertheless, experimental reconstructions are essential for constraining the parameters of the NGV framework, therefore scientific efforts for detailed reconstructions of complex systems is of paramount importance. Algorithmic approaches, such as the NGV framework, are able to use sparse biological data to scale into entire brains with or without pathological architectures.

3.9.1 Single cell morphometrics and topology

Three clones were generated from each reconstructed astrocyte morphology, with each clone having as an input the original morphology's endfeet appositions, morphometric distributions, point cloud and branching topology (Fig. 3.9A, B). As the synthesized cell was constrained by the original morphology, it allows for the systematic study of its growth pattern without the external influence of the network organization. It should be noted that the synthesized cell morphology is still unique, regardless of the aforementioned constraints, due to the stochastic selection of the tree barcodes combined with the exponential probability of branching at a specific path length. For all the validations that follow, perisynaptic and perivascular trees were validated separately, due to their different roles and their distinct morphological properties.

A set of commonly used morphometrics were extracted from the two morphology groups. Specifically, I tested the section lengths radial and path distances, branch orders and bifurcation angles. When comparing morphometrics between groups of a small size, like in this example in which the morphometrics of 3 cells are compared with the morphometrics of a single reconstruction, the mechanism of random barcode selection can result into creating the same tree topology more than one time. This is especially often if the

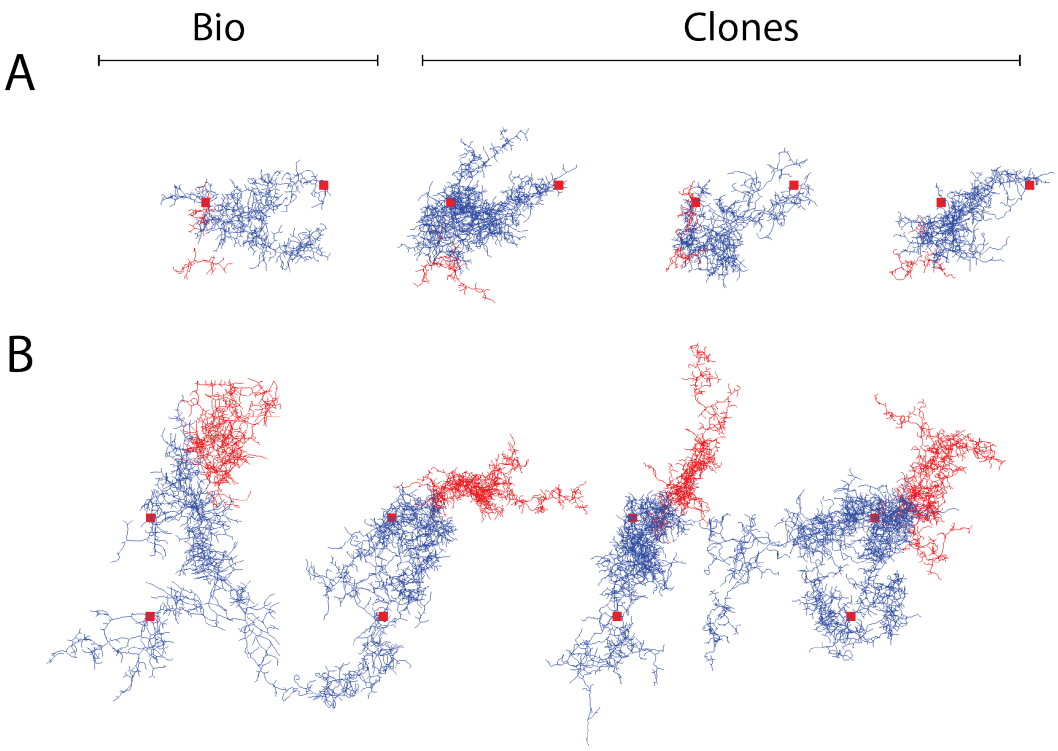

Figure 3.9 Examples of synthesized cells (clones) that are generated from the branching topology, morphometrics and endfeet targets of a single biological morphology. Perivascular processes are in blue and perisynaptic processes in red.

pool of barcodes is created from a single cell. Therefore, the probability to draw the exact combination of barcodes as in the reconstructed cell if very small. This effect can be seen in the morphometric distribution comparisons in Figure 3.10 as a shift in the distributions. Radial and path distance and section branch orders are the features that are most inflicted by the aforementioned bias. The effect is more prominent in the second cell (Fig. 3.9B), because of the larger difference between the barcodes of the trees. In all cases the astrocyte successfully grew the perivascular processes to the endfeet targets using the barcode that was available.

The topological colonization synthesis for astrocytes does not target to capture the morphometrics of a single morphology, that is to generate a morphology that is identical to the input cell. It aims instead to capture the population wide characteristics while maintaining variability by creating unique realizations from that population. Therefore, the design choice of sampling from a pool of barcodes makes better sense when a

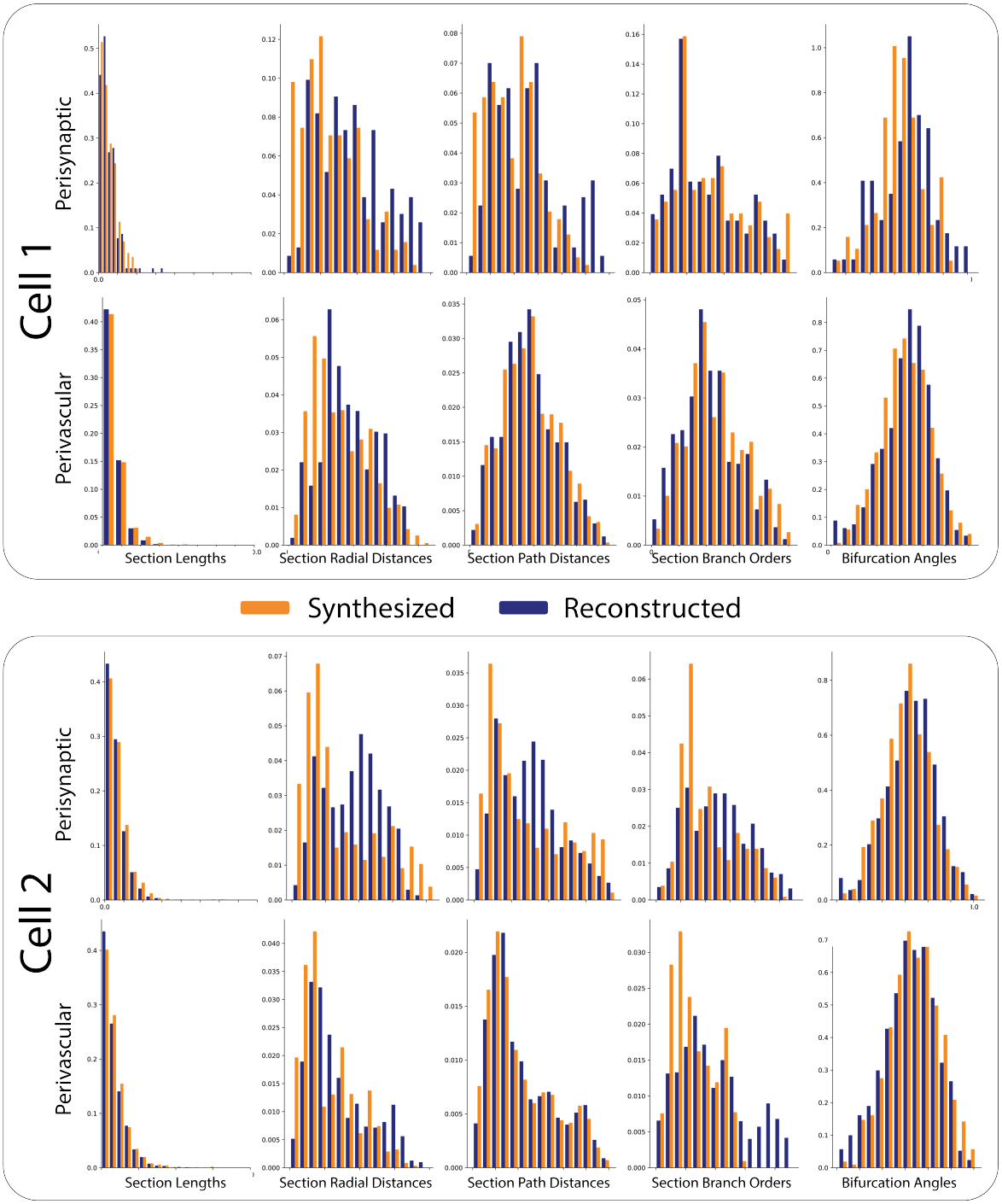

Figure 3.10 Comparison of the normalized histograms of the morphometrics of cloned (blue) and experimentally reconstructed (orange) astrocytes. Astrocyte clones are synthesized by using the persistence barcode of one cell while keeping endfeet appositions, morphometric distributions, point cloud and branching topology unchanged.

population of cells is used as an input in synthesis as we will see in the next section. Before moving to a circuit wide validation, a more meaningful way to validate the correctness of the branching structure will be presented.

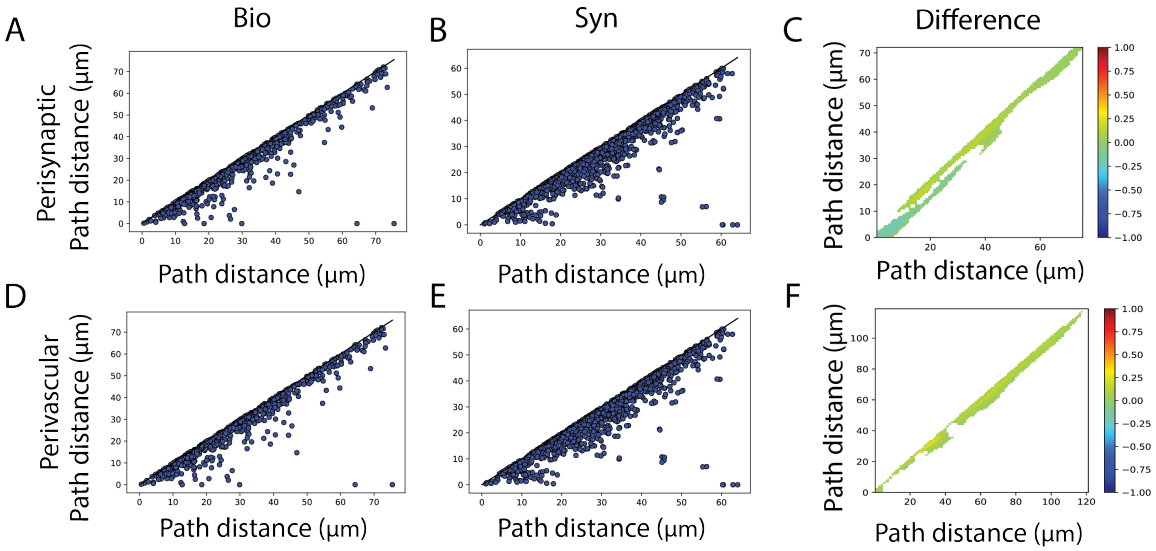

Figure 3.11 Cloned cells topology validation. Persistence diagrams for experimental reconstructions (A, D) and synthesized astrocytes (B, E). From the persistence images of the diagrams, their topological difference for each row is shown (C, F).

Persistence diagrams were extracted from the reconstructed (Fig. 3.11A,D) and synthesized-cloned (Fig. 3.11B,E) morphologies, and subsequently converted to persistence images, the pixel values of which are normalized in the $[0, 1]$. The size of the images in both axes is normalized by the maximum dimension (in µm) of our dataset.

The topological difference between the branching topologies of the experimental and cloned cells showed a less than 20% discrepancy close to the diagonal of the persistence difference. Values close to the diagonal correspond to sections that are short lived, i.e. their birth-death distance (section length) is small. This difference sources from the choice of the segment length (0.1 µm), which leads to the scaling of the bars that are shorter than that. Even though it doesn't contribute significantly in the total length of the cell (see section 3.6), it is visible in the topological difference due to the slight shift of the small branches from the diagonal. The heavily ramified nature of astrocytic morphologies results into a high branching frequency, which requires a small segment length in order to capture all the details during synthesis. Having a ten times denser sampling of points makes synthesis significantly slower when compared to neuronal synthesis that uses a segment length of 1 µm. However, it was necessary in order to capture all the smallest bars. The dense morphologies can then be re-sampled after they

are generated, reducing the number of points in longer sections and making sure that the short branches consist of at least two points, their starts and ends. Unfortunately, with the current synthesis implementation the computational overhead cannot be avoided, but in the future a variable segment length approach could overcome this issue.

3.9.2 NGV circuit morphometrics and topology

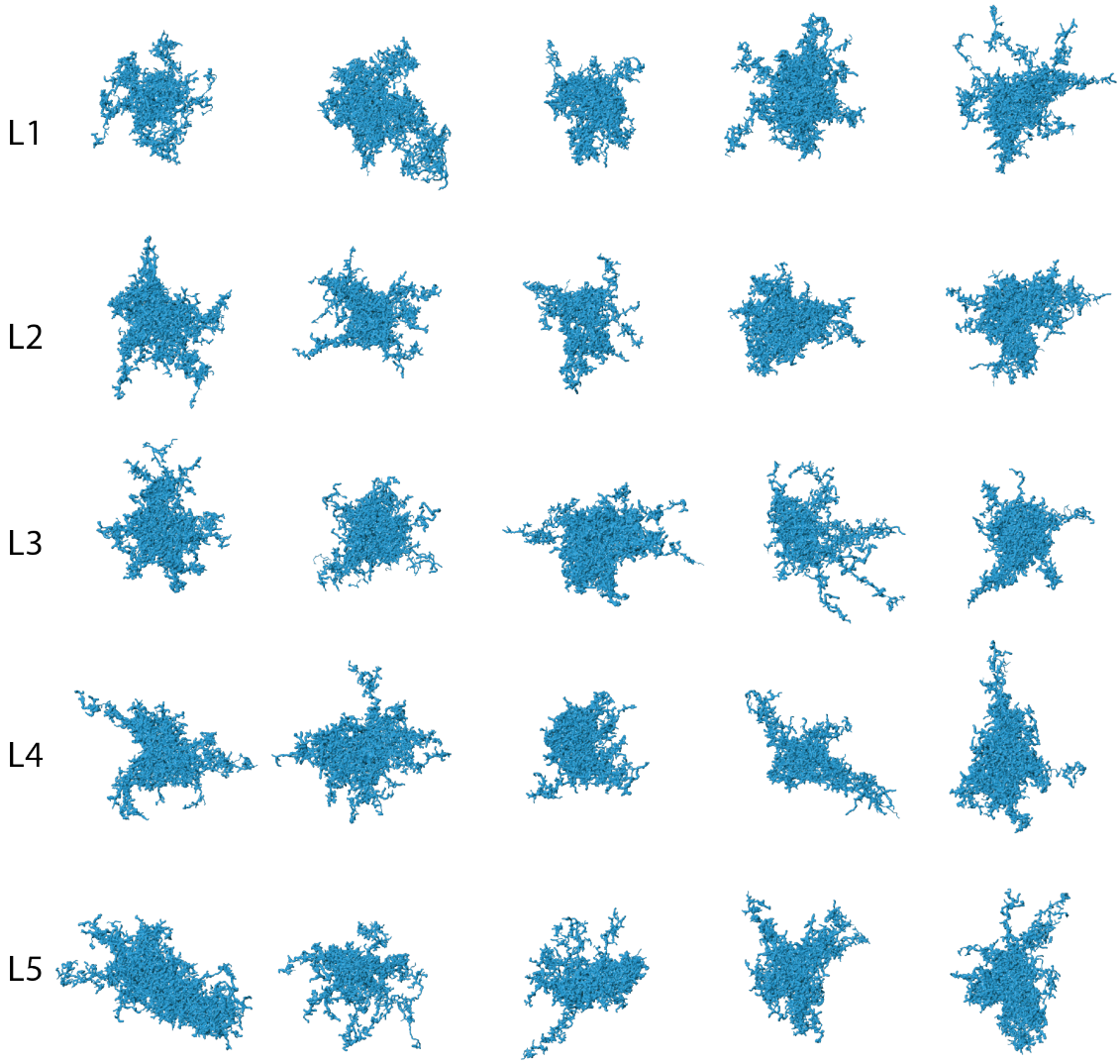

Figure 3.12 Examples of NGV Circuit astrocyte morphologies. Five astrocytes from each layers that are not in contact with the bounding wall.

In the context of a circuit, each astrocyte could sample its barcodes from all available branching topologies, which were previously extracted from the reconstructed datasets. The perivascular targets, perisynaptic orientations, synaptic clouds and domain boundaries were generated from the NGV circuit building algorithms and were used as input in synthesis to guide the growth process. Therefore, the input data for each astrocyte was unique, determined by the local environment and the size of the astrocyte domain.

Five representatives from each layer that are not in contact with the boundaries were randomly selected (Fig. 3.12) from which a set of common morphometrics were extracted, such as the number and lengths of sections, the section radial and path distances and branch orders, the remote bifurcation angles and the segment radii and volumes. The same feature extraction was applied to the experimental reconstruction and the distributions of reconstructed and synthesized morphologies were compared for each feature. The morphological analysis was applied on perisynaptic and perivascular processes separately, because of their different branching properties.

Due to the fact that topological synthesis of astrocytes uses the path distance from the soma as a metric for branching, it was expected to reproduce very well the section length and path distance distribution for the population. Radial distance distribution on the other hand, depends on the radial outgrowth of the synthesized trees. On the population level the radial distances from all experimental morphologies were pooled together, smoothing out the distributions from longer or shorter cells. Therefore when compared with a synthesized sample that drew from barcodes randomly, similar statistics can be achieved.

It was surprising that the opening angles were so well reproduced without sampling from a biological distribution. The simple rule of one child following the parent direction and the second child following the direction to the seed that is available and furthest away from the initial direction was sufficient to reproduce the angle distributions of the experimental morphologies. This suggests that astrocyte create branches in a space filling manner, as they progressively ramify during development, filling up the available space. Therefore, using the synaptic cloud, which is already available from the neuronal circuit, the biological splitting behavior can be reproduced without the need of extracting angle morphometrics from the experimental data, reducing in this way the input measurements that are required for astrocyte synthesis.

Simulation of calcium induced waves throughout the morphology requires biologically realistic surface area and volume profiles for the distribution of ion channels and trans-

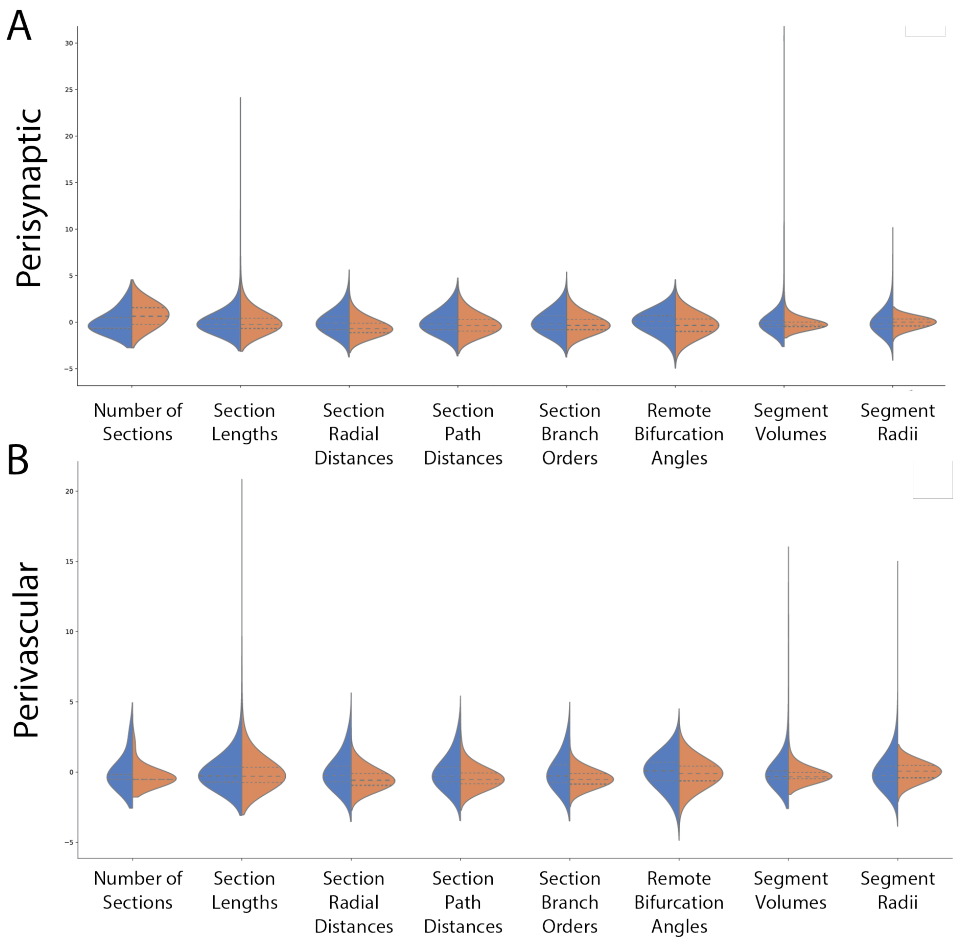

Figure 3.13 Morphometric comparison between synthesized (orange) and experimental morphologies (blue).

mission line dynamics. For this reason I computed how segment surface area and volume vary with respect to the radial distance from the soma of the astrocyte. First I grouped all segments in each morphology in perisynaptic and perivascular and sorted each segment in the group according to the distance from the segment's center to the center of the cell's soma. The sorted-by-distance segment volumes and surface areas were cumulatively summed, producing the cumulative plots in Figure 3.14. The synthesized diameters and perimeters result to a distribution of surface areas and volumes that fall within the variance of the reconstructed values. Note that the reconstructed cells assume significantly variable radial distributions, giving rise to high differences within the input population and rendering a proper modelling of diameters and perimeters difficult. More reconstructed datasets (10-20 astrocytes) would be necessary to successfully constrain the model and identify potential subtypes of astrocytes instead of pooling them together in the same group.

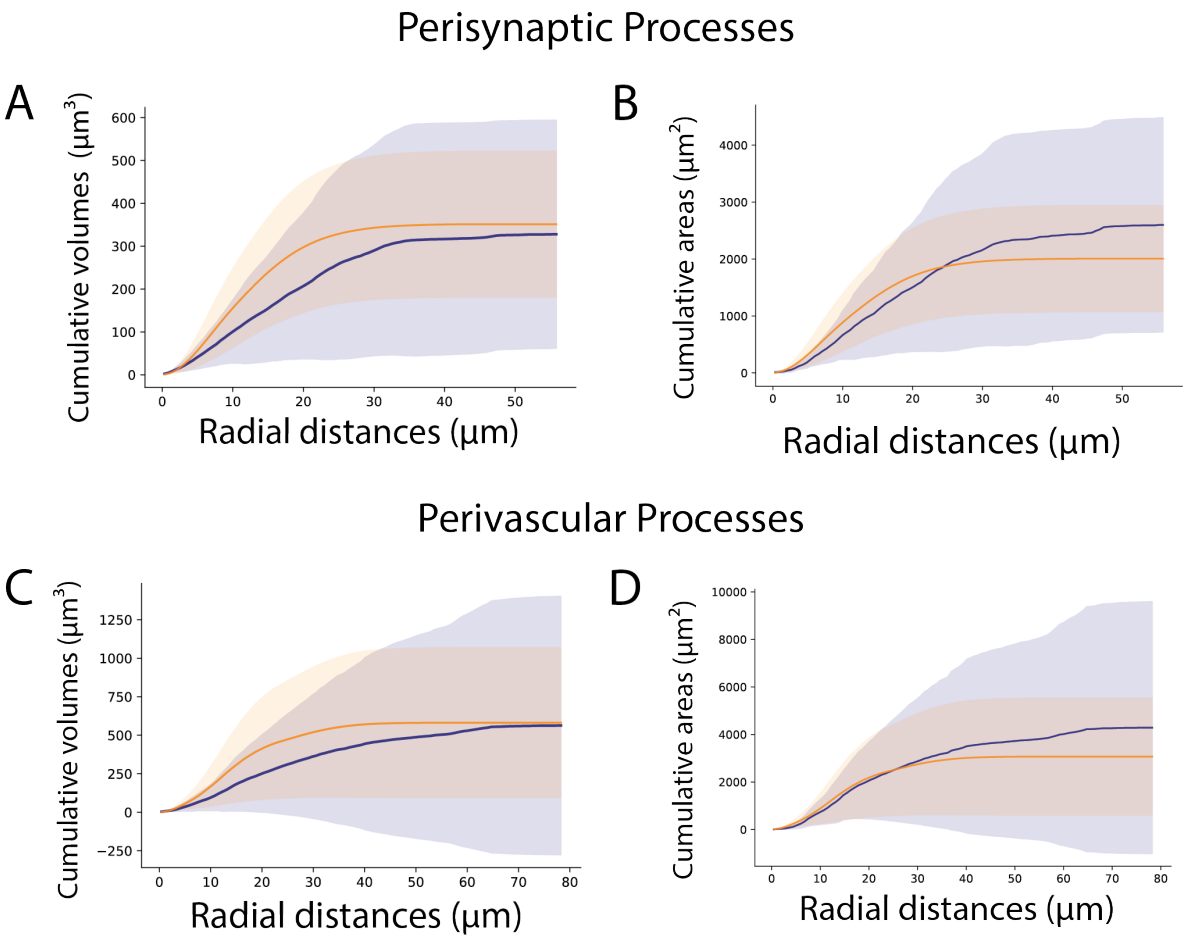

Figure 3.14 Comparison of cumulative segment volumes and surface areas between synthesized and experimental data. Blue plots correspond to experimental morphologies, whereas orange plots correspond to the synthesized population. In both plots the mean value and variance are plotted. (A,C) Cumulative segment volume plots as a function of radial distance. (B, D) Cumulative segment surface area plots as a function of radial distance.

Similarly to the single cell synthesized clones in the previous section, the trees of both reconstructed and synthesized morphologies were converted into persistence diagrams and subsequently into persistence images (Fig. 3.15A,C). The first step was to calculate the topological distance between each pair in the group of reconstructed morphologies in order to determine the error baseline within the reconstructed population. The average topological distance between reconstructed perivascular trees was 110 ± 32 units. The average topological distance of the reconstructed perisynaptic trees was 79 ± 24 units.

The next step was to calculate the average over all distances for each pair of reconstructed and synthesized morphology, grouped by layer. For perivascular processes, in layer I the average topological distance was 69 ± 27 units, in layer II 68 ± 33 units, in layer III

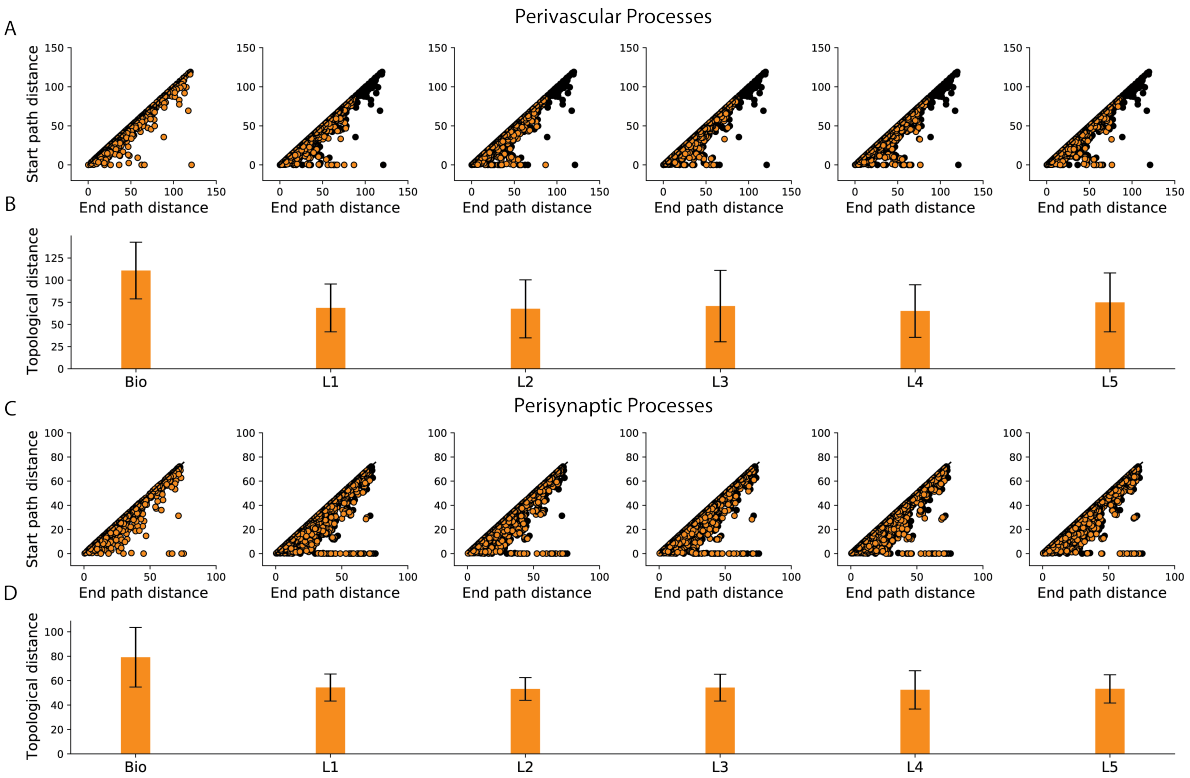

Figure 3.15 The topological distance of each layer's persistence diagram compared to the bio (black continuous line) and its respective standard error (black dashed line). (G, H) Validation of cumulative process surface area and volume as a function of the radial distance from the soma between circuit astrocytes (orange) and bio (blue)

71 ± 40 units, in layer IV 65 ± 33 and in layer V 75 ± 33 units. For perisynaptic processes, the reconstructed baseline was in layer I the topological distance was 54 ± 11 units, in layer II 53 ± 9 units, in layer III 54 ± 11 units, in layer IV 52 ± 16 units and in layer V 53 ± 12 units. These results can be seen in Figure 3.15B,D.

The comparison between the intra and per layer inter population topological distances, showed that the reconstructed trees of the astrocytic morphologies exhibited large distances even when perisynaptic and perivascular processes were considered separately. One factor contributing to this results was the existence of trees in one morphology that were very short as opposed to trees in a different morphology that were longer and spread out. Pruned trees could be result of partial reconstruction or cut from the reconstruction block. Unfortunately, given the small number of reconstructed morphologies (n=3), further classification or curation was impossible. However, the synthesized trees exhibited smaller topological distances on average because of the sampling of the barcodes.

4

Validations and predictions

In experimental setups there is a specific number of measurements that can be made, depending on the protocols that were used to stain, fix the tissue and digitally reconstruct it. Slightly different scientific questions might require starting the entire process anew with different strains of animals, transgenic or not, and weeks of work until measurements can be extracted. In-silico anatomical reconstructions of the NGV do not seek to replace the experimental setup, but to minimize the costs and time required from scientific discoveries and most important the avoidable sacrifice of animals. Algorithmically generated NGV circuits could serve as magnifying glasses into brain's complexity, allowing scientists to explore the geometry and topology of its entities and their connections. Moreover, the creation of multiple NGV circuits, each one with a different set of parameters that reflect organizational changes in brain anatomy, allow for a better understanding of the anatomical principles and their geometric constraints on brain function. All these insights could guide the scientist for the construction of focused experiments, limiting exploration as much as possible thanks to in-silico circuits. Here I present an exploratory journey into the quantification of compositional and organizational aspects of the NGV circuit.

4.1 Spatial organization of astrocytic endfeet

To gain a general overview of the spatial organization of the gliovascular elements, spatial kernel density estimate (kde) plots were generated from the points comprising these datasets. A Gaussian kernel was used for the estimation of the probability density function, the bandwidth of which (standard deviation) was determined by the Scott's rule (Scott, 2015). The plots were realized on the x-y plane, where y corresponded to the

cortical depth of the circuit. The vasculature point samples were differentiated into large vessels (Fig. 4.1A) and capillaries (Fig. 4.1B) using a diameter threshold 6 µm, which was reported for rodents in Schmid et al. (2019). In addition, two more datasets were used for the density plots: the astrocytic somata coordinates (Fig. 4.1C) and the endfeet target points on the surface of the vasculature (Fig. 4.1D). Altogether, using the four plots I sought to investigate the effect of gliovascular elements on the endfeet generation, if any.

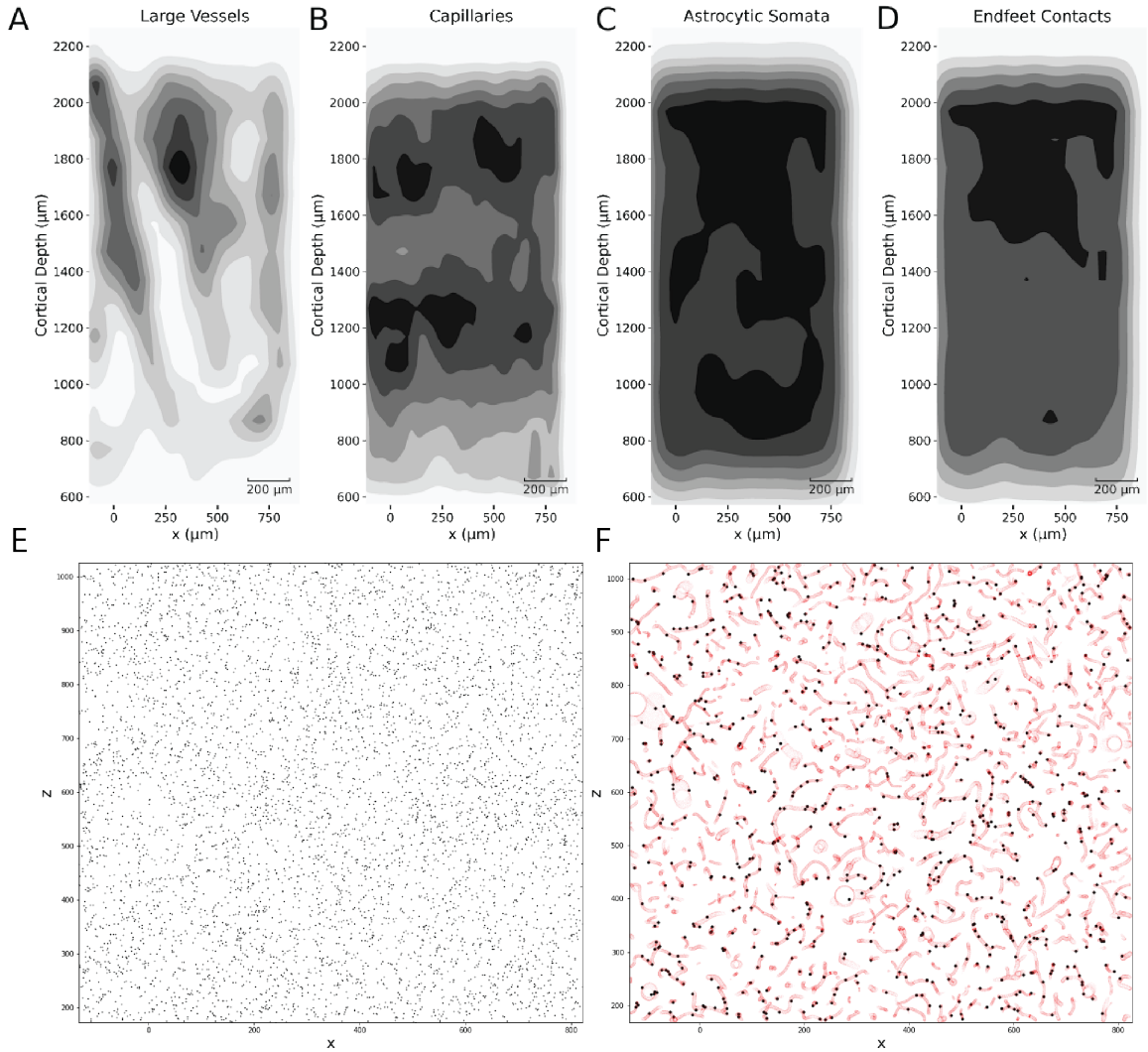

Figure 4.1 Spatial kernel density estimate plots of large vessels (A)m capillaries (B), somata coordinates (C) and endfeet targets on the surface of the vasculature (D). (E) Homogeneous distribution of endfeet targets in Layer I. (F) A 30 µm slice in layer I of endfeet targets (black) and the vasculature mesh points (red).

The density plots showed no prominent spatial correlation between the endfeet targets and either the large vessels or the capillaries. They exhibited instead overlapping density

regions with the density profile of the astrocytic somata, especially in layer I. In the NGV circuit most astrocytes produce endfeet (> 90% in the NGV circuit), therefore the higher density of endfeet in regions of high soma density was a consistent prediction. As a matter of fact the density of endfeet in the NGV circuit was measured as 23464 endfeet per mm^3 in layer V and 28421 endfeet per mm^3 in layer I. The cerebral micro-vasculature is a space-filling structure (Gould et al., 2011) that spans the entire cortical space , whilst occupying less than 5% of the total cortical volume (Heinzer et al., 2006, 2008; Serduc et al., 2006). As we already saw in the NGV circuit generation (see section 2.8.2), the astrocytic somata were evenly spaced following the density which almost doubled in layer one. Therefore, it appears the generation of the endfeet was not restricted by the vascular volume. and by extension most astrocytes always project endfeet targets to nearby vessels.

Creating a scatter plot of the target points in layer I (Fig. 4.1E) showed that indeed the distribution of the endfeet targets wasn't "trapped" by the vascular structures, rather it was homogeneously distributed throughout the available space. In addition, taking a closer look into a 30 µm slice verified that the endfeet target selection was spread out throughout the entire space, an observation that explained their spatial correlation with the astrocytic somata, but not with the vascular structures.

In conclusion, the evenly spaced distribution of astrocytic somata throughout the neuropil allows for the generation of vascular endfeet projections, which extend to the vasculature from their local environment. The space-filling organization of the vasculature in combination with the astrocytic somata spacing allows for the uniform provision of glucose and nutrient provision to the neurons (Magistretti and Allaman, 2018; Magistretti and Pellerin, 1996), which co-occupy the same space, and for an efficient recycling of water, neurotransmitters, toxic molecules and ions (e.g. K^+ clearance) (Abbott et al., 2010; Bellot-Saez et al., 2017).

4.2 Effect of astrocytic density on endfeet organization

A number of studies suggest that astrocytic density varies little across brain structures and species when compared to the variation of the neuronal density due to differences in neuronal sizes (Haug, 1987; Herculano-Houzel, 2014; Leuba and Garey, 1989; Tower and Young, 1973). As neurons increase in size in bigger brains, their density decreases leading to a higher glia/neuron ratio, ranging from 0.3 in rodents to 1.5 in humans (Blinkow and Glezer, 1968; Nedergaard et al., 2003; Pelvig et al., 2003). However, recent studies

showed that astrocytes in humans have spans twice as big as their rodent counterparts (Oberheim et al., 2009), which raises the question of how morphological constraints in a dense neuropil affect the astrocytic population.

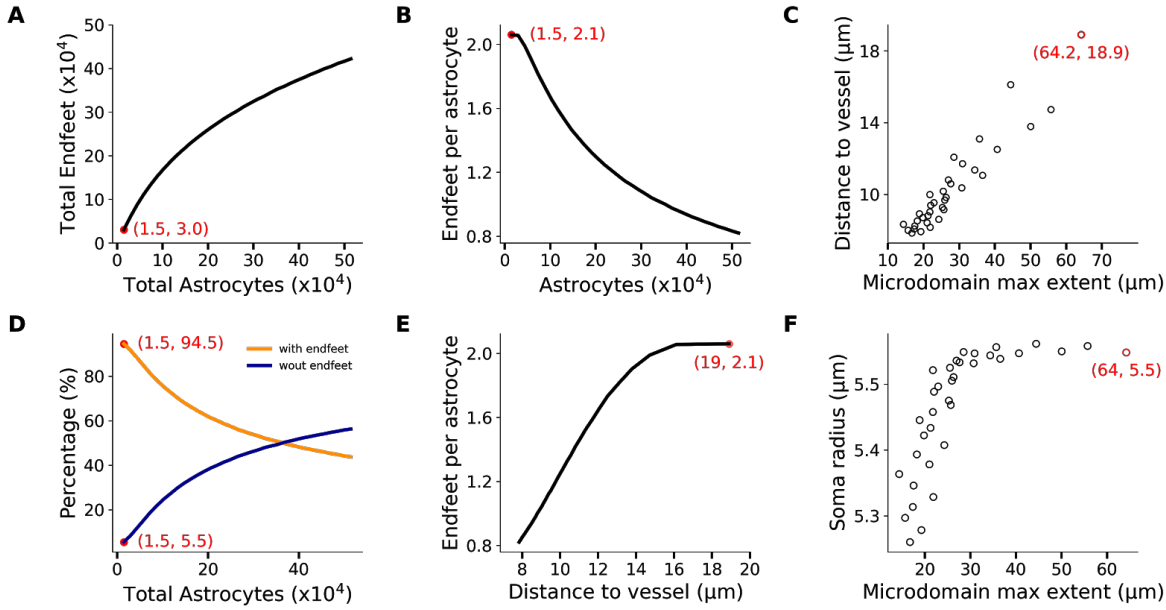

Figure 4.2 Effect of astrocyte density increase on the feasibility of perivascular processes in the same bounding space. The red data points correspond to the reference circuit with the biological parameters. As the astrocytic density increases the total number of endfeet increases sublinearly with respect to the total number of astrocytes (A), which is also reflected in the per astrocyte number of endfeet (B) and leads to smaller distances and domain extents (C). As the number of astrocytes increases, astrocytes with no endfeet increase in number (D), their distance to the closest vessel becomes smaller (E) and because of the packing there is a bias for smaller soma sizes (F).

In order to explore the structural relationship between astrocytic density and microdomains, I generated 100 NGV circuits, where cell placement, microdomains and gliovascular connectivity stages were executed. The initial NGV circuit had the default parameters and the total number of 14648 astrocytes. An uniform scaling factor was applied to the astrocyte densities for each subsequent circuit until the total number of astrocytes was scaled up to half a million. The vasculature dataset, bounding space and neuronal population remained unchanged for all circuits.

I discovered that as the astrocytic density increased, leading to a higher total number of astrocytes, the number of endfeet did not increase accordingly, but follows a sub-linear relation (Fig. 4.2A). This relation was a result of the reduction of the number of endfeet per astrocyte from an average of 2.1 to 0.8, induced by the shrinking of the microdomain bounding space, the extent of which dropped from 64.2 µm down to 15 µm (Fig. 4.2C).

A smaller microdomain extent reduces the reachable space of an astrocyte, which in turn results in the decrease of the number of astrocytes which have endfeet. Specifically, the percentage of astrocytes with no endfeet increased from 1.5% to almost 60% of the total astrocyte number in the circuit (Fig. 4.2D) and because of the tight packing, the average distance of the perivascular astrocytes to the closest vessel dropped from 19 µm to 0.8 µm (Fig. 4.2E), with their somata essentially touching the surface of the vasculature and their anatomical domains occluding access to neighboring astrocytes. In fact, the packing becomes so dense that the Gaussian sampling of the somata radii becomes skewed, thereby favoring smaller values because of lack of available space (Fig. 4.2F).

4.3 Wiring, surface areas and volumes

In order to obtain a deeper understanding of the elements that compose the gray matter of the cerebral cortex, quantification was performed of the wiring, surface areas and volumes for neurons, astrocytes and the vasculature. The processes of neurons, astrocytes, and vasculature were decomposed into segments, which populated three separate spatial indices (R-trees, Beckmann et al. (1990)), indexed by their centroid. Spatial queries were performed to extract morphological features such as process length, area, and volume for specific regions of interest, such as layers or astrocytic microdomains. I then extracted both total measurements and densities, separated by layer for the three types of entities in the NGV.

Starting with the volume fractions, I measured that neuronal processes occupied (33 ± 13) % of the neuropil, astrocytes (4.0 ± 0.1) % and vasculature (4.7 ± 0.7) % (Table 4.1). In the literature, the volume fraction of neuronal processes has been reported to be (35.0 ± 0.5) % for dendrites and (47.0 ± 0.5) % for axons in the rat hippocampus (Karbowski, 2015; Mishchenko et al., 2010). Astrocytes were reported to occupy (11 ± 4) % of the neuropil in the cerebral cortex (Dienel and Rothman, 2020; Mishchenko et al., 2010), and vasculature less 5% of the total cortical volume (Heinzer et al., 2006, 2008; Serduc et al., 2006). Vasculature volume fractions were consisted with previous experimental estimates.

The missing volume percentage of the neuronal wiring in the NGV circuit corresponds to the missing afferent fibers from outside the region of interest, which have been predicted to be approximately 41 million and would form an additional 147 ± 4 million synapses (Markram et al., 2015). Astrocytic process volume fractions exhibited a 6% compared to experimental estimates, which could not be explained in terms of missing wiring because of the localized structure of astrocytes. However, the NGV circuit models the

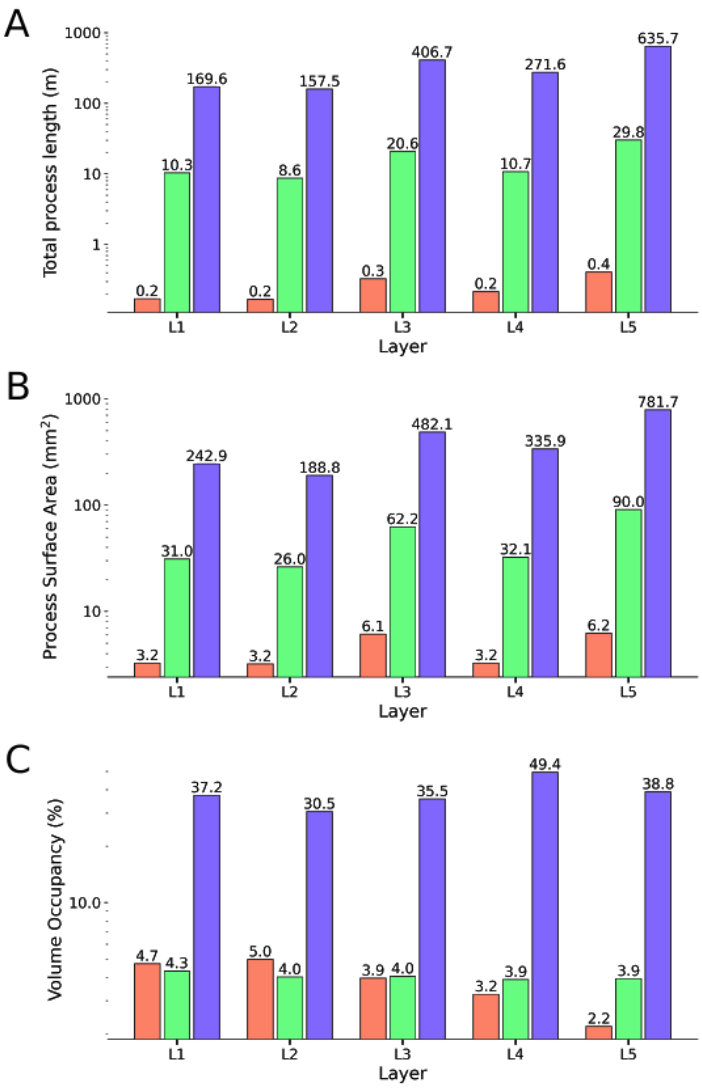

Figure 4.3 Total process (A) wiring, (B) surface areas and (C) volumes per layer of neurons (blue), astrocytes (green) and vasculature (red).

anatomical architecture of the somatosensory cortex of a P14 rat, in which the density of astrocytic somata ($(12\,286 \pm 1601)\,\mathrm{mm}^{-3}$) hasn't reached adult values ($15\,000\,\mathrm{mm}^{-3}$ to $18\,000\,\mathrm{mm}^{-3}$, Gordon et al. (2007); Leahy et al. (2013)). In addition, the degree of astrocytic ramification increases significantly from P14 to P21, in which age it converges into the mature phenotype, full of spongiform processes that cover the entire domain (Bushong et al., 2002, 2004). The synthesized morphologies of astrocytes in the NGV circuit were generated from the branching topologies of P14 reconstructed morphologies (Calì et al., 2019), which have not yet acquired the mature phenotype. Therefore, under the light of these two predicates, i.e. lower soma density and ramification compared

to mature astrocytes, the lower volume fractions in the NGV circuit were consistent compared to the reported measurements on adult rodents.

Total length (m)	L1	L2	L3	L4	L5
Neurons	169.6	157.5	406.7	271.6	636.7
Astrocytes	10.3	8.6	20.6	10.7	29.8
Vasculature	0.2	0.2	0.3	0.2	0.4
Length density (m/mm^3)	L1	L2	L3	L4	L5
Neurons	1308.9	1347.7	1467.2	1824.4	1541.4
Astrocytes	79.2	73.7	74.2	71.5	72.3
Vasculature	1.3	1.4	1.2	1.4	0.9
Total surface area (mm^2)	L1	L2	L3	L4	L5
Neurons	242.9	188.8	482.1	335.9	781.7
Astrocytes	31.0	26.0	62.2	32.1	90.0
Vasculature	3.2	3.2	6.1	3.2	6.2
Surface area density (mm^2/mm^3)	L1	L2	L3	L4	L5
Neurons	1874.9	1615.4	1739.4	2256.2	1895.4
Astrocytes	239.3	222.4	224.2	215.8	218.3
Vasculature	25.0	27.2	21.9	21.8	15.0
Total volume ($\times 10^{-2}$ mm^3)	L1	L2	L3	L4	L5
Neurons	4.8	3.6	9.8	7.4	16.0
Astrocytes	0.6	0.5	1.1	0.6	1.6
Vasculature	0.6	0.6	1.0	0.5	0.9
Volume occupancy (% of the layer volume)	L1	L2	L3	L4	L5
Neurons	37.2	30.5	35.5	49.4	38.8
Astrocytes	4.3	4.0	4.0	3.9	3.9
Vasculature	4.7	5.0	3.9	3.2	2.2

Table 4.1 Quantification of the total wiring, total surface areas and volume fractions for neurons, astrocytes and the vasculature and for each layer in the NGV circuit.

Apart from volume fractions, which are usually reported in the literature, I also measured surface area and length of all three entities in the NGV circuit, both in absolute and density representation (Table 4.1). Neuronal process total length ranged from 120 m in layer I to 657 m in layer V, two orders of magnitude higher than astrocytic process length, which ranged from 1.4 m to 3.5 m in layer V and three orders of magnitude higher than vasculature wiring, which ranged from 0.2 m in layer I to 0.5 m in layer V. Total Surface area for neurons ranged from 242.9 mm^2 in layer I to 781.7 mm^2 in layer V. Astrocytic processes surface area was measured from 31 mm^2 in layer I to 90 mm^2 in layer V. Finally, vasculature surface area ranged from 3.2 mm^2 in layer I to 6.2 mm^2 in layer V. The ratio of the total length between neurons and astrocytes was 20 ± 3 and between neuronal and vascular total length was 1347 ± 372. The total process surface ratios were 8 ± 1 and 98 ± 29 respectively.

Following the quantification of the geometrical features of neurons, astrocytes and the vasculature, it was apparent that there was a systematic order-of-magnitude difference between them. The data suggested there is a hierarchy in cortical composition, the origin of which has been theorized in terms of length (Klyachko and Stevens, 2003; Wen et al., 2009), conduction delay (Budd et al., 2010), volume or/and spine economy (Karbowski, 2015) minimization. Most importantly, I have shown here that an in-silico circuit of the NGV architecture can indeed be used to investigate questions concerning the intricacies of cortical composition and their relation to computational capacity.

4.4 Astrocyte-related numbers

In this section I will focus into the central player of the NGV architecture, the astrocyte. Due to the fact that the gliovascular interface has been extensively analyzed in the validation of the NGV model, I extracted two quantities that were not found in the literature, namely the total endfeet surface areas for each astrocyte. The median of the total endfeet surface areas per astrocyte was 427 μm^2 with a 95th percentile of 992 μm^2 (Fig. 4.4A), and the median of the total endfeet volume areas per astrocyte was 414 μm^3 with a 95th percentile of 962 μm^3 (Fig. 4.4B).

The neuroglial interface consists of the connections between neurons and astrocytes via the formation of tripartite synapses. Each astrocyte domain connected to 627 ± 259 neurons via tripartite synapses (Fig. 4.4C), whereas 6 ± 4 neuronal somata were in contact with each microdomain. The number of neuronal somata per astrocyte was in a consistent range compared to reported numbers of four to eight neuronal cell bodies

per astrocytic domain in the rat hippocampus (Halassa et al., 2007b). The median of the number of synapses per microdomain was 3010 and the 95th percentile was 7175 synapses. Compared to the 100000 synapses per domain that have been reported by Bushong et al. (2002), the circuit numbers fell short, although this discrepancy has been encountered before and was due to he missing afferent fibers, mostly long range projections (Stepanyants et al., 2009). Taking into account the missing synapses from the external connections would result into a synapse density of (0.9 ± 0.1) synapses/μm^3 for layers I-V (Santuy et al., 2018), the predicted median for each microdomain would be 71995 and the 95th percentile 134010 synapses, which is consistent with the literature.

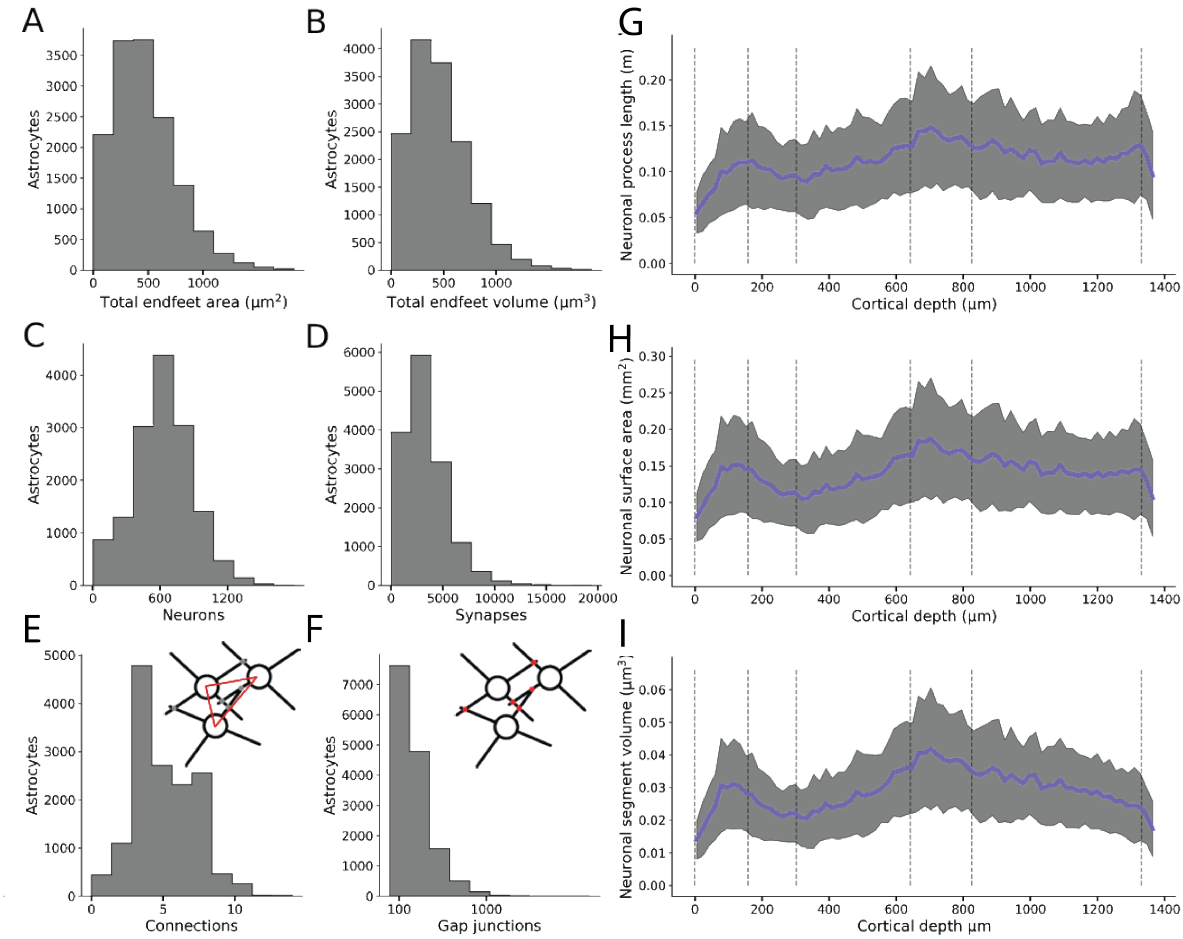

Figure 4.4 Quantification of the astrocytic interfaces. Histograms of per-astrocyte total endfeet area (A), volume (B), connected neurons (C), connected synapses (D), astrocytic neighbors (E) and gap junctions (F). (G-I) Neuronal processes total lengths, areas and volumes per microdomain and across the cortical depth. Purple line represents the average and the gray area the respective standard deviation.

The astrocytic syncytium is formed via gap junctional connections, established in the overlapping interface between each astrocyte and its neighboring astrocytes. The NGV

circuit astrocytes formed 5 ± 2 connections with their neighbors (Fig. 4.4E). In the study of Xu et al. (2010), the inter-astrocytic connections were estimated to 11 ± 3 connections, ranging from 6 to 15 in hippocampal slices from P21 to P25 rats (Xu et al., 2010). In order to discern if the source of this significant discrepancy in the emergent connections of my model was either a geometrical restriction resulting from the domain tessellation or morphological artifact, I calculated the number of neighbors per astrocyte based on the domain tessellation (using only the polygons). Therefore, analysing the incident domains to each domain resulted to 15 ± 3 neighbors per astrocyte, which were notably higher than the connections established from the gap junctions. The connections were calculated from the detection of the intersections (touches) between neighboring morphologies. The median number of gap junctional connections were found to be 198, with the 95th percentile being 609 (Fig. 4.4). The exponential distribution of the gap junction numbers in combination to the available neighbors signified that the NGV astrocytes, not being yet fully mature, they didn't exhibit an extensive ramification, allowing for a uniform interface across the boundaries of the domain. Rather the primary processes reached the boundaries of the domain and penetrated into neighbor territory forming a lot of close-together touches (in small distances). This is indeed how astrocytes form connections with their neighbors while developing and before reaching the maturation stage (Bushong et al., 2002, 2004; Ogata and Kosaka, 2002). There is however space for improvement in my model so that astrocytic processes could optimally cover the extents of the domain and connect to more neighbors as reported in experiments.

On a microdomain basis, I calculated the total wiring, surface area and volume of neuronal processes for each microdomain across the cortical depth of the somatosensory cortex (Fig. 4.4G-I). The total process length density per microdomain was calculated for all neuronal morphologies and found to range from 1 to 2 μm/μm3 across all layers. The average number of neurons and synapses per astrocytic microdomain were 250 and 3000 respectively (Fig. 4.4D,E)

5

Conclusions and future work

5.1 Conclusions

Astrocytes extend ramified processes to the vasculature and neuronal synapses, creating reticular highways for neuronal trophic support, homeostatic control (ions, water), and multi-directional signaling to and from the vasculature, neurons, and neighboring astrocytes. The plethora of complex biological mechanisms that arise from the neuronal-glial-vascular (NGV) ensembles and how they support brain function have not been completely understood. This is because we lack an understanding of the detailed anatomical organization of the NGV that forms the foundation for these interactions.

In this thesis, I created for the first time a data-driven digital reconstruction of the neuronal-glial-vascular (NGV) ensemble at a micrometer anatomical resolution. I used sparse data from numerous studies to build an NGV circuit of 14648 protoplasmic astrocytes and 88541 neocortical neurons, forming a functional column of the P14 rat neocortex with its microvasculature. I designed an algorithmic framework for constructing large-scale networks of neurons, astrocytes, and the cerebral microvasculature to achieve this. Previous work on the digital reconstruction of neuronal networks was extended with a new pipeline to include astrocytes, the vasculature, and reconstructing their pairwise connectivities: neuro-glial, glio-vascular, and glial-glial.

The first step was to generate the spatial organization of the astrocytic syncytium based on experimental data. The reproduction of both the spatial frequency and dispersion of astrocytic somata was achieved by developing a novel method that allowed the somata' placement at a specific density and distance to their closest neighbors while avoiding

collisions with geometric entities co-occupying space. Previous cell placement models generated positions without considering their spatial embedding and dispersion, which is an essential feature of the astrocyte's tiling organization. This method successfully reconstructed the key properties of the astrocyte positions from which stellar morphologies are grown.

Instead of growing the astrocytes simultaneously, searching for connections, interacting with their neighbors, and remodeling to form a tiling organization, I turned the problem on its head by first partitioning the cortical space into polygons (anatomically exclusive regions of the astrocytes) and then process each astrocyte region independently. This approach converted a computationally intractable problem into an embarrassingly parallel one, which scales efficiently to any number of astrocytes. Furthermore, to make the domain size proportionate to the soma dimensions, I modeled the polygon generation as a power diagram in which the soma's radius influences the size of the domain. I also successfully reproduced the overlapping interface of neighboring astrocytes by applying a uniform scaling of the domains until they reached a 5% volume overlap with their neighbors. Each domain polygon delimited the accessible vascular branches and synapses for each astrocyte, and all connectivity methods, apart from the glial-glial that required the entire astrocytic population, were calculated independently.

The gliovascular connectivity was established within each astrocyte domain by first distributing potential targets on the vascular branches and sampling the number of endfeet from a distribution with an average value of two, according to literature data for P14 rats. Which targets should we select and with what kind of relation to each other? To answer this question, I analyzed the endfeet geometry in the reconstructed astrocyte morphologies and created a selection strategy that incrementally selected the closest targets from different branches by maximizing the distance to previously selected ones. The endfeet surface geometry was then reconstructed from the competitive propagation of 2D waves along the vasculature surface geodesics, constrained by reported area distributions. The neuroglial connectivity was established by randomly selecting a subset of the synapses inside the astrocyte domain.

The last and most complex stage was to grow detailed stochastic astroglial morphologies, constrained by the per-astrocyte data produced in the steps above. Thus, astrocytes were grown in space, targeting the endfeet vasculature sites, using the available synaptic cloud to influence their growth, replicating the branching topology of the experimentally-reconstructed cells. Perisynaptic process orientations were distributed based on the microdomain's orientation, which also constrained the cell's overall growth. To make this

possible, I developed a novel algorithm that combined the topological branching and space colonization methods using the neuronal synapses as a point cloud of attraction seeds. Following the morphology generation, the glial-glial connectivity was generated based on the overlapping geometries between neighboring astrocyte morphologies. The neuroglial connectivity was defined by assigning the astrocyte morphology's closest segment to each neuronal synapse, starting from the available synthesized morphologies of astrocytes.

The topological branching synthesis for astrocytes is a paradigm shift from existing approaches, limited by the small number of digitally-reconstructed morphologies. Instead of relying on the existing reconstructions available from biological experiments, I computationally generated a large number of morphologies of astrocytes based on the extracted branching topology of the astrocytic reconstructions. This framework allowed the generation of an unlimited number of morphologies, which replicated the input exemplars' biological branching topology, yet have grown into unique, space-embedded, and context-aware entities. The integration of additional data concerning different astrocytic types will incrementally add morphological variability into the NGV circuit.

The NGV circuit was validated against numerous literature sources to ensure its biological fidelity. It successfully reproduced the spatial organization, dispersion, and geometric characteristics of the astrocytic somata. In addition, the astrocytic somata were placed without collisions with other somata or the vasculature geometry, reproducing the physical limitations and occupancy that naturally emerge in a biological network.

The domain volume distribution was consistent with reported estimates on juvenile rodent brains, whereas there was no notable difference between the overlapping and non-overlapping volumes due to the small overlap factor. Most importantly, the NGV circuit's domains reproduced literature findings of decreased domain sizes in layer I, resulting from the increased astrocyte density in said layer. This result confirmed that astrocytic shapes are indeed susceptible to purely geometric constraints induced by their contacts and spatial organization.

Cells were generated with perisynaptic and perivascular processes connecting astrocytes to the synaptic cleft and vascular sites, respectively. The number of vascular sites was sampled from biological data. The emerging astrocyte distance distribution to the vasculature and neuronal somata was in agreement with experimental measurements, which suggested that the organizational relationship between neurons, astrocytes, and the vasculature does not exhibit a specific spatial pattern. Instead, it only depends on the somata distribution and physical limitations.

The digital reconstruction of the endfeet areas on the vasculature's surface followed the constraints extracted from the literature estimates. However, when the surface meshes were pruned to reach the target distributions, the vasculature's respective total coverage dropped from ~ 91% down to ~ 30%. Thus, I discovered that the specific combination of constraints (astrocyte densities, number of endfeet, and endfoot area distributions) was impossible to result in the expected biological coverage of ~ 60%, indicating an inconsistency in the values reported in the literature. This discrepancy illuminated the power of using a computational model to uncover the geometric underpinnings that govern the NGV architecture.

Topological astrocyte synthesis was first validated for its ability to reproduce unique morphologies. Thus, each reconstruction was decomposed into a pool of barcodes, and multiple cells (clones) were synthesized from each barcode pool. All the cell characteristics, such as the number of trees, endfeet targets, and soma size, remained unchanged. The morphometrics were in agreement with the reconstructed ones. However, because of the random selection of barcodes from the pool for each cell realization, the exact configuration of barcodes that comprise the initial cell rarely occurs. Since each barcode may appear more than once in the resulting morphologies due to the random sampling, the morphometric distributions, especially radial and path distances, could be skewed. This behavior was anticipated because of the topological synthesis's design to capture the variability of the population instead of reproducing exact cells. In addition, this effect is more severe when few sample morphologies are available, which results in the high variance of single cells within the input population. The topological comparison exhibited a difference close to the diagonal of the persistence diagrams, a result caused by choice of the minimum segment length (0.1 µm), which resulted in the scaling of smaller branches to that value. This difference, however, was measured to negligibly affect the total length of the cell.

After validating that the synthesis method could successfully reproduce the topologies of astrocytes starting from a single cell, I validated the circuit morphologies synthesized inside the NGV network. The population morphometrics matched the reconstructed ones, and the topological distance between the population in each layer and the biological cells was smaller than the topological distance within the group of biological reconstructions. The space colonization component of the model succeeded in reproducing the branches' bifurcation angles without sampling from morphometrics. Finally, synthesized astrocytes accurately reproduced the surface areas and volume distributions, which are essential for modeling their functional properties.

The NGV circuit provided access to a plethora of measurements that I collected as exploratory predictions of the underlying biological complexity. Analysis of astrocyte somata's spatial densities, vasculature, and endfeet unveiled that astrocytic endfeet are homogeneously distributed in space due to the space-filling geometry of the vasculature. This geometrically-constrained architecture allows for a spatially-continuous provision of trophic support to neurons throughout the cortical space, which only varies with cortical astrocytic density. Thus, the tiling astrocyte compartmentalizes the vasculature, and their endfeet optimize the communication wiring from the endfoot to neurons. Given the relatively low density of astrocytes compared to neurons, this endfeet organization and coverage would be impossible if astrocytes did not partition the cortical space with the anatomically exclusive regions, leading to insufficient trophic support.

Multiple circuit realizations of increasing astrocyte densities were generated to explore how endfeet appositions vary with respect to the number of astrocytes. Specifically, I evaluated the effect of increasing the astrocytic density, up to half a million astrocytes, on the network's gliovascular connectivity. I found that as the total number of astrocytes increased, their overall extent shrank due to their tight packing, reducing their access to vascular sites. However, the astrocyte number increase did not compensate for the drop in endfeet numbers due to the tight packing of domains that prevented astrocytes from projecting to the vasculature. In contrast to neurons, astrocytic density varies little in different species and animal ages. My experiments indicated that the contact spacing behavior, which gives rise to anatomically-exclusive domains, acts as a global constraint for the astrocytes' morphological steady state, which is reached at one month of age in rodents. In addition, for the morphological domain to include the vascular sites within reach, a specific range of spacing is required, which depends on the inter-vessel distance. Therefore, the astrocyte's role in providing trophic support polarizes its morphology and constraints its location to maximize the connections from the vasculature to neurons.

Delving deeper into the NGV quantification, I extracted the per layer lengths, surface areas, and volumes, both in terms of total and density measurements. Compared to reported biological numbers, the volume fractions of neuronal processes were smaller than the values reported in the literature due to the missing afferent fibers that reached the circuit from outside. Also, the lower average density of the P14 rat neuropil combined with the partially ramified morphologies resulted in a volume occupancy that was 6% lower than reported values for adult animals. The quantification of the geometric features of all three elements in the NGV verified the emergence of a systematic order-of-magnitude difference in the cortical composition that has been observed in experimental studies.

This finding proved the usefulness of the model to study the emerging organizational properties of NGV ensembles. The unique morphological characteristics of all three entities are sufficient to explain this hierarchy. Vasculature's low density accounts for the lower end of this hierarchy, whereas neuronal wiring was measured approximately 20 times higher than astrocytes and 1000 times higher than vasculature. Astrocytes are locally bound and populate the cortical space in densities that are six times lower than neurons, while neurons span multiple layers innervating both locally and long-range areas with their axons.

I subsequently sought to investigate the organizational numbers surrounding the central player of the NGV, the astrocyte. Given that the glio-vascular interface has already been validated, I focused on the connections with neurons and neighboring astrocytes. At the neuro-glial interface, the number of neuronal somata and synapses in contact with each astrocyte was found to agree with experimental estimates. At the glial-glial interface, the number of neighbors was measured to be smaller than the reported values, a discrepancy which was caused by primary astrocytic processes penetrating the neighboring domains and establishing clusters of gap junctional connections. While this is indeed the observed behavior for P7 astrocytes, at P14 of age, a wider spread of connections was expected to occur, suggesting tree distribution within the domain needs to be revisited in the future. The NGV model renders possible the simultaneous quantification of both compositional (densities, wiring, surface areas, and volume) and organizational (connectivities, distance distributions, correlations) aspects of its entities.

Biophysical models of the blood-brain barrier interface and its metabolic signaling require precise geometry specification of the astrocytic endfoot. Therefore, the endfoot surface's algorithmic reconstruction allows for modeling the functional interface between astrocytes, pericytes, smooth muscle, and endothelial cells. The present study's algorithmic approach allows for the computational reconstruction of all endfoot surfaces in a circuit, across the entire microvasculature in the region of interest. Changes in the endfeet surface areas, which lead by extension to the vasculature coverage variation, have been observed in pathologies such as major depressive disorder (Rajkowska et al., 2013) and Huntington's disease (Hsiao et al., 2015). For example, the endfoot area's extent determines total counts of the Kir and BK potassium channels that need to be distributed for a potassium buffering model in the NGV unit (Witthoft et al., 2013). Therefore, proper distribution of abutting endfeet areas is an integral part of a blood-brain barrier's functional model. A crucial factor for the accuracy of the endfeet areas is the quality of the vascular surface mesh. Disconnected components, floating segments, and reconstruction artifacts will all

negatively influence the faithful reconstruction of the endfeet, as they will either trap the growth of an endfoot surface or force it to grow on a non-existent structure. In our model, vasculature reconstruction errors are present and influence the endfeet area distribution; however, with upcoming high-quality datasets, such error sources will be eliminated.

The NGV circuit provides the structural foundation for the large-scale biophysical modeling of cross-talk between neurons, glia, and the vasculature. This data-driven approach allows for incremental refinement as more experimental data become available, new biophysical models get published, and new questions arise. Drug delivery research studies the molecular properties of drugs. However, it should also consider the drug's interaction with its environment, i.e., the physicochemical properties as the drug travels through the blood-brain barrier to various locations of a healthy or/and pathological brain. Similarly, research in neurodegenerative diseases such as Alzheimer's disease target reactive astrocytes, the morphology of which is entirely transformed with variation in their ramification, overlap, and proliferation compared to healthy brains. Although local interactions can be studied, the large-scale emergent effects of changes in the lactate shuttle, glutamate recycling, synthesis of glutathione, and overall disruption in homeostasis can provide insights that will advance therapeutic solutions. This model will provide a factual basis for this type of work.

5.2 Future directions

5.2.1 Simulation

The digital reconstruction activity of the neuronal microcircuit Markram et al. (2015) was simulated via multi-compartmental conductance-based Hodgkin-Huxley models using the NEURON simulation tool. The extension to NGV ensembles will allow functional models that simulate the interactions between neurons, astrocytes, and the vasculature.

Existing functional models of neuro-glial, glio-vascular and glial-glial coupling are restricted to oversimplified models of no or a small number of compartments (Farr and David, 2011; Li et al., 2017; Volman et al., 2007), as a 2D single compartment networks (Bellinger, 2005; Höfer et al., 2002) or as 3D graphs (Chan et al., 2017; Lallouette et al., 2014; Wallach et al., 2014). Yet, no biophysical model of NGV interactions has been implemented in a detailed 3D network of synthesized morphologies at a micrometer resolution. Therefore, the NGV circuit provides the necessary geometric architecture to simulate such models for neuronal-glial-vascular interactions.

5.2.2 Murine and primate glial classes and sub-classes

The murine CNS is populated by three main glial classes: astrocytes, oligodendrocytes, and microglia. In this thesis, I focused on protoplasmic astrocytes due to their key and well-understood role in forming the NGV architecture, yet it is only the beginning for an entire NGV organization. New emerging studies have identified new subtypes (Batiuk et al., 2020; Clavreul et al., 2019) of protoplasmic astrocytes, the morphological characteristics of which may vary in different cortical depths and regions.

Extending the model to the white matter would require the addition of fibrous astrocytes and oligodendrocytes. Fibrous astrocytes grow straight and less branched processes (Matyash and Kettenmann, 2010), which connect to Ranvier's nodes of myelinated axons and the vasculature much alike their protoplasmic relatives (Marín-padilla, 1995). They cover larger regions (up to 300 µm) than protoplasmic astrocytes (< 60 µm) (Ransom, 2012), lack fine processes (Oberheim et al., 2009) and they are evenly distributed, although they don't form anatomically exclusive regions (Vasile et al., 2017). During neuronal development, oligodendrocytes myelinate axons to increase signal conduction velocities and form bi-directional functional units (Nave and Trapp, 2008). One oligodendrocyte attaches to multiple axonal fibers and can be depolarized by them, influencing the axonal conduction velocity in a coordinating manner (Yamazaki et al., 2010), which is not yet understood.

It has been discovered that in primates and humans, astrocytes differ not only in numbers (Bass et al., 1971), but also in topological branching and cell-type diversity. Two primate and human-specific types have been found: interlaminar and varicose projections astrocytes. The somata of interlaminar astrocytes are located in layer I and extend long processes that traverse the cortical layers parallel to each other, terminating to layers III-IV (Falcone et al., 2019). Their processes contact both capillaries and neuronal processes (Falcone et al., 2019) and have been reported to share functions with protoplasmic astrocytes (Sosunov et al., 2014), allowing them to monitor and maintain distant territories. Varicose projection astrocytes are encountered in the deep layers V-VI, where they radially extend long unbranched processes with varicose-like enlargements (Oberheim et al., 2009; Sosunov et al., 2014; Verkhratsky et al., 2018). They too exhibited electrophysiological properties similar to protoplasmic and interlaminar astrocytes (Sosunov et al., 2014).

Microglia are morphologically motile macrophages in the CNS, which continuously protrude and retract their processes, monitoring their micro-environment (Davalos et al.,

2005; Nimmerjahn et al., 2005). They make repetitive contacts with tripartite synapses, and their behavior is modulated by neuronal activity (Tremblay et al., 2010), engaging in intricate signaling patterns that also involve astrocytes (Pascual et al., 2012). Thus, the tripartite synapse has a fourth active player, which, apart from inflammatory functions, also participates in the development, maturation, regulation, and homeostasis of synapses, establishing a quad-partite synapse (Schafer et al., 2013).

The greatest challenge in adding new cell types in the NGV framework revolves around data availability and complete characterization of cell properties. Although protoplasmic astrocytes are the next most studied CNS cells to neurons, the number of highly detailed reconstructed morphologies is relatively small. However, the use of morphology synthesis reduces the need for thousands or millions of morphologies down a small number essential to capture the branching behavior of a cell type.

5.2.3 Improvements of the NGV framework

The NGV framework was designed with the use of a brain atlas in mind, in which densities, brain region annotations, the cerebral vasculature, etc., would all be registered in the same coordinate system, and a query for a specific region would extract all the data required by the framework. However, because the cerebral microvasculature was independently obtained, I manually transformed it into the neuronal coordinate space and ensured a common registration space. In the future, full automation of selecting a brain region and extracting the respective information will be possible with new microvasculature datasets that are registered in the same reference space, such as the whole brain vasculature reconstruction of Todorov et al. (2019). This is an essential step for scaling my model to the whole brain and in curved regions.

Scaling into whole-brain networks would affect the framework by increasing reading and writing times of the datasets, memory allocation, and running time for each processing step. The SONATA specification (Dai et al., 2020) and libSONATA library provide efficient out-of-core storage, which is ideal for large-scale networks. Cell placement, microdomains, and endfeet area generation would be the most affected steps of such scaling because they use the entire cortical space for their computations. Partitioning the space into chunks and running each chunk in parallel, taking care of the boundaries' computation, would resolve such a bottleneck. On the other hand, morphology synthesis would not be affected from scaling to bigger circuits because each cell is synthesized in parallel, distributed into the available CPUs of the machine. The synthesis of approximately 10000 astrocytes requires less than ten hours in 36 CPUs of one node. Therefore using

clusters with thousands of nodes would easily allow for scaling to millions of cells in the same amount of time.

A key aspect of the NGV that is currently missing from my model is the ultra-structural generation of the geometry corresponding to the perisynaptic astrocytic process that engulfs the pre and post-synaptic terminals of the synapse, forming the tripartite ensemble (Araque et al., 1999). A synthetic ultra-structural model of the tripartite synapse would combine sub-cellular functional models with large scale signal propagation throughout the NGV circuitry.

In the predictions of chapter 3, it was found that the distribution of gap junctional connections was clustered around penetrating processes in the neighboring domains. To improve the current approach, it would first require more astrocytic reconstructions to create a diverse barcode population of trees that extend at different radial distances from the soma. Then, during barcode selection in morphology synthesis, the distance from the soma to the domain boundary could be used to select a barcode that fits within that available space instead of randomly selecting one. This approach would result in improved coverage of the domain space by the grown morphology.

Finally, the NGV model is a first draft of the neuronal-glial-vascular organization, generated from sparse data across numerous studies. As data acquisition techniques improve, more and more constraints will be added in the future, incrementally improving the current model and allowing for the extension to new models that would represent different animal species or ages and simulate various CNS pathologies.

6

Supplementary Material

6.1 Vasculature site attraction field

In order to model the chemo-attractive field which influences the growth of the perivascular processes, we need first to make some assumptions of its form and properties: We assume that there isn't a preferred direction of the diffusive gradient of the chemo-attractive molecules , i.e. it's isotropic. Furthermore, given that the vasculature graph and surface mesh are not available at the time of the morphology generation , the second assumption constrains the field to be generated by a point source instead of the entire surface of the vasculature in the vicinity.

For each reconstructed astrocyte the endfeet targets were annotated as points close the the termination of an endfoot process. The closest leaf was found for each endfoot target and the upstream sections from the leaf to the root were extracted as show in Figure 6.1A.

Let a point T be the target point, S the center of the astrocytic soma. For each first point p_i of each section, the angles $theta_i$ between $\vec{SP_i}$ and ST, as a function to the radial distance to the target TP_i. However, measurements on different trees lead to different trends that depend on the extent and orientation of the tree inside the attraction field. In order to normalize the data and quantify the underlying attraction trend we performed min-max normalization for both angles and radial distances as shown in the comparison of figure 6.1B.

The attraction of the main process to the target was fit using the quantile logit function (Figure 6.1C).

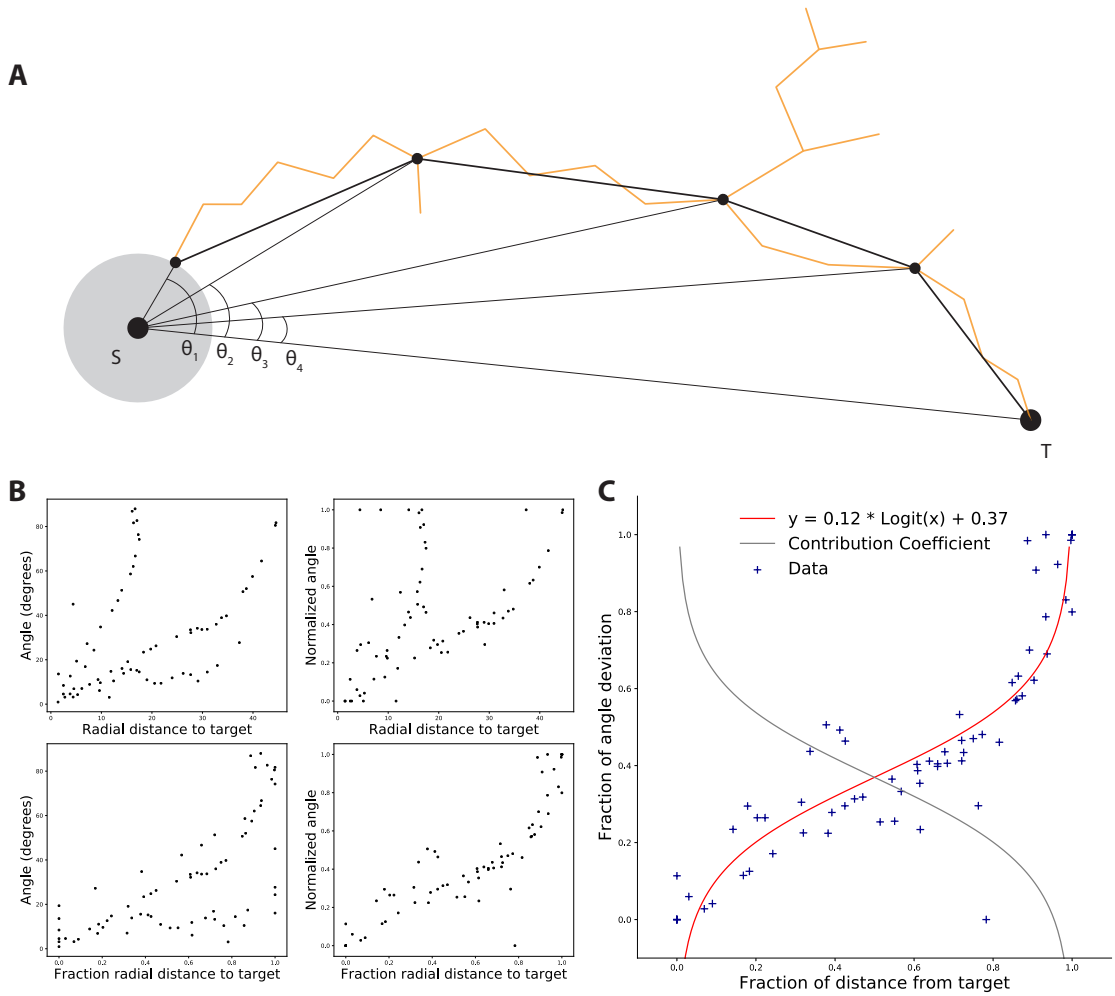

Figure 6.1 Attraction field analysis. (A) Analysis of radial distances from the soma S to each section end and the respective angle to $\vec{ST}$. (B) Scatter plots of non-normalized and min-max normalized data. (C) min-max normalized data (blue scatter) of how influenced the direction of the process is as it approaches the target along with the logit function fit (red) and the corresponding contribution coefficient α

$$y(x) = 0.12 \times L(x) + 0.37 \qquad x \in [0, 1] \tag{6.1}$$

$$L(x) = \ln\left(\frac{x}{1-x}\right) \tag{6.2}$$

The function $a(x)$ produces values in the $(-\infty, \infty)$, but we are only interested in the interval $[0, 1]$. For this reason we introduce the clamp function $c(x) = \max(0, (\min(x, 1)))$, which limits the image into the desired interval. Finally, let d_t and d_{s_i} be the distances from the soma center to the target. The contribution factor of the direction to

the target can be calculated, by substituting x with $1 - x$ and by using the identity $logit(1 - x) = -logit(x)$:

$$a\left(\frac{d_{s_i}}{d_t}\right) = c\left(y\left(1 - \frac{d_{s_i}}{d_t}\right)\right) = c\left(-0.12 \times L\left(\frac{d_{s_i}}{d_t}\right) + 0.37\right) \tag{6.3}$$

6.2 Solution to the eikonal equation

$$T_3 = T_1 + \lambda T_{1,2} + \sqrt{\left(\vec{e}_{1,3} - \lambda\vec{e}_{1,2}\right)^T Q \left(\vec{e}_{1,3} - \lambda\vec{e}_{1,2}\right)} \tag{6.4}$$

$$\vec{a} = \vec{e}_{1,3} \tag{6.5}$$

$$\vec{b} = \vec{e}_{1,2} \tag{6.6}$$

$$\tag{6.7}$$

$$\frac{\partial T_3}{\partial \lambda} = 0 \tag{6.8}$$

$$T_{1,2} + \frac{2\lambda\vec{b}^T Q\vec{b} - \vec{a}^T Q\vec{b} - \vec{b}^T Q\vec{a}}{2\sqrt{\left(\vec{a} - \lambda\vec{b}\right)^T Q \left(\vec{a} - \lambda\vec{b}\right)}} = 0 \tag{6.9}$$

$$\sqrt{\left(\vec{a} - \lambda\vec{b}\right)^T Q \left(\vec{a} - \lambda\vec{b}\right)} = \frac{\vec{a}^T Q\vec{b} + \vec{b}^T Q\vec{a} - 2\lambda\vec{b}^T Q\vec{b}}{2T_{1,2}} \tag{6.10}$$

$$\left(\vec{a} - \lambda\vec{b}\right)^T Q \left(\vec{a} - \lambda\vec{b}\right) = \left(\frac{\vec{a}^T Q\vec{b} + \vec{b}^T Q\vec{a} - 2\lambda\vec{b}^T Q\vec{b}}{2T_{1,2}}\right)^2 \tag{6.11}$$

$$\vec{n}^T Q\vec{m} = C_{nm} \tag{6.12}$$

$$C_{aa} - \lambda\left(C_{ab} + C_{ba}\right) + \lambda^2 C_{bb} = \frac{\left(C_{ab} + C_{ba} - 2\lambda C_{bb}\right)^2}{4T_{1,2}^2} \tag{6.13}$$

$$= \frac{\left(C_{ab} + C_{ba}\right)^2 - 4\lambda\left(C_{ab} + C_{ba}\right)C_{bb} + 4\lambda^2 C_{bb}^2}{4T_{1,2}^2} \tag{6.14}$$

$$= \frac{C_{ab}^2 + 2C_{ab}C_{ba} + C_{ba}^2 - 2\lambda C_{ab}C_{bb} - 2\lambda C_{ba}C_{bb} + 4\lambda^2 C_{bb}^2}{4T_{1,2}^2} \tag{6.15}$$

$$\tag{6.16}$$

$$\lambda^2 C_{bb}\left(1 - \frac{C_{bb}}{T_{1,2}^2}\right) + \lambda\left(C_{ab} + C_{ba}\right)\left(-1 + \frac{C_{bb}}{T_{1,2}^2}\right) + \left(C_{aa} - \frac{\left(C_{ab} + C_{ba}\right)^2}{4T_{1,2}^2}\right) \tag{6.17}$$

6.3 Connection of disconnected vasculature components

The vasculature dataset that is currently available from Prof. Weber's lab was extracted via synchotron based x-ray tomographic microscopy (srXTM) (Plouraboué et al., 2004) and a graph representation was generated (Reichold et al., 2009) and outputted in the vtk file format. I am developing a Python package, NeuroV, to enable the processing and analysis of such datasets.

The vasculature reconstruction consists of approximately 12000 disconnected components exponentially distributed by the number points that they contain (Figure 6.2). The aforementioned histogram does not contain the biggest component which consists of 3.8 million points (4 million total points). Due to the fact that the vasculature object consists of vertices connected by edges, it can trivially be represented via a graph G.

Let H_i be the i-th connected component (subgraph) of the graph $G = (V, E)$, where V, E are the respective vertices and edges. For each of the N connected components H_i it holds that, $V(H_i) \subset V(G)$ and $E(H_i) \subset E(G)$. Moreover, given that G is disconnected, there is no edge that connects H_i components with each other and by extension there is no shared vertex: $V(H_i) \cap V(H_j) = \varnothing$, $i \neq j$. We define a minimal edge set E' which renders G connected, i.e.:

$$E' \cup E = \{\{u, v\} : u, v \in V(G) : \forall\, k, m \in V(G)\ \exists \text{ path } p : p \text{ connects } k, m\} \tag{6.18}$$

Vasculature graph vertices are embedded in space, therefore the centroid of the 3D points that correspond to the vertices in each component was calculated. In order to reduce the computation overload due to the size of the dataset, a variable neighborhood η was defined as a sphere around the centroid of a component of radius r. It's initial value was equal to the average adjacent vertex distance and increased until a suitable vertex from another component was found. The algorithm performs an hierarchical matching of components. Specifically, starting with the set of connected components I_0 it matches each non-connected component with its closest neighbor by creating a connecting edge uv (see Figure 6.2 (b)). In the next iteration pairs of bigger components are matched from the remaining set I_1, a procedure that continues until they are all connected, i.e. $|I_n| = 1$.

$$E'_k = \{\{u, v\} : u \in V(H_i),\ v \in V(H_j),\ i \neq j : min||u, v||\} \qquad H_i, H_j \in I_k \tag{6.19}$$

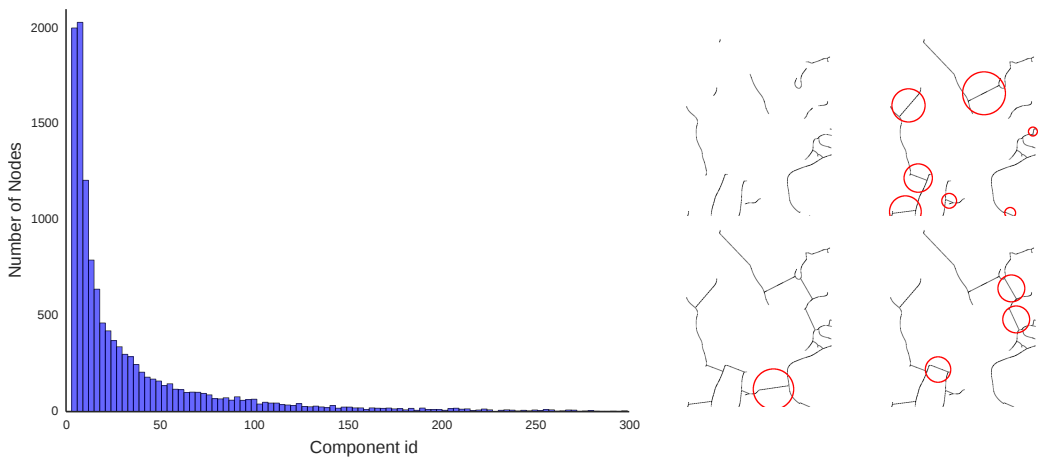

(a) (b)

Figure 6.2 (a) Histogram of the number of the disconnected components and their respective number of nodes that they contain. (b) Example of the iterative connection (clockwise from upper left corner) of a graph test sample.

The end result was a connected undirected graph that allowed the parsing of the vasculature as a whole. Parsing of the vasculature is essential for the extraction of morphological features, such as path distances from a start point, and especially for

finding and labeling the closest neighbor segment to a point in space. For example, the calculation of the best candidate segments for endfoot targeting requires the detection of the closest neighboring point followed by the parsing of the graph in order to determine the best position of the endfeet.

6.4 Calculation of Empty and Overlap Space

The domain geometry of the astrocytic morphologies was approximated by calculating the convex hulls of the points that constitute each morphology. The overlap volume is defined as the intersection volume of the convex hulls and the empty space as the union volume subtracted from the volume of the circuit.

$$V_{\text{overlap}} = \bigcap_n V^n_{\text{hull}} \qquad V_{\text{empty}} = V_{\text{circuit}} - \bigcup_n V^n_{\text{hull}}$$

Given a rectangular box of known volume V_{box} that includes all the convex hulls, a sample of N uniformly random 3D points were generated. The number of points that lie inside an intersection C_{int} and inside the convex hulls in general C_{hull} were counted. The aforementioned values can be trivially calculated with the following analogical relations:

$$\frac{V_{\text{overlap}}}{V_{\text{box}}} = \frac{C_{int}}{N} \qquad \frac{V_{\text{hull}}}{V_{\text{box}}} = \frac{C_{hull}}{N}$$

Bibliography

N. Joan Abbott, Lars Rönnbäck, and Elisabeth Hansson. Astrocyte–endothelial interactions at the blood–brain barrier. *Nature Reviews Neuroscience*, 7(1):41–53, January 2006. ISSN 1471-003X. doi: 10.1038/nrn1824. URL http://www.nature.com/nrn/journal/v7/n1/abs/nrn1824.html.

N. Joan Abbott, Adjanie A. K. Patabendige, Diana E. M. Dolman, Siti R. Yusof, and David J. Begley. Structure and function of the blood–brain barrier. *Neurobiology of Disease*, 37(1):13–25, January 2010. ISSN 0969-9961. doi: 10.1016/j.nbd.2009.07.030. URL http://www.sciencedirect.com/science/article/pii/S0969996109002083.

Marwan Abdellah, Nadir Román Guerrero, Samuel Lapere, Jay S. Coggan, Daniel Keller, Benoit Coste, Snigdha Dagar, Jean-Denis Courcol, Henry Markram, and Felix Schürmann. Interactive visualization and analysis of morphological skeletons of brain vasculature networks with VessMorphoVis. *Bioinformatics*, 36(Supplement_1):i534–i541, July 2020. ISSN 1367-4803. doi: 10.1093/bioinformatics/btaa461. URL https://academic.oup.com/bioinformatics/article/36/Supplement_1/i534/5870503. Publisher: Oxford Academic.

Nicola J Allen and Ben A Barres. Signaling between glia and neurons: focus on synaptic plasticity. *Current opinion in neurobiology*, 15(5):542–548, 2005. ISSN 0959-4388. Publisher: Elsevier.

Thierry Amédée, Antoine Robert, and Jonathan A Coles. Potassium homeostasis and glial energy metabolism. *Glia*, 21(1):46–55, 1997. ISSN 0894-1491. Publisher: Wiley Online Library.

W Lloyd Andriezen. The neuroglia elements in the human brain. *British medical journal*, 2(1700):227, 1893. Publisher: BMJ Publishing Group.

Florence Appaix, Sabine Girod, Sylvie Boisseau, Johannes Römer, Jean-Claude Vial, Mireille Albrieux, Mathieu Maurin, Antoine Depaulis, Isabelle Guillemain, and Boudewijn van der Sanden. Specific In Vivo Staining of Astrocytes in the Whole Brain after Intravenous Injection of Sulforhodamine Dyes. *PLOS ONE*, 7(4): e35169, April 2012. ISSN 1932-6203. doi: 10.1371/journal.pone.0035169. URL https://journals.plos.org/plosone/article?id=10.1371/journal.pone.0035169.

Alfonso Araque, Vladimir Parpura, Rita P Sanzgiri, and Philip G Haydon. Tripartite synapses: glia, the unacknowledged partner. *Trends in neurosciences*, 22(5):208–215, 1999. ISSN 0166-2236. Publisher: Elsevier.

Alfonso Araque, Giorgio Carmignoto, Philip G. Haydon, Stéphane H. R. Oliet, Richard Robitaille, and Andrea Volterra. Gliotransmitters Travel in Time and Space. *Neuron*, 81 (4):728–739, February 2014. ISSN 0896-6273. doi: 10.1016/j.neuron.2014.02.007. URL https://www.cell.com/neuron/abstract/S0896-6273(14)00105-6. Publisher: Elsevier.

Giorgio A Ascoli and Jeffrey L Krichmar. L-neuron: A modeling tool for the efficient generation and parsimonious description of dendritic morphology. *Neurocomputing*, 32–33:1003–1011, June 2000. ISSN 0925-2312. doi: 10.1016/S0925-2312(00)00272-1. URL http://www.sciencedirect.com/science/article/pii/S0925231200002721.

Giorgio A Ascoli, Jeffrey L Krichmar, Ruggero Scorcioni, Slawomir J Nasuto, Stephen L Senft, and GL Krichmar. Computer generation and quantitative morphometric analysis of virtual neurons. *Anatomy and Embryology*, 204(4):283–301, 2001. ISSN 0340-2061. Publisher: Springer.

Giorgio A. Ascoli, Duncan E. Donohue, and Maryam Halavi. NeuroMorpho.Org: A Central Resource for Neuronal Morphologies. *Journal of Neuroscience*, 27(35):9247–9251, August 2007. ISSN 0270-6474, 1529-2401. doi: 10.1523/JNEUROSCI.2055-07.2007. URL https://www.jneurosci.org/content/27/35/9247. Publisher: Society for Neuroscience Section: Toolbox.

Giorgio A. Ascoli, Lidia Alonso-Nanclares, Stewart A. Anderson, German Barrionuevo, Ruth Benavides-Piccione, Andreas Burkhalter, György Buzsáki, Bruno Cauli, Javier DeFelipe, Alfonso Fairén, Dirk Feldmeyer, Gord Fishell, Yves Fregnac, Tamas F. Freund, Daniel Gardner, Esther P. Gardner, Jesse H. Goldberg, Moritz Helmstaedter, Shaul Hestrin, Fuyuki Karube, Zoltán F. Kisvárday, Bertrand Lambolez, David A. Lewis, Oscar Marin, Henry Markram, Alberto Muñoz, Adam Packer, Carl C. H. Petersen, Kathleen S. Rockland, Jean Rossier, Bernardo Rudy, Peter Somogyi, Jochen F. Staiger,

Gabor Tamas, Alex M. Thomson, Maria Toledo-Rodriguez, Yun Wang, David C. West, Rafael Yuste, and The Petilla Interneuron Nomenclature Group (PING). Petilla terminology: nomenclature of features of GABAergic interneurons of the cerebral cortex. *Nature Reviews Neuroscience*, 9(7):557–568, July 2008. ISSN 1471-0048. doi: 10.1038/nrn2402. URL https://www.nature.com/articles/nrn2402. Number: 7 Publisher: Nature Publishing Group.

Franz Aurenhammer. Power diagrams: properties, algorithms and applications. *SIAM Journal on Computing*, 16(1):78–96, 1987. ISSN 0097-5397. Publisher: SIAM.

Maryam Bagheri, Arjang Rezakhani, Sofie Nyström, Maria V Turkina, Mehrdad Roghani, Per Hammarström, and Simin Mohseni. Amyloid beta 1-40-induced astrogliosis and the effect of genistein treatment in rat: a three-dimensional confocal morphometric and proteomic study. *PLoS One*, 8(10):e76526, 2013. ISSN 1932-6203. Publisher: Public Library of Science.

Norman H. Bass, Helen H. Hess, Alfred Pope, and Caroline Thalheimer. Quantitative cytoarchitectonic distribution of neurons, glia, and DNA in rat cerebral cortex. *The Journal of Comparative Neurology*, 143(4):481–490, December 1971. ISSN 1096-9861. doi: 10.1002/cne.901430405. URL http://onlinelibrary.wiley.com/doi/10.1002/cne.901430405/abstract.

Mykhailo Y. Batiuk, Araks Martirosyan, Jérôme Wahis, Filip de Vin, Catherine Marneffe, Carola Kusserow, Jordan Koeppen, João Filipe Viana, João Filipe Oliveira, Thierry Voet, Chris P. Ponting, T. Grant Belgard, and Matthew G. Holt. Identification of region-specific astrocyte subtypes at single cell resolution. *Nature Communications*, 11(1):1220, March 2020. ISSN 2041-1723. doi: 10.1038/s41467-019-14198-8. URL https://www.nature.com/articles/s41467-019-14198-8. Number: 1 Publisher: Nature Publishing Group.

Anja Beckmann, Alexander Grißmer, Sandra Wolf, Johanna Recktenwald, and Carola Meier. Oxygen-glucose deprivation in mouse astrocytes is associated with ultrastructural changes in connexin 43 gap junctions. *Neuroscience*, 397:67–79, 2019. ISSN 0306-4522. Publisher: Elsevier.

Norbert Beckmann, Hans-Peter Kriegel, Ralf Schneider, and Bernhard Seeger. The R*-tree: an efficient and robust access method for points and rectangles. In *Proceedings of the 1990 ACM SIGMOD international conference on Management of data*, SIGMOD '90, pages 322–331, New York, NY, USA, May 1990. Association for Computing

Machinery. ISBN 978-0-89791-365-2. doi: 10.1145/93597.98741. URL https://doi.org/10.1145/93597.98741.

Steve Bellinger. Modeling calcium wave oscillations in astrocytes. *Neurocomputing*, 65: 843–850, 2005. ISSN 0925-2312. Publisher: Elsevier.

Alba Bellot-Saez, Orsolya Kékesi, John W Morley, and Yossi Buskila. Astrocytic modulation of neuronal excitability through K+ spatial buffering. *Neuroscience & Biobehavioral Reviews*, 77:87–97, 2017. ISSN 0149-7634. Publisher: Elsevier.

LH Bergersen, C Morland, L Ormel, JE Rinholm, Max Larsson, JFH Wold, ÅT Røe, A Stranna, M Santello, and D Bouvier. Immunogold detection of L-glutamate and D-serine in small synaptic-like microvesicles in adult hippocampal astrocytes. *Cerebral cortex*, 22(7):1690–1697, 2012. ISSN 1460-2199. Publisher: Oxford University Press.

Paola Bezzi, Giorgio Carmignoto, Lucia Pasti, Sabino Vesce, Daniela Rossi, Barbara Lodi Rizzini, Tullio Pozzan, and Andrea Volterra. Prostaglandins stimulate calcium-dependent glutamate release in astrocytes. *Nature*, 391(6664):281–285, 1998. ISSN 1476-4687. Publisher: Nature Publishing Group.

Paola Bezzi, Vidar Gundersen, José Luis Galbete, Gerald Seifert, Christian Steinhäuser, Ethel Pilati, and Andrea Volterra. Astrocytes contain a vesicular compartment that is competent for regulated exocytosis of glutamate. *Nature neuroscience*, 7(6):613–620, 2004. ISSN 1546-1726. Publisher: Nature Publishing Group.

Erika Bindocci, Iaroslav Savtchouk, Nicolas Liaudet, Denise Becker, Giovanni Carriero, and Andrea Volterra. Three-dimensional Ca2+ imaging advances understanding of astrocyte biology. *Science*, 356(6339), 2017. ISSN 0036-8075. Publisher: American Association for the Advancement of Science.

S Blinkow and I Glezer. The neuroglia. *The Human Brain in Figures and Tables*, pages 237–253, 1968. Publisher: Plenum Press.

Gilles Bonvento, Nicola Sibson, and Luc Pellerin. Does glutamate image your thoughts? *Trends in neurosciences*, 25(7):359–364, 2002. ISSN 0166-2236. Publisher: Elsevier.

Panagiotis Bozelos, Stefanos S. Stefanou, Georgios Bouloukakis, Constantinos Melachrinos, and Panayiota Poirazi. REMOD: A Tool for Analyzing and Remodeling the Dendritic Architecture of Neural Cells. *Frontiers in Neuroanatomy*, 9, 2016. ISSN 1662-5129. doi: 10.3389/fnana.2015.00156. URL https://www.frontiersin.org/articles/10.3389/fnana.2015.00156/full. Publisher: Frontiers.

Heiko Braak and Eva Braak. Diagnostic criteria for neuropathologic assessment of Alzheimer's disease. *Neurobiology of aging*, 18(4):S85–S88, 1997. ISSN 0197-4580. Publisher: Elsevier.

Angus M Brown. Brain glycogen re-awakened. *Journal of neurochemistry*, 89(3):537–552, 2004. ISSN 0022-3042. Publisher: Wiley Online Library.

Angus M Brown and Bruce R Ransom. Astrocyte glycogen as an emergency fuel under conditions of glucose deprivation or intense neural activity. *Metabolic brain disease*, 30 (1):233–239, 2015. ISSN 0885-7490. Publisher: Springer.

Julian ML Budd, Krisztina Kovács, Alex S Ferecskó, Péter Buzás, Ulf T Eysel, and Zoltán F Kisvárday. Neocortical axon arbors trade-off material and conduction delay conservation. *PLoS Comput Biol*, 6(3):e1000711, 2010. ISSN 1553-7358. Publisher: Public Library of Science.

RE Burke, WB Marks, and B Ulfhake. A parsimonious description of motoneuron dendritic morphology using computer simulation. *Journal of Neuroscience*, 12(6): 2403–2416, 1992. ISSN 0270-6474. Publisher: Soc Neuroscience.

Eric A. Bushong, Maryann E. Martone, Ying Z. Jones, and Mark H. Ellisman. Protoplasmic Astrocytes in CA1 Stratum Radiatum Occupy Separate Anatomical Domains. *The Journal of Neuroscience*, 22(1):183–192, January 2002. ISSN 0270-6474, 1529-2401. URL http://www.jneurosci.org/content/22/1/183.

Eric A Bushong, Maryann E Martone, and Mark H Ellisman. Maturation of astrocyte morphology and the establishment of astrocyte domains during postnatal hippocampal development. *International Journal of Developmental Neuroscience*, 22(2):73–86, April 2004. ISSN 0736-5748. doi: 10.1016/j.ijdevneu.2003.12.008. URL http://www.sciencedirect.com/science/article/pii/S0736574803001473.

Corrado Calì, Marco Agus, Kalpana Kare, Daniya J. Boges, Heikki Lehväslaiho, Markus Hadwiger, and Pierre J. Magistretti. 3D cellular reconstruction of cortical glia and parenchymal morphometric analysis from Serial Block-Face Electron Microscopy of juvenile rat. *Progress in Neurobiology*, 183:101696, December 2019. ISSN 0301-0082. doi: 10.1016/j.pneurobio.2019.101696. URL http://www.sciencedirect.com/science/article/pii/S0301008219300139.

Siow-Cheng Chan, Siew-Ying Mok, Danny Wee-Kiat Ng, and Sing-Yau Goh. The role of neuron–glia interactions in the emergence of ultra-slow oscillations. *Biological cybernetics*, 111(5-6):459–472, 2017. ISSN 0340-1200. Publisher: Springer.

T. Chang Ling and J. Stone. Factors determining the morphology and distribution of astrocytes in the cat retina: a 'contact-spacing' model of astrocyte interaction. *The Journal of Comparative Neurology*, 303(3):387–399, January 1991. ISSN 0021-9967. doi: 10.1002/cne.903030305.

Solène Clavreul, Lamiae Abdeladim, Edwin Hernández-Garzón, Dragos Niculescu, Jason Durand, Sio-Hoï Ieng, Raphaëlle Barry, Gilles Bonvento, Emmanuel Beaurepaire, Jean Livet, and Karine Loulier. Cortical astrocytes develop in a plastic manner at both clonal and cellular levels. *Nature Communications*, 10(1):1–14, October 2019. ISSN 2041-1723. doi: 10.1038/s41467-019-12791-5. URL https://www.nature.com/articles/s41467-019-12791-5.

Jay S. Coggan, Corrado Calì, Daniel Keller, Marco Agus, Daniya Boges, Marwan Abdellah, Kalpana Kare, Heikki Lehväslaiho, Stefan Eilemann, Renaud Blaise Jolivet, Markus Hadwiger, Henry Markram, Felix Schürmann, and Pierre J. Magistretti. A Process for Digitizing and Simulating Biologically Realistic Oligocellular Networks Demonstrated for the Neuro-Glio-Vascular Ensemble. *Frontiers in Neuroscience*, 12, 2018. ISSN 1662-453X. doi: 10.3389/fnins.2018.00664. URL https://www.frontiersin.org/articles/10.3389/fnins.2018.00664/full. Publisher: Frontiers.

Ann H Cornell-Bell, Steven M Finkbeiner, Mark S Cooper, and Stephen J Smith. Glutamate induces calcium waves in cultured astrocytes: long-range glial signaling. *Science*, 247(4941):470–473, 1990. ISSN 0036-8075. Publisher: American Association for the Advancement of Science.

Hermann Cuntz, Alexander Borst, and Idan Segev. Optimization principles of dendritic structure. *Theoretical Biology and Medical Modelling*, 4(1):21, June 2007. ISSN 1742-4682. doi: 10.1186/1742-4682-4-21. URL https://doi.org/10.1186/1742-4682-4-21.

Hermann Cuntz, Friedrich Forstner, Alexander Borst, and Michael Häusser. One Rule to Grow Them All: A General Theory of Neuronal Branching and Its Practical Application. *PLoS Computational Biology*, 6(8), August 2010. ISSN 1553-734X. doi: 10.1371/journal.pcbi.1000877. URL http://www.ncbi.nlm.nih.gov/pmc/articles/PMC2916857/.

Kael Dai, Juan Hernando, Yazan N. Billeh, Sergey L. Gratiy, Judit Planas, Andrew P. Davison, Salvador Dura-Bernal, Padraig Gleeson, Adrien Devresse, Benjamin K. Dichter, Michael Gevaert, James G. King, Werner A. H. Van Geit, Arseny V. Povolotsky, Eilif Muller, Jean-Denis Courcol, and Anton Arkhipov. The SONATA data format for efficient description of large-scale network models. *PLOS Computational Biology*,

16(2):e1007696, February 2020. ISSN 1553-7358. doi: 10.1371/journal.pcbi.1007696. URL https://journals.plos.org/ploscompbiol/article?id=10.1371/journal.pcbi.1007696. Publisher: Public Library of Science.

Jessica S. Damoiseaux and Michael D. Greicius. Greater than the sum of its parts: a review of studies combining structural connectivity and resting-state functional connectivity. *Brain Structure and Function*, 213(6):525–533, June 2009. ISSN 1863-2653, 1863-2661. doi: 10.1007/s00429-009-0208-6. URL http://link.springer.com/article/10.1007/s00429-009-0208-6.

Dimitrios Davalos, Jaime Grutzendler, Guang Yang, Jiyun V Kim, Yi Zuo, Steffen Jung, Dan R Littman, Michael L Dustin, and Wen-Biao Gan. ATP mediates rapid microglial response to local brain injury in vivo. *Nature neuroscience*, 8(6):752–758, 2005. ISSN 1546-1726. Publisher: Nature Publishing Group.

David Dereudre. Introduction to the theory of Gibbs point processes. In *Stochastic Geometry*, pages 181–229. Springer, 2019.

Barbara Di Benedetto, Victoria A. Malik, Salina Begum, Lena Jablonowski, Gabriela B. Gómez-González, Inga D. Neumann, and Rainer Rupprecht. Fluoxetine Requires the Endfeet Protein Aquaporin-4 to Enhance Plasticity of Astrocyte Processes. *Frontiers in Cellular Neuroscience*, 10, 2016. ISSN 1662-5102. doi: 10.3389/fncel.2016.00008. URL https://www.frontiersin.org/articles/10.3389/fncel.2016.00008/full.

Gerald A Dienel and Douglas L Rothman. Reevaluation of Astrocyte-Neuron Energy Metabolism with Astrocyte Volume Fraction Correction: Impact on Cellular Glucose Oxidation Rates, Glutamate–Glutamine Cycle Energetics, Glycogen Levels and Utilization Rates vs. Exercising Muscle, and Na+/K+ Pumping Rates. *Neurochemical Research*, pages 1–24, 2020. ISSN 1573-6903. Publisher: Springer.

Claudia Distler, Zofia Dreher, and Jonathan Stone. Contact spacing among astrocytes in the central nervous system: An hypothesis of their structural role. *Glia*, 4(5):484–494, 1991. ISSN 1098-1136. doi: 10.1002/glia.440040508. URL https://onlinelibrary.wiley.com/doi/abs/10.1002/glia.440040508. _eprint: https://onlinelibrary.wiley.com/doi/pdf/10.1002/glia.440040508.

Philip M Dixon. R ipley's K Function. *Wiley StatsRef: Statistics Reference Online*, 2014. Publisher: Wiley Online Library.

Adam Dobrin. A review of properties and variations of Voronoi diagrams. *Whitman College*, pages 1949–3053, 2005. Publisher: Citeseer.

Duncan E. Donohue and Giorgio A. Ascoli. Automated reconstruction of neuronal morphology: An overview. *Brain Research Reviews*, 67(1):94–102, June 2011. ISSN 0165-0173. doi: 10.1016/j.brainresrev.2010.11.003. URL http://www.sciencedirect.com/science/article/pii/S0165017310001293.

Qiang Du, Vance Faber, and Max Gunzburger. Centroidal Voronoi tessellations: Applications and algorithms. *SIAM review*, 41(4):637–676, 1999. ISSN 0036-1445. Publisher: SIAM.

Jens P Eberhard, Alexander Wanner, and Gabriel Wittum. NeuGen: a tool for the generation of realistic morphology of cortical neurons and neural networks in 3D. *Neurocomputing*, 70(1-3):327–342, 2006. ISSN 0925-2312. Publisher: Elsevier.

Michael N Economo, Nathan G Clack, Luke D Lavis, Charles R Gerfen, Karel Svoboda, Eugene W Myers, and Jayaram Chandrashekar. A platform for brain-wide imaging and reconstruction of individual neurons. *eLife*, 5:e10566, January 2016. ISSN 2050-084X. doi: 10.7554/eLife.10566. URL https://doi.org/10.7554/eLife.10566. Publisher: eLife Sciences Publications, Ltd.

Robert Egger, Vincent J. Dercksen, Daniel Udvary, Hans-Christian Hege, and Marcel Oberlaender. Generation of dense statistical connectomes from sparse morphological data. *Frontiers in Neuroanatomy*, 8, 2014. ISSN 1662-5129. doi: 10.3389/fnana.2014.00129. URL https://www.frontiersin.org/articles/10.3389/fnana.2014.00129/full. Publisher: Frontiers.

Jason G Emsley and Jeffrey D Macklis. Astroglial heterogeneity closely reflects the neuronal-defined anatomy of the adult murine CNS. *Neuron glia biology*, 2(3):175, 2006. Publisher: NIH Public Access.

Csaba Erö, Marc-Oliver Gewaltig, Daniel Keller, and Henry Markram. A Cell Atlas for the Mouse Brain. *Frontiers in Neuroinformatics*, 12, 2018. ISSN 1662-5196. doi: 10.3389/fninf.2018.00084. URL https://www.frontiersin.org/articles/10.3389/fninf.2018.00084/full#F2.

Carmen Estrada, James V Bready, Judith A Berliner, William M Pardridge, and Pasquale A Cancilla. Astrocyte growth stimulation by a soluble factor produced by cerebral endothelial cells in vitro. *Journal of Neuropathology & Experimental*

Neurology, 49(6):539–549, 1990. ISSN 1554-6578. Publisher: American Association of Neuropathologists, Inc.

Carmen Falcone, Marisol Wolf-Ochoa, Sarwat Amina, Tiffany Hong, Gelareh Vakilzadeh, William D Hopkins, Patrick R Hof, Chet C Sherwood, Paul R Manger, and Stephen C Noctor. Cortical interlaminar astrocytes across the therian mammal radiation. *Journal of Comparative Neurology*, 527(10):1654–1674, 2019. ISSN 0021-9967. Publisher: Wiley Online Library.

Akhlaq A Farooqui, Hsiu-Chiung Yang, Thad A Rosenberger, and Lloyd A Horrocks. Phospholipase A2 and its role in brain tissue. *Journal of neurochemistry*, 69(3):889–901, 1997. ISSN 0022-3042. Publisher: Wiley Online Library.

Hannah Farr and Tim David. Models of neurovascular coupling via potassium and EET signalling. *Journal of theoretical biology*, 286:13–23, 2011. ISSN 0022-5193. Publisher: Elsevier.

Zhisong Fu, Won-Ki Jeong, Yongsheng Pan, Robert M Kirby, and Ross T Whitaker. A fast iterative method for solving the eikonal equation on triangulated surfaces. *SIAM Journal on Scientific Computing*, 33(5):2468–2488, 2011. ISSN 1064-8275. Publisher: SIAM.

Woo-Ping Ge, Atsushi Miyawaki, Fred H. Gage, Yuh Nung Jan, and Lily Yeh Jan. Local generation of glia is a major astrocyte source in postnatal cortex. *Nature*, 484(7394): 376–380, March 2012. ISSN 1476-4687. doi: 10.1038/nature10959.

James E. Goldman and Fung-Chow Chiu. Growth Kinetics, Cell Shape, and the Cytoskeleton of Primary Astrocyte Cultures. *Journal of Neurochemistry*, 42(1): 175–184, 1984. ISSN 1471-4159. doi: 10.1111/j.1471-4159.1984.tb09714.x. URL https://onlinelibrary.wiley.com/doi/abs/10.1111/j.1471-4159.1984.tb09714.x. _eprint: https://onlinelibrary.wiley.com/doi/pdf/10.1111/j.1471-4159.1984.tb09714.x.

Vera A Golovina and Mordecai P Blaustein. Unloading and refilling of two classes of spatially resolved endoplasmic reticulum Ca2+ stores in astrocytes. *Glia*, 31(1):15–28, 2000. ISSN 0894-1491. Publisher: Wiley Online Library.

Grant R. J. Gordon, Sean J. Mulligan, and Brian A. MacVicar. Astrocyte control of the cerebrovasculature. *Glia*, 55(12):1214–1221, 2007. ISSN 1098-1136. doi: 10.1002/glia.20543. URL https://onlinelibrary.wiley.com/doi/abs/10.1002/glia.20543. _eprint: https://onlinelibrary.wiley.com/doi/pdf/10.1002/glia.20543.

Daniel J Gould, Tegy J Vadakkan, Ross A Poché, and Mary E Dickinson. Multifractal and lacunarity analysis of microvascular morphology and remodeling. *Microcirculation*, 18(2):136–151, 2011. ISSN 1073-9688. Publisher: Wiley Online Library.

P. Gressens, C. Richelme, H. J. Kadhim, J. F. Gadisseux, and P. Evrard. The germinative zone produces the most cortical astrocytes after neuronal migration in the developing mammalian brain. *Biology of the Neonate*, 61(1):4–24, 1992. ISSN 0006-3126. doi: 10.1159/000243526.

Antje Grosche, Jens Grosche, Mark Tackenberg, Dorit Scheller, Gwendolyn Gerstner, Annett Gumprecht, Thomas Pannicke, Petra G Hirrlinger, Ulrika Wilhelmsson, and Kerstin Hüttmann. Versatile and simple approach to determine astrocyte territories in mouse neocortex and hippocampus. *PLoS One*, 8(7):e69143, 2013. ISSN 1932-6203. Publisher: Public Library of Science.

Wesley B Grueber and Alvaro Sagasti. Self-avoidance and tiling: mechanisms of dendrite and axon spacing. *Cold Spring Harbor perspectives in biology*, 2(9):a001750, 2010. ISSN 1943-0264. Publisher: Cold Spring Harbor Lab.

Michael M. Halassa, Tommaso Fellin, and Philip G. Haydon. The tripartite synapse: roles for gliotransmission in health and disease. *Trends in Molecular Medicine*, 13(2): 54–63, February 2007a. ISSN 1471-4914. doi: 10.1016/j.molmed.2006.12.005. URL http://www.sciencedirect.com/science/article/pii/S1471491406002851.

Michael M Halassa, Tommaso Fellin, Hajime Takano, Jing-Hui Dong, and Philip G Haydon. Synaptic islands defined by the territory of a single astrocyte. *Journal of Neuroscience*, 27(24):6473–6477, 2007b. ISSN 0270-6474. Publisher: Soc Neuroscience.

Maryam Halavi, Kelly A. Hamilton, Ruchi Parekh, and Giorgio A. Ascoli. Digital Reconstructions of Neuronal Morphology: Three Decades of Research Trends. *Frontiers in Neuroscience*, 6, April 2012. ISSN 1662-4548. doi: 10.3389/fnins.2012.00049. URL https://www.ncbi.nlm.nih.gov/pmc/articles/PMC3332236/.

Andrew P Halestrap and Nigel T PRICE. The proton-linked monocarboxylate transporter (MCT) family: structure, function and regulation. *Biochemical Journal*, 343(2):281–299, 1999. ISSN 0264-6021. Publisher: Portland Press Ltd.

Nicola B. Hamilton and David Attwell. Do astrocytes really exocytose neurotransmitters? *Nature Reviews Neuroscience*, 11(4):227–238, April 2010. ISSN 1471-0048. doi: 10.

1038/nrn2803. URL https://www.nature.com/articles/nrn2803. Number: 4 Publisher: Nature Publishing Group.

P Hamilton. A language to describe the growth of neurites. *Biological cybernetics*, 68(6): 559–565, 1993. ISSN 0340-1200. Publisher: Springer.

Masamitsu Hara, Kazu Kobayakawa, Yasuyuki Ohkawa, Hiromi Kumamaru, Kazuya Yokota, Takeyuki Saito, Ken Kijima, Shingo Yoshizaki, Katsumi Harimaya, Yasuharu Nakashima, and Seiji Okada. Interaction of reactive astrocytes with type I collagen induces astrocytic scar formation through the integrin–N-cadherin pathway after spinal cord injury. *Nature Medicine*, 23(7):818–828, July 2017. ISSN 1546-170X. doi: 10.1038/nm.4354. URL https://www.nature.com/articles/nm.4354. Number: 7 Publisher: Nature Publishing Group.

Herbert Haug. Brain sizes, surfaces, and neuronal sizes of the cortex cerebri: A stereological investigation of man and his variability and a comparison with some mammals (primates, whales, marsupials, insectivores, and one elephant). *American Journal of Anatomy*, 180(2):126–142, 1987. ISSN 1553-0795. doi: 10.1002/aja.1001800203. URL https://onlinelibrary.wiley.com/doi/abs/10.1002/aja.1001800203. _eprint: https://onlinelibrary.wiley.com/doi/pdf/10.1002/aja.1001800203.

Stefan Heinzer, Thomas Krucker, Marco Stampanoni, Rafael Abela, Eric P Meyer, Alexandra Schuler, Philipp Schneider, and Ralph Müller. Hierarchical microimaging for multiscale analysis of large vascular networks. *Neuroimage*, 32(2):626–636, 2006. ISSN 1053-8119. Publisher: Elsevier.

Stefan Heinzer, Gisela Kuhn, Thomas Krucker, Eric Meyer, Alexandra Ulmann-Schuler, Marco Stampanoni, Max Gassmann, Hugo H Marti, Ralph Müller, and Johannes Vogel. Novel three-dimensional analysis tool for vascular trees indicates complete micro-networks, not single capillaries, as the angiogenic endpoint in mice overexpressing human VEGF165 in the brain. *Neuroimage*, 39(4):1549–1558, 2008. ISSN 1053-8119. Publisher: Elsevier.

Fritz A Henn, Hengo Haljama, and Anders Hamberger. Glial cell function: active control of extracellular K+ concentration. *Brain Research*, 43(2):437–443, 1972. ISSN 0006-8993. Publisher: Elsevier.

Suzana Herculano-Houzel. The glia/neuron ratio: How it varies uniformly across brain structures and species and what that means for brain physiology and

evolution. *Glia*, 62(9):1377–1391, 2014. ISSN 1098-1136. doi: 10.1002/glia.22683. URL https://onlinelibrary.wiley.com/doi/abs/10.1002/glia.22683. _eprint: https://onlinelibrary.wiley.com/doi/pdf/10.1002/glia.22683.

Leonardo A. Hernández-Pérez, Duniel Delgado-Castillo, Rainer Martín-Pérez, Rubén Orozco-Morales, and Juan V. Lorenzo-Ginori. New Features for Neuron Classification. *Neuroinformatics*, 17(1):5–25, January 2019. ISSN 1559-0089. doi: 10.1007/s12021-018-9374-0. URL https://doi.org/10.1007/s12021-018-9374-0.

Leif Hertz. Possible role of neuroglia: a potassium-mediated neuronal–neuroglial–neuronal impulse transmission system. *Nature*, 206(4989):1091–1094, 1965. ISSN 0028-0836. Publisher: Springer.

DE Hillman. Neuronal shape parameters and substructures as a basis of neuronal form. *The neurosciences, fourth study program*, pages 477–498, 1979. Publisher: MIT Press Cambridge, MA.

Hodgkin A. L. and Huxley A. F. A quantitative description of membrane current and its application to conduction and excitation in nerve. *The Journal of Physiology*, 117(4): 500–544, August 1952. ISSN 0022-3751. doi: 10.1113/jphysiol.1952.sp004764. URL https://physoc.onlinelibrary.wiley.com/doi/abs/10.1113/jphysiol.1952.sp004764.

Glendon Holst, Stuart Berg, Kalpana Kare, Pierre Magistretti, and Corrado Cali. Adding large EM stack support. pages 1–7. IEEE, 2016. ISBN 1-4673-8956-0.

Han-Yun Hsiao, Yu-Chen Chen, Chien-Hsiang Huang, Chiao-Chi Chen, Yi-Hua Hsu, Hui-Mei Chen, Feng-Lan Chiu, Hung-Chih Kuo, Chen Chang, and Yijuang Chern. Aberrant astrocytes impair vascular reactivity in Huntington disease. *Annals of Neurology*, 78 (2):178–192, August 2015. ISSN 1531-8249. doi: 10.1002/ana.24428.

Matthew R Hynd, Heather L Scott, and Peter R Dodd. Glutamate-mediated excitotoxicity and neurodegeneration in Alzheimer's disease. *Neurochemistry international*, 45(5): 583–595, 2004. ISSN 0197-0186. Publisher: Elsevier.

Thomas Höfer, Laurent Venance, and Christian Giaume. Control and plasticity of intercellular calcium waves in astrocytes: a modeling approach. *Journal of Neuroscience*, 22(12):4850–4859, 2002. ISSN 0270-6474. Publisher: Soc Neuroscience.

JOHN D Imig, Ai Ping Zou, Dave E Stec, DAVID R Harder, JOHN R Falck, and Richard J Roman. Formation and actions of 20-hydroxyeicosatetraenoic acid in rat renal arterioles.

American Journal of Physiology-Regulatory, Integrative and Comparative Physiology, 270(1):R217–R227, 1996. ISSN 0363-6119.

Yuh-Nung Jan and Lily Yeh Jan. Branching out: mechanisms of dendritic arborization. *Nature Reviews Neuroscience*, 11(5):316–328, 2010. ISSN 1471-0048. Publisher: Nature Publishing Group.

Jernej Jorgačevski, Maja Potokar, Marko Kreft, Alenka Guček, Jean-Pierre Mothet, and Robert Zorec. Astrocytic Vesicle-based Exocytosis in Cultures and Acutely Isolated Hippocampal Rodent Slices. *Journal of Neuroscience Research*, 95(11):2152–2158, 2017. ISSN 0360-4012. Publisher: Wiley Online Library.

Kamel Kacem, Pierre Lacombe, Jacques Seylaz, and Gilles Bonvento. Structural organization of the perivascular astrocyte endfeet and their relationship with the endothelial glucose transporter: A confocal microscopy study. *Glia*, 23(1):1–10, 1998. ISSN 1098-1136. doi: 10.1002/(SICI)1098-1136(199805)23:1<1::AID-GLIA1>3.0.CO;2-B. URL https://onlinelibrary.wiley.com/doi/abs/10.1002/%28SICI%291098-1136%28199805%2923%3A1%3C1%3A%3AAID-GLIA1%3E3.0.CO%3B2-B. _eprint: https://onlinelibrary.wiley.com/doi/pdf/10.1002/%28SICI%291098-1136%28199805%2923%3A1%3C1%3A%3AAID-GLIA1%3E3.0.CO%3B2-B.

Lida Kanari, Paweł Dłotko, Martina Scolamiero, Ran Levi, Julian Shillcock, Kathryn Hess, and Henry Markram. A Topological Representation of Branching Neuronal Morphologies. *Neuroinformatics*, 16(1):3–13, January 2018. ISSN 1559-0089. doi: 10.1007/s12021-017-9341-1. URL https://doi.org/10.1007/s12021-017-9341-1.

Lida Kanari, Hugo Dictus, Athanassia Chalimourda, Werner Van Geit, Benoit Coste, Julian Shillcock, Kathryn Hess, and Henry Markram. Computational synthesis of cortical dendritic morphologies. *bioRxiv*, page 2020.04.15.040410, April 2020. doi: 10.1101/2020.04.15.040410. URL https://www.biorxiv.org/content/10.1101/2020.04.15.040410v1. Publisher: Cold Spring Harbor Laboratory Section: New Results.

Jan Karbowski. Cortical composition hierarchy driven by spine proportion economical maximization or wire volume minimization. *PLoS Comput Biol*, 11(10):e1004532, 2015. ISSN 1553-7358. Publisher: Public Library of Science.

Pegah Kassraian-Fard, Michael Pfeiffer, and Roman Bauer. A generative growth model for thalamocortical axonal branching in primary visual cortex. *PLOS Computational Biology*, 16(2):e1007315, February 2020. ISSN 1553-7358. doi: 10.1371/journal.pcbi.

1007315. URL https://journals.plos.org/ploscompbiol/article?id=10.1371/journal.pcbi.1007315. Publisher: Public Library of Science.

Narayanan Kasthuri, Kenneth Jeffrey Hayworth, Daniel Raimund Berger, Richard Lee Schalek, José Angel Conchello, Seymour Knowles-Barley, Dongil Lee, Amelio Vázquez-Reina, Verena Kaynig, Thouis Raymond Jones, Mike Roberts, Josh Lyskowski Morgan, Juan Carlos Tapia, H. Sebastian Seung, William Gray Roncal, Joshua Tzvi Vogelstein, Randal Burns, Daniel Lewis Sussman, Carey Eldin Priebe, Hanspeter Pfister, and Jeff William Lichtman. Saturated Reconstruction of a Volume of Neocortex. *Cell*, 162(3):648–661, July 2015. ISSN 0092-8674. doi: 10.1016/j.cell.2015.06.054. URL http://www.sciencedirect.com/science/article/pii/S0092867415008247.

Cihan Bilge Kayasandik, Wenjuan Ru, and Demetrio Labate. A multistep deep learning framework for the automated detection and segmentation of astrocytes in fluorescent images of brain tissue. *Scientific Reports*, 10(1):5137, March 2020. ISSN 2045-2322. doi: 10.1038/s41598-020-61953-9. URL https://www.nature.com/articles/s41598-020-61953-9. Number: 1 Publisher: Nature Publishing Group.

Baljit S. Khakh and Michael V. Sofroniew. Diversity of astrocyte functions and phenotypes in neural circuits. *Nature Neuroscience*, 18(7):942–952, July 2015. ISSN 1097-6256. doi: 10.1038/nn.4043. URL http://www.nature.com/neuro/journal/v18/n7/abs/nn.4043.html.

Vitaly A Klyachko and Charles F Stevens. Connectivity optimization and the positioning of cortical areas. *Proceedings of the National Academy of Sciences*, 100(13):7937–7941, 2003. ISSN 0027-8424. Publisher: National Acad Sciences.

Randal A Koene, Betty Tijms, Peter van Hees, Frank Postma, Alexander de Ridder, Ger JA Ramakers, Jaap van Pelt, and Arjen van Ooyen. NETMORPH: a framework for the stochastic generation of large scale neuronal networks with realistic neuron morphologies. *Neuroinformatics*, 7(3):195–210, 2009. ISSN 1539-2791. Publisher: Springer.

Natalya Korogod, Carl CH Petersen, and Graham W Knott. Ultrastructural analysis of adult mouse neocortex comparing aldehyde perfusion with cryo fixation. *eLife*, 4:e05793, August 2015. ISSN 2050-084X. doi: 10.7554/eLife.05793. URL https://doi.org/10.7554/eLife.05793. Publisher: eLife Sciences Publications, Ltd.

Hideaki Kubotera, Hiroko Ikeshima-Kataoka, Yoshiki Hatashita, Anna Letizia Allegra Mascaro, Francesco Saverio Pavone, and Takafumi Inoue. Astrocytic endfeet re-

cover blood vessels after removal by laser ablation. *Scientific Reports*, 9(1):1263, February 2019. ISSN 2045-2322. doi: 10.1038/s41598-018-37419-4. URL https://www.nature.com/articles/s41598-018-37419-4.

Prathamesh M. Kulkarni, Emily Barton, Michalis Savelonas, Raghav Padmanabhan, Yanbin Lu, Kristen Trett, William Shain, J. Leigh Leasure, and Badrinath Roysam. Quantitative 3-D analysis of GFAP labeled astrocytes from fluorescence confocal images. *Journal of Neuroscience Methods*, 246:38–51, May 2015. ISSN 0165-0270. doi: 10.1016/j.jneumeth.2015.02.014. URL http://www.sciencedirect.com/science/article/pii/S0165027015000667.

Gewebelehre Kölliker. Bd. II. *S*, 706:1854, 1896.

Johannes Köster and Sven Rahmann. Snakemake—a scalable bioinformatics workflow engine. *Bioinformatics*, 28(19):2520–2522, October 2012. ISSN 1367-4803. doi: 10.1093/bioinformatics/bts480. URL https://academic.oup.com/bioinformatics/article/28/19/2520/290322. Publisher: Oxford Academic.

Jules Lallouette, Maurizio De Pittà, Eshel Ben-Jacob, and Hugues Berry. Sparse short-distance connections enhance calcium wave propagation in a 3D model of astrocyte networks. *Frontiers in Computational Neuroscience*, 8, 2014. ISSN 1662-5188. doi: 10.3389/fncom.2014.00045. URL https://www.frontiersin.org/articles/10.3389/fncom.2014.00045/full.

Matthias Landgraf and Jan Felix Evers. Control of dendritic diversity. *Current Opinion in Cell Biology*, 17(6):690–696, December 2005. ISSN 0955-0674. doi: 10.1016/j.ceb.2005.09.005. URL http://www.sciencedirect.com/science/article/pii/S0955067405001444.

Darin Lanjakornsiripan, Baek-Jun Pior, Daichi Kawaguchi, Shohei Furutachi, Tomoaki Tahara, Yu Katsuyama, Yutaka Suzuki, Yugo Fukazawa, and Yukiko Gotoh. Layer-specific morphological and molecular differences in neocortical astrocytes and their dependence on neuronal layers. *Nature Communications*, 9(1):1623, April 2018. ISSN 2041-1723. doi: 10.1038/s41467-018-03940-3. URL https://www.nature.com/articles/s41467-018-03940-3.

Conor Leahy, Harsha Radhakrishnan, and Vivek J. Srinivasan. Volumetric imaging and quantification of cytoarchitecture and myeloarchitecture with intrinsic scattering contrast. *Biomedical Optics Express*, 4(10):1978–1990, October 2013. ISSN 2156-7085. doi: 10.1364/BOE.4.001978. URL http://www.osapublishing.org/abstract.cfm?uri=boe-4-10-1978.

Junghee Lee, Seung Jae Hyeon, Hyeonjoo Im, Hyun Ryu, Yunha Kim, and Hoon Ryu. Astrocytes and microglia as non-cell autonomous players in the pathogenesis of ALS. *Experimental neurobiology*, 25(5):233–240, 2016. ISSN 1226-2560.

RL Leino, DZ Gerhart, AM Van Bueren, AL McCall, and Lester R Drewes. Ultrastructural localization of GLUT 1 and GLUT 3 glucose transporters in rat brain. *Journal of neuroscience research*, 49(5):617–626, 1997. ISSN 0360-4012. Publisher: Wiley Online Library.

G Leuba and LJ Garey. Comparison of neuronal and glial numerical density in primary and secondary visual cortex of man. *Experimental brain research*, 77(1):31–38, 1989. ISSN 0014-4819. Publisher: Springer.

Steven W. Levison and James E. Goldman. Both oligodendrocytes and astrocytes develop from progenitors in the subventricular zone of postnatal rat forebrain. *Neuron*, 10(2): 201–212, February 1993. ISSN 0896-6273. doi: 10.1016/0896-6273(93)90311-E. URL http://www.sciencedirect.com/science/article/pii/089662739390311E.

JiaJia Li, Yong Xie, YuGuo Yu, MengMeng Du, Rong Wang, and Ying Wu. A neglected GABAergic astrocyte: Calcium dynamics and involvement in seizure activity. *Science China Technological Sciences*, 60(7):1003–1010, 2017. ISSN 1674-7321. Publisher: Springer.

Jyh-Ming Lien, Marco Morales, and Nancy M Amato. Neuron prm: A framework for constructing cortical networks. *Neurocomputing*, 52:191–197, 2003. ISSN 0925-2312. Publisher: Elsevier.

Aristid Lindenmayer. Mathematical models for cellular interactions in development II. Simple and branching filaments with two-sided inputs. *Journal of theoretical biology*, 18(3):300–315, 1968. ISSN 0022-5193. Publisher: Elsevier.

Kenneth A. Lindsay, David J. Maxwell, Jay R. Rosenberg, and Gayle Tucker. A new approach to reconstruction models of dendritic branching patterns. *Mathematical Biosciences*, 205(2):271–296, February 2007. ISSN 0025-5564. doi: 10.1016/j.mbs.2006.08.005. URL http://www.sciencedirect.com/science/article/pii/S0025556406001258.

Artur Luczak. Spatial embedding of neuronal trees modeled by diffusive growth. *Journal of neuroscience methods*, 157(1):132–141, 2006. ISSN 0165-0270. Publisher: Elsevier.

Artur Luczak. Measuring Neuronal Branching Patterns Using Model-Based Approach. *Frontiers in Computational Neuroscience*, 4, October 2010. ISSN 1662-5188.

doi: 10.3389/fncom.2010.00135. URL http://www.ncbi.nlm.nih.gov/pmc/articles/PMC2978053/.

Mónica López-Hidalgo and James Schummers. Cortical maps: a role for astrocytes? *Current opinion in neurobiology*, 24:176–189, 2014. ISSN 0959-4388. Publisher: Elsevier.

Mónica López-Hidalgo, Walter B. Hoover, and James Schummers. Spatial organization of astrocytes in ferret visual cortex. *Journal of Comparative Neurology*, 524(17):3561–3576, 2016. ISSN 1096-9861. doi: 10.1002/cne.24015. URL https://onlinelibrary.wiley.com/doi/abs/10.1002/cne.24015. _eprint: https://onlinelibrary.wiley.com/doi/pdf/10.1002/cne.24015.

Baofeng Ma, Richard Buckalew, Yixing Du, Conrad M. Kiyoshi, Catherine C. Alford, Wei Wang, Dana M. McTigue, John J. Enyeart, David Terman, and Min Zhou. Gap junction coupling confers isopotentiality on astrocyte syncytium. *Glia*, 64(2): 214–226, February 2016. ISSN 1098-1136. doi: 10.1002/glia.22924. URL http://onlinelibrary.wiley.com/doi/10.1002/glia.22924/abstract.

Sanjay Magavi, Drew Friedmann, Garrett Banks, Alberto Stolfi, and Carlos Lois. Coincident generation of pyramidal neurons and protoplasmic astrocytes in neocortical columns. *The Journal of Neuroscience: The Official Journal of the Society for Neuroscience*, 32(14):4762–4772, April 2012. ISSN 1529-2401. doi: 10.1523/JNEUROSCI.3560-11.2012.

Pierre J Magistretti and Igor Allaman. A cellular perspective on brain energy metabolism and functional imaging. *Neuron*, 86(4):883–901, 2015. ISSN 0896-6273. Publisher: Elsevier.

Pierre J. Magistretti and Igor Allaman. Lactate in the brain: from metabolic end-product to signalling molecule. *Nature Reviews Neuroscience*, 19(4):235–249, April 2018. ISSN 1471-0048. doi: 10.1038/nrn.2018.19. URL https://www.nature.com/articles/nrn.2018.19. Number: 4 Publisher: Nature Publishing Group.

Pierre J Magistretti and Luc Pellerin. Cellular bases of brain energy metabolism and their relevance to functional brain imaging: evidence for a prominent role of astrocytes. *Cerebral cortex*, 6(1):50–61, 1996. ISSN 1047-3211.

Pierre J Magistretti, Luc Pellerin, Douglas L Rothman, and Robert G Shulman. Energy on demand. *Science*, 283(5401):496–497, 1999. ISSN 0036-8075. Publisher: American Association for the Advancement of Science.

Toma Marinov, Haven A. López Sánchez, Liang Yuchi, Dayo O. Adewole, D. Kacy Cullen, and Reuben H. Kraft. A computational model of bidirectional axonal growth in micro-tissue engineered neuronal networks (micro-TENNs). *In Silico Biology*, 13 (3-4):85–99, January 2020. ISSN 1386-6338. doi: 10.3233/ISB-180172. URL https://content.iospress.com/articles/in-silico-biology/isb180172. Publisher: IOS Press.

Henry Markram, Eilif Muller, Srikanth Ramaswamy, Michael W. Reimann, Marwan Abdellah, Carlos Aguado Sanchez, Anastasia Ailamaki, Lidia Alonso-Nanclares, Nicolas Antille, Selim Arsever, Guy Antoine Atenekeng Kahou, Thomas K. Berger, Ahmet Bilgili, Nenad Buncic, Athanassia Chalimourda, Giuseppe Chindemi, Jean-Denis Courcol, Fabien Delalondre, Vincent Delattre, Shaul Druckmann, Raphael Dumusc, James Dynes, Stefan Eilemann, Eyal Gal, Michael Emiel Gevaert, Jean-Pierre Ghobril, Albert Gidon, Joe W. Graham, Anirudh Gupta, Valentin Haenel, Etay Hay, Thomas Heinis, Juan B. Hernando, Michael Hines, Lida Kanari, Daniel Keller, John Kenyon, Georges Khazen, Yihwa Kim, James G. King, Zoltan Kisvarday, Pramod Kumbhar, Sébastien Lasserre, Jean-Vincent Le Bé, Bruno R. C. Magalhães, Angel Merchán-Pérez, Julie Meystre, Benjamin Roy Morrice, Jeffrey Muller, Alberto Muñoz-Céspedes, Shruti Muralidhar, Keerthan Muthurasa, Daniel Nachbaur, Taylor H. Newton, Max Nolte, Aleksandr Ovcharenko, Juan Palacios, Luis Pastor, Rodrigo Perin, Rajnish Ranjan, Imad Riachi, José-Rodrigo Rodríguez, Juan Luis Riquelme, Christian Rössert, Konstantinos Sfyrakis, Ying Shi, Julian C. Shillcock, Gilad Silberberg, Ricardo Silva, Farhan Tauheed, Martin Telefont, Maria Toledo-Rodriguez, Thomas Tränkler, Werner Van Geit, Jafet Villafranca Díaz, Richard Walker, Yun Wang, Stefano M. Zaninetta, Javier DeFelipe, Sean L. Hill, Idan Segev, and Felix Schürmann. Reconstruction and Simulation of Neocortical Microcircuitry. *Cell*, 163(2):456–492, October 2015. ISSN 0092-8674, 1097-4172. doi: 10.1016/j.cell.2015.09.029. URL /cell/abstract/S0092-8674(15)01191-5.

David L Martin and Karin Rimvall. Regulation of gamma-aminobutyric acid synthesis in the brain. *Journal of neurochemistry*, 60(2):395–407, 1993. ISSN 0022-3042. Publisher: Wiley Online Library.

Miguel Marín-padilla. Prenatal development of fibrous (white matter), protoplasmic (gray matter), and layer I astrocytes in the human cerebral cortex: a Golgi study. *Journal of Comparative Neurology*, 357(4):554–572, 1995. ISSN 0021-9967. Publisher: Wiley Online Library.

Thomas Misje Mathiisen, Knut Petter Lehre, Niels Christian Danbolt, and Ole Petter Ottersen. The perivascular astroglial sheath provides a complete covering of the brain microvessels: an electron microscopic 3D reconstruction. *Glia*, 58(9):1094–1103, 2010. ISSN 0894-1491. Publisher: Wiley Online Library.

Vitali Matyash and Helmut Kettenmann. Heterogeneity in astrocyte morphology and physiology. *Brain Research Reviews*, 63(1):2–10, May 2010. ISSN 0165-0173. doi: 10.1016/j.brainresrev.2009.12.001. URL http://www.sciencedirect.com/science/article/pii/S0165017309001295.

A. Kimberley McAllister. Cellular and Molecular Mechanisms of Dendrite Growth. *Cerebral Cortex*, 10(10):963–973, October 2000. ISSN 1047-3211. doi: 10.1093/cercor/10.10.963. URL https://academic.oup.com/cercor/article/10/10/963/608101. Publisher: Oxford Academic.

Addason FH McCaslin, Brenda R Chen, Andrew J Radosevich, Bruno Cauli, and Elizabeth MC Hillman. in vivo 3D Morphology of Astrocyte—Vasculature Interactions in the Somatosensory Cortex: Implications for Neurovascular Coupling. *Journal of cerebral blood flow & metabolism*, 31(3):795–806, 2011. ISSN 0271-678X. Publisher: SAGE Publications Sage UK: London, England.

Bruce Howard McCormick and K Mulchandani. L-system modeling of neurons. volume 2359, pages 693–705. International Society for Optics and Photonics, 1994.

Nikolai Medvedev, Victor Popov, Christian Henneberger, Igor Kraev, Dmitri A Rusakov, and Michael G Stewart. Glia selectively approach synapses on thin dendritic spines. *Philosophical Transactions of the Royal Society B: Biological Sciences*, 369(1654): 20140047, 2014. ISSN 0962-8436. Publisher: The Royal Society.

Heraldo Memelli, Benjamin Torben-Nielsen, and James Kozloski. Self-referential forces are sufficient to explain different dendritic morphologies. *Frontiers in Neuroinformatics*, 7, 2013. ISSN 1662-5196. doi: 10.3389/fninf.2013.00001. URL http://journal.frontiersin.org/article/10.3389/fninf.2013.00001/abstract.

Huaiyu Mi, Henry Haeberle, and Ben A Barres. Induction of astrocyte differentiation by endothelial cells. *Journal of Neuroscience*, 21(5):1538–1547, 2001. ISSN 0270-6474. Publisher: Soc Neuroscience.

Yuriy Mishchenko, Tao Hu, Josef Spacek, John Mendenhall, Kristen M Harris, and Dmitri B Chklovskii. Ultrastructural analysis of hippocampal neuropil from the

connectomics perspective. *Neuron*, 67(6):1009–1020, 2010. ISSN 0896-6273. Publisher: Elsevier.

Tsuneko Mishima and Hajime Hirase. In vivo intracellular recording suggests that gray matter astrocytes in mature cerebral cortex and hippocampus are electrophysiologically homogeneous. *The Journal of Neuroscience: The Official Journal of the Society for Neuroscience*, 30(8):3093–3100, February 2010. ISSN 1529-2401. doi: 10.1523/JNEUROSCI.5065-09.2010.

Anusha Mishra, Arif Hamid, and Eric A Newman. Oxygen modulation of neurovascular coupling in the retina. *Proceedings of the National Academy of Sciences*, 108(43): 17827–17831, 2011. ISSN 0027-8424. Publisher: National Acad Sciences.

Stefanie L. Moye, Blanca Diaz-Castro, Mohitkumar R. Gangwani, and Baljit S. Khakh. Visualizing Astrocyte Morphology Using Lucifer Yellow Iontophoresis. *JoVE (Journal of Visualized Experiments)*, (151):e60225, September 2019. ISSN 1940-087X. doi: 10.3791/60225. URL https://www.jove.com/video/60225/visualizing-astrocyte-morphology-using-lucifer-yellow-iontophoresis.

Souhel Najjar, Daniel M Pearlman, Orrin Devinsky, Amanda Najjar, and David Zagzag. Neurovascular unit dysfunction with blood-brain barrier hyperpermeability contributes to major depressive disorder: a review of clinical and experimental evidence. *Journal of neuroinflammation*, 10(1):906, 2013. ISSN 1742-2094. Publisher: Springer.

Klaus-Armin Nave and Bruce D Trapp. Axon-glial signaling and the glial support of axon function. *Annu. Rev. Neurosci.*, 31:535–561, 2008. ISSN 0147-006X. Publisher: Annual Reviews.

Maiken Nedergaard, Bruce Ransom, and Steven A. Goldman. New roles for astrocytes: Redefining the functional architecture of the brain. *Trends in Neurosciences*, 26 (10):523–530, October 2003. ISSN 0166-2236. doi: 10.1016/j.tins.2003.08.008. URL http://www.sciencedirect.com/science/article/pii/S0166223603002662.

Axel Nimmerjahn, Frank Kirchhoff, Jason N. D. Kerr, and Fritjof Helmchen. Sulforhodamine 101 as a specific marker of astroglia in the neocortex in vivo. *Nature Methods*, 1(1):31–37, October 2004. ISSN 1548-7105. doi: 10.1038/nmeth706. URL https://www.nature.com/articles/nmeth706. Number: 1 Publisher: Nature Publishing Group.

Axel Nimmerjahn, Frank Kirchhoff, and Fritjof Helmchen. Resting microglial cells are highly dynamic surveillants of brain parenchyma in vivo. *Science*, 308(5726):1314–1318, 2005. ISSN 0036-8075. Publisher: American Association for the Advancement of Science.

Mutsuo Nuriya and Masato Yasui. Endfeet serve as diffusion-limited subcellular compartments in astrocytes. *Journal of Neuroscience*, 33(8):3692–3698, 2013. ISSN 0270-6474. Publisher: Soc Neuroscience.

Nancy Ann Oberheim, Takahiro Takano, Xiaoning Han, Wei He, Jane H. C. Lin, Fushun Wang, Qiwu Xu, Jeffrey D. Wyatt, Webster Pilcher, Jeffrey G. Ojemann, Bruce R. Ransom, Steven A. Goldman, and Maiken Nedergaard. Uniquely hominid features of adult human astrocytes. *The Journal of Neuroscience: The Official Journal of the Society for Neuroscience*, 29(10):3276–3287, March 2009. ISSN 1529-2401. doi: 10.1523/JNEUROSCI.4707-08.2009.

Marcel Oberlaender, Christiaan P. J. de Kock, Randy M. Bruno, Alejandro Ramirez, Hanno S. Meyer, Vincent J. Dercksen, Moritz Helmstaedter, and Bert Sakmann. Cell Type–Specific Three-Dimensional Structure of Thalamocortical Circuits in a Column of Rat Vibrissal Cortex. *Cerebral Cortex*, 22(10):2375–2391, October 2012. ISSN 1047-3211. doi: 10.1093/cercor/bhr317. URL https://academic.oup.com/cercor/article/22/10/2375/289513. Publisher: Oxford Academic.

Steffen Oeltze and Bernhard Preim. Visualization of anatomic tree structures with convolution surfaces. pages 311–320, 2004.

K Ogata and T Kosaka. Structural and quantitative analysis of astrocytes in the mouse hippocampus. *Neuroscience*, 113(1):221–233, August 2002. ISSN 0306-4522. doi: 10.1016/S0306-4522(02)00041-6. URL http://www.sciencedirect.com/science/article/pii/S0306452202000416.

Markel Olabarria, Harun N Noristani, Alexei Verkhratsky, and José J Rodríguez. Concomitant astroglial atrophy and astrogliosis in a triple transgenic animal model of Alzheimer's disease. *Glia*, 58(7):831–838, 2010. ISSN 0894-1491. Publisher: Wiley Online Library.

Matthew A Olude, Oluwaseun A Mustapha, Oluwatunde A Aderounmu, James O Olopade, and Amadi O Ihunwo. Astrocyte morphology, heterogeneity, and density in the developing African giant rat (Cricetomys gambianus). *Frontiers in neuroanatomy*, 9:67, 2015. ISSN 1662-5129. Publisher: Frontiers.

RK Orkand, JG Nicholls, and SW Kuffler. Effect of nerve impulses on the membrane potential of glial cells in the central nervous system of amphibia. *Journal of neurophysiology*, 29(4):788–806, 1966. ISSN 0022-3077.

Aude Panatier, Joanne Vallée, Michael Haber, Keith K Murai, Jean-Claude Lacaille, and Richard Robitaille. Astrocytes are endogenous regulators of basal transmission at central synapses. *Cell*, 146(5):785–798, 2011. ISSN 0092-8674. Publisher: Elsevier.

Ruchi Parekh and Giorgio A Ascoli. Neuronal morphology goes digital: a research hub for cellular and system neuroscience. *Neuron*, 77(6):1017–1038, 2013. ISSN 0896-6273. Publisher: Elsevier.

Vladimir Parpura, Trent A Basarsky, Fang Liu, Ksenija Jeftinija, Srdija Jeftinija, and Philip G Haydon. Glutamate-mediated astrocyte–neuron signalling. *Nature*, 369(6483): 744–747, 1994. ISSN 0028-0836. Publisher: Springer.

Vladimir Parpura, Michael T Heneka, Vedrana Montana, Stéphane HR Oliet, Arne Schousboe, Philip G Haydon, Randy F Stout Jr, David C Spray, Andreas Reichenbach, and Thomas Pannicke. Glial cells in (patho) physiology. *Journal of neurochemistry*, 121(1):4–27, 2012. ISSN 0022-3042. Publisher: Wiley Online Library.

Olivier Pascual, Sarrah Ben Achour, Philippe Rostaing, Antoine Triller, and Alain Bessis. Microglia activation triggers astrocyte-mediated modulation of excitatory neurotransmission. *Proceedings of the National Academy of Sciences*, 109(4):E197–E205, 2012. ISSN 0027-8424. Publisher: National Acad Sciences.

Luc Pellerin and Pierre J Magistretti. Glutamate uptake into astrocytes stimulates aerobic glycolysis: a mechanism coupling neuronal activity to glucose utilization. *Proceedings of the National Academy of Sciences*, 91(22):10625–10629, 1994. ISSN 0027-8424. Publisher: National Acad Sciences.

AJ Pellionisz. Neural geometry: towards a fractal model of neurons. *Models of brain function. Cambridge University Press, Cambridge*, pages 453–464, 1989.

Dorte P Pelvig, Henning Pakkenberg, Lisbeth Regeur, Solveig Oster, and Bente Pakkenberg. Neocortical glial cell numbers in Alzheimer's disease. *Dementia and geriatric cognitive disorders*, 16(4):212–219, 2003. ISSN 1420-8008. Publisher: Karger Publishers.

Ognen AC Petroff, Laura D Errante, Douglas L Rothman, Jung H Kim, and Dennis D Spencer. Glutamate–glutamine cycling in the epileptic human hippocampus. *Epilepsia*, 43(7):703–710, 2002. ISSN 0013-9580. Publisher: Wiley Online Library.

F. Plourabouré, P. Cloetens, C. Fonta, A. Steyer, F. Lauwers, and J.-P. Marc-Vergnes. X-ray high-resolution vascular network imaging. *Journal of Microscopy*, 215(2):139–148, August 2004. ISSN 1365-2818. doi: 10.1111/j.0022-2720.2004.01362.x. URL http://onlinelibrary.wiley.com/doi/10.1111/j.0022-2720.2004.01362.x/abstract.

Till B Puschmann, Carl Zandén, Isabell Lebkuechner, Camille Philippot, Yolanda de Pablo, Johan Liu, and Milos Pekny. HB-EGF affects astrocyte morphology, proliferation, differentiation, and the expression of intermediate filament proteins. *Journal of neurochemistry*, 128(6):878–889, 2014. ISSN 0022-3042. Publisher: Wiley Online Library.

Grazyna Rajkowska, Jonathan Hughes, Craig A. Stockmeier, Jose Javier Miguel-Hidalgo, and Dorota Maciag. Coverage of Blood Vessels by Astrocytic Endfeet Is Reduced in Major Depressive Disorder. *Biological Psychiatry*, 73(7):613–621, April 2013. ISSN 0006-3223. doi: 10.1016/j.biopsych.2012.09.024. URL http://www.sciencedirect.com/science/article/pii/S0006322312008505.

Bruce R. Ransom. *Neuroglia*. Oxford University Press, November 2012. ISBN 978-0-19-979473-7. Google-Books-ID: y40NAwAAQBAJ.

Ron Refaeli, Adi Doron, Aviya Benmelech-Chovav, Maya Groysman, Tirzah Kreisel, Yonatan Loewenstein, and Inbal Goshen. Features Of Hippocampal Astrocytic Domains And Their Spatial Relation To Excitatory And Inhibitory Neurons. *bioRxiv*, 2020. Publisher: Cold Spring Harbor Laboratory.

Andreas Reichenbach, Amin Derouiche, and Frank Kirchhoff. Morphology and dynamics of perisynaptic glia. *Brain Research Reviews*, 63(1-2):11–25, May 2010. ISSN 1872-6321. doi: 10.1016/j.brainresrev.2010.02.003.

Johannes Reichold, Marco Stampanoni, Anna Lena Keller, Alfred Buck, Patrick Jenny, and Bruno Weber. Vascular Graph Model to Simulate the Cerebral Blood Flow in Realistic Vascular Networks. *Journal of Cerebral Blood Flow & Metabolism*, 29(8): 1429–1443, August 2009. ISSN 0271-678X, 1559-7016. doi: 10.1038/jcbfm.2009.58. URL http://jcb.sagepub.com/content/29/8/1429.

Daniel Rial, Cristina Lemos, Helena Pinheiro, Joana M Duarte, Francisco Q Gonçalves, Joana I Real, Rui D Prediger, Nélio Gonçalves, Catarina A Gomes, and Paula M Canas. Depression as a glial-based synaptic dysfunction. *Frontiers in cellular neuroscience*, 9: 521, 2016. ISSN 1662-5102. Publisher: Frontiers.

Astrid Rohlmann and J. R. Wolff. Subcellular Topography and Plasticity of Gap Junction Distribution on Astrocytes. In *Gap Junctions in the Nervous System*, Neuroscience Intelligence Unit, pages 175–192. Springer, Berlin, Heidelberg, 1996. ISBN 978-3-662-21937-9 978-3-662-21935-5. doi: 10.1007/978-3-662-21935-5_10. URL https://link.springer.com/chapter/10.1007/978-3-662-21935-5_10.

JD Rothstein, LJ Martin, and RW Kuncl. Decreased brain and spinal cord glutamate transport in amyotrophic lateral sclerosis. *N Engl J Med*, 326(1):464–1468, 1992.

Jeffrey D Rothstein, Marleen Van Kammen, Allan I Levey, Lee J Martin, and Ralph W Kuncl. Selective loss of glial glutamate transporter GLT-1 in amyotrophic lateral sclerosis. *Annals of Neurology: Official Journal of the American Neurological Association and the Child Neurology Society*, 38(1):73–84, 1995. ISSN 0364-5134. Publisher: Wiley Online Library.

David Ruelle. *Statistical mechanics: Rigorous results*. World Scientific, 1999. ISBN 981-02-3862-2.

Adam Runions, Martin Fuhrer, Brendan Lane, Pavol Federl, Anne-Gaëlle Rolland-Lagan, and Przemyslaw Prusinkiewicz. Modeling and Visualization of Leaf Venation Patterns. In *ACM SIGGRAPH 2005 Papers*, SIGGRAPH '05, pages 702–711, New York, NY, USA, 2005. ACM. doi: 10.1145/1186822.1073251. URL http://doi.acm.org/10.1145/1186822.1073251.

Adam Runions, Brendan Lane, and Przemyslaw Prusinkiewicz. Modeling Trees with a Space Colonization Algorithm. In *Proceedings of the Third Eurographics Conference on Natural Phenomena*, NPH'07, pages 63–70, Aire-la-Ville, Switzerland, Switzerland, 2007. Eurographics Association. ISBN 978-3-905673-49-4. doi: 10.2312/NPH/NPH07/063-070. URL http://dx.doi.org/10.2312/NPH/NPH07/063-070.

Chris Rycroft. Voro++: A three-dimensional Voronoi cell library in C++. Technical report, Lawrence Berkeley National Lab.(LBNL), Berkeley, CA (United States), 2009.

A Santuy, JR Rodriguez, Javier DeFelipe, and A Merchan-Perez. Volume electron microscopy of the distribution of synapses in the neuropil of the juvenile rat somatosensory cortex. *Brain Structure and Function*, 223(1):77–90, 2018. ISSN 1863-2653. Publisher: Springer.

Leonid P. Savtchenko, Lucie Bard, Thomas P. Jensen, James P. Reynolds, Igor Kraev, Nikolay Medvedev, Michael G. Stewart, Christian Henneberger, and Dmitri A. Rusakov.

Disentangling astroglial physiology with a realistic cell model in silico. *Nature Communications*, 9(1):3554, 2018. ISSN 2041-1723. doi: 10.1038/s41467-018-05896-w.

Dorothy P Schafer, Emily K Lehrman, and Beth Stevens. The "quad-partite" synapse: Microglia-synapse interactions in the developing and mature CNS. *Glia*, 61(1):24–36, 2013. ISSN 0894-1491. Publisher: Wiley Online Library.

Donald E Schmechel and Pasko Rakic. A Golgi study of radial glial cells in developing monkey telencephalon: morphogenesis and transformation into astrocytes. *Anatomy and embryology*, 156(2):115–152, 1979. ISSN 0340-2061. Publisher: Springer.

Franca Schmid, Matthew JP Barrett, Patrick Jenny, and Bruno Weber. Vascular density and distribution in neocortex. *Neuroimage*, 197:792–805, 2019. ISSN 1053-8119. Publisher: Elsevier.

Arne Schousboe, Lasse Kristoffer Bak, and Helle Sønderby Waagepetersen. Astrocytic control of biosynthesis and turnover of the neurotransmitters glutamate and GABA. *Frontiers in endocrinology*, 4:102, 2013. ISSN 1664-2392. Publisher: Frontiers.

Alexandra E Schreiner, Simone Durry, Tomomi Aida, Martin C Stock, Ulrich Rüther, Kohichi Tanaka, Christine R Rose, and Karl W Kafitz. Laminar and subcellular heterogeneity of GLAST and GLT-1 immunoreactivity in the developing postnatal mouse hippocampus. *Journal of Comparative Neurology*, 522(1):204–224, 2014. ISSN 0021-9967. Publisher: Wiley Online Library.

Michael D Scofield, Hao Li, Benjamin M Siemsen, Kati L Healey, Phuong K Tran, Nicholas Woronoff, Heather A Boger, Peter W Kalivas, and Kathryn J Reissner. Cocaine self-administration and extinction leads to reduced glial fibrillary acidic protein expression and morphometric features of astrocytes in the nucleus accumbens core. *Biological psychiatry*, 80(3):207–215, 2016. ISSN 0006-3223. Publisher: Elsevier.

Ruggero Scorcioni, Sridevi Polavaram, and Giorgio A Ascoli. L-Measure: a web-accessible tool for the analysis, comparison and search of digital reconstructions of neuronal morphologies. *Nature protocols*, 3(5):866, 2008. ISSN 1750-2799. Publisher: Nature Publishing Group.

David W Scott. *Multivariate density estimation: theory, practice, and visualization*. John Wiley & Sons, 2015. ISBN 0-471-69755-9.

Ethan K. Scott and Liqun Luo. How do dendrites take their shape? *Nature Neuroscience*, 4(4):359–365, April 2001. ISSN 1546-1726. doi: 10.1038/86006. URL https://www.nature.com/articles/nn0401_359. Number: 4 Publisher: Nature Publishing Group.

Raphaël Serduc, Pascale Vérant, Jean-Claude Vial, Régine Farion, Linda Rocas, Chantal Rémy, Taoufik Fadlallah, Elke Brauer, Alberto Bravin, and Jean Laissue. In vivo two-photon microscopy study of short-term effects of microbeam irradiation on normal mouse brain microvasculature. *International Journal of Radiation Oncology* Biology* Physics*, 64(5):1519–1527, 2006. ISSN 0360-3016. Publisher: Elsevier.

Yonatan Serlin, Ilan Shelef, Boris Knyazer, and Alon Friedman. Anatomy and physiology of the blood–brain barrier. volume 38, pages 2–6. Elsevier, 2015. ISBN 1084-9521.

Nikhil Sharma, Jean-Claude Baron, and James B Rowe. Motor imagery after stroke: relating outcome to motor network connectivity. *Annals of Neurology: Official Journal of the American Neurological Association and the Child Neurology Society*, 66(5): 604–616, 2009. ISSN 0364-5134. Publisher: Wiley Online Library.

Carol A Sheppard, Peter B Simpson, Alan H Sharp, Frederick C Nucifora, Christopher A Ross, G David Lange, and James T Russell. Comparison of type 2 inositol 1, 4, 5-trisphosphate receptor distribution and subcellular Ca2+ release sites that support Ca2+ waves in cultured astrocytes. *Journal of neurochemistry*, 68(6):2317–2327, 1997. ISSN 0022-3042. Publisher: Wiley Online Library.

Marie Simard, Gregory Arcuino, Takahiro Takano, Qing Song Liu, and Maiken Nedergaard. Signaling at the Gliovascular Interface. *Journal of Neuroscience*, 23(27): 9254–9262, October 2003. ISSN 0270-6474, 1529-2401. doi: 10.1523/JNEUROSCI.23-27-09254.2003. URL https://www.jneurosci.org/content/23/27/9254. Publisher: Society for Neuroscience Section: Cellular/Molecular.

T. G. Smith, G. D. Lange, and W. B. Marks. Fractal methods and results in cellular morphology — dimensions, lacunarity and multifractals. *Journal of Neuroscience Methods*, 69(2):123–136, November 1996. ISSN 0165-0270. doi: 10.1016/S0165-0270(96)00080-5. URL http://www.sciencedirect.com/science/article/pii/S0165027096000805.

Michael V. Sofroniew and Harry V. Vinters. Astrocytes: biology and pathology. *Acta Neuropathologica*, 119(1):7–35, January 2010. ISSN 0001-6322. doi: 10.1007/s00401-009-0619-8. URL https://www.ncbi.nlm.nih.gov/pmc/articles/PMC2799634/.

Ursula Sonnewald and Daniel Kondziella. Neuronal glial interaction in different neurological diseases studied by ex vivo 13C NMR spectroscopy. *NMR in Biomedicine: An International Journal Devoted to the Development and Application of Magnetic Resonance In Vivo*, 16(6-7):424–429, 2003. ISSN 0952-3480. Publisher: Wiley Online Library.

Alexander A Sosunov, Xiaoping Wu, Nadejda M Tsankova, Eileen Guilfoyle, Guy M McKhann, and James E Goldman. Phenotypic heterogeneity and plasticity of isocortical and hippocampal astrocytes in the human brain. *Journal of Neuroscience*, 34(6):2285–2298, 2014. ISSN 0270-6474. Publisher: Soc Neuroscience.

Armen Stepanyants, Luis M Martinez, Alex S Ferecskó, and Zoltán F Kisvárday. The fractions of short-and long-range connections in the visual cortex. *Proceedings of the National Academy of Sciences*, 106(9):3555–3560, 2009. ISSN 0027-8424. Publisher: National Acad Sciences.

Charles E Stout, James L Costantin, Christian CG Naus, and Andrew C Charles. Intercellular calcium signaling in astrocytes via ATP release through connexin hemichannels. *Journal of Biological Chemistry*, 277(12):10482–10488, 2002. ISSN 0021-9258. Publisher: ASBMB.

Rudi K Tannenberg, Heather L Scott, Robert I Westphalen, and Peter R Dodd. The identification and characterization of excitotoxic nerve-endings in Alzheimer disease. *Current Alzheimer Research*, 1(1):11–25, 2004. ISSN 1567-2050. Publisher: Bentham Science Publishers.

Gabriela Tavares, Manuella Martins, Joana Sofia Correia, Vanessa Morais Sardinha, Sónia Guerra-Gomes, Sofia Pereira das Neves, Fernanda Marques, Nuno Sousa, and João Filipe Oliveira. Employing an open-source tool to assess astrocyte tridimensional structure. *Brain Structure & Function*, 222(4):1989–1999, May 2017. ISSN 1863-2661. doi: 10.1007/s00429-016-1316-8.

Gaia Tavosanis. Dendritic structural plasticity. *Developmental neurobiology*, 72(1):73–86, 2012. ISSN 1932-8451. Publisher: Wiley Online Library.

Mihail Ivilinov Todorov, Johannes C. Paetzold, Oliver Schoppe, Giles Tetteh, Velizar Efremov, Katalin Völgyi, Marco Düring, Martin Dichgans, Marie Piraud, Bjoern Menze, and Ali Ertürk. Automated analysis of whole brain vasculature using machine learning. *bioRxiv*, page 613257, April 2019. doi: 10.1101/613257. URL https://www.

biorxiv.org/content/10.1101/613257v1. Publisher: Cold Spring Harbor Laboratory Section: New Results.

Xiaoping Tong, Yan Ao, Guido C Faas, Sinifunanya E Nwaobi, Ji Xu, Martin D Haustein, Mark A Anderson, Istvan Mody, Michelle L Olsen, and Michael V Sofroniew. Astrocyte Kir4. 1 ion channel deficits contribute to neuronal dysfunction in Huntington's disease model mice. *Nature neuroscience*, 17(5):694–703, 2014. ISSN 1546-1726. Publisher: Nature Publishing Group.

Ben Torben-Nielsen, Karl Tuyls, and Eric Postma. Evol-neuron: Neuronal morphology generation. *Neurocomputing*, 71(4-6):963–972, 2008. ISSN 0925-2312. Publisher: Elsevier.

S. Tout, Z. Dreher, T. Chan-Ling, and J. Stone. Contact-spacing among astrocytes is independent of neighbouring structures: in vivo and in vitro evidence. *The Journal of Comparative Neurology*, 332(4):433–443, June 1993. ISSN 0021-9967. doi: 10.1002/cne.903320405.

D. B. Tower and O. M. Young. The Activities of Butyrylcholinesterase and Carbonic Anhydrase, the Rate of Anaerobic Glycolysts, and the Question of a Constant Density of Glial Cells in Cerebral Cortices of Various Mammalian Species from Mouse to Whale. *Journal of Neurochemistry*, 20(2):269–278, 1973. ISSN 1471-4159. doi: 10.1111/j.1471-4159.1973.tb12126.x. URL https://onlinelibrary.wiley.com/doi/abs/10.1111/j.1471-4159.1973.tb12126.x. _eprint: https://onlinelibrary.wiley.com/doi/pdf/10.1111/j.1471-4159.1973.tb12126.x.

Marie-Ève Tremblay, Rebecca L Lowery, and Ania K Majewska. Microglial interactions with synapses are modulated by visual experience. *PLoS Biol*, 8(11):e1000527, 2010. ISSN 1545-7885. Publisher: Public Library of Science.

Philbert S Tsai, John P Kaufhold, Pablo Blinder, Beth Friedman, Patrick J Drew, Harvey J Karten, Patrick D Lyden, and David Kleinfeld. Correlations of neuronal and microvascular densities in murine cortex revealed by direct counting and colocalization of nuclei and vessels. *Journal of Neuroscience*, 29(46):14553–14570, 2009. ISSN 0270-6474. Publisher: Soc Neuroscience.

Egor Turovsky, Anastassios Karagiannis, Ana Paula Abdala, and Alexander V Gourine. Impaired CO2 sensitivity of astrocytes in a mouse model of Rett syndrome. *The Journal of physiology*, 593(14):3159–3168, 2015. ISSN 0022-3751. Publisher: Wiley Online Library.

L Fejes Tóth. Illumination of convex discs. *Acta Mathematica Academiae Scientiarum Hungaricae*, 29(3-4):355–360, 1977. ISSN 0001-5954. Publisher: Springer.

Hiroki R. Ueda, Hans-Ulrich Dodt, Pavel Osten, Michael N. Economo, Jayaram Chandrashekar, and Philipp J. Keller. Whole-Brain Profiling of Cells and Circuits in Mammals by Tissue Clearing and Light-Sheet Microscopy. *Neuron*, 106 (3):369–387, May 2020. ISSN 0896-6273. doi: 10.1016/j.neuron.2020.03.004. URL http://www.sciencedirect.com/science/article/pii/S0896627320301902.

Ghanim Ullah, Peter Jung, and Ann H Cornell-Bell. Anti-phase calcium oscillations in astrocytes via inositol (1, 4, 5)-trisphosphate regeneration. *Cell calcium*, 39(3):197–208, 2006. ISSN 0143-4160. Publisher: Elsevier.

RHH Van den Heuvel, B Curti, MA Vanoni, and A Mattevi. Glutamate synthase: a fascinating pathway from L-glutamine to L-glutamate. *Cellular and Molecular Life Sciences CMLS*, 61(6):669–681, 2004. ISSN 1420-682X. Publisher: Springer.

Ronald AJ van Elburg and Arjen van Ooyen. Impact of dendritic size and dendritic topology on burst firing in pyramidal cells. *PLoS Comput Biol*, 6(5):e1000781, 2010. ISSN 1553-7358. Publisher: Public Library of Science.

Flora Vasile, Elena Dossi, and Nathalie Rouach. Human astrocytes: structure and functions in the healthy brain. *Brain Structure and Function*, 222(5), 2017. ISSN 1863-2653. Publisher: Springer.

Rachel Ventura and Kristen M. Harris. Three-Dimensional Relationships between Hippocampal Synapses and Astrocytes. *The Journal of Neuroscience*, 19(16):6897–6906, August 1999. ISSN 0270-6474, 1529-2401. URL http://www.jneurosci.org/content/19/16/6897.

Alexei Verkhratsky and Robert Zorec. Secretory Astrocytes. In *Neurosecretion: Secretory Mechanisms*, pages 127–160. Springer, 2020.

Alexei Verkhratsky, Nancy Ann Oberheim Bush, Maiken Nedergaard, and Arthur Butt. The special case of human astrocytes. *Neuroglia*, 1(1):21–29, 2018. Publisher: Multidisciplinary Digital Publishing Institute.

Rudolf Ludwig Karl Virchow. *Die Cellularpathologie in ihrer Begründung auf physiologische und pathologische Gewebelehre*. A. Hirshcwald, 1859. Google-Books-ID: Wi31tvfv3y4C.

Vladislav Volman, Eshel Ben-Jacob, and Herbert Levine. The astrocyte as a gatekeeper of synaptic information transfer. *Neural computation*, 19(2):303–326, 2007. ISSN 0899-7667. Publisher: MIT Press.

Andrea Volterra and Jacopo Meldolesi. Astrocytes, from brain glue to communication elements: the revolution continues. *Nature Reviews Neuroscience*, 6(8):626–640, August 2005. ISSN 1471-0048. doi: 10.1038/nrn1722. URL https://www.nature.com/articles/nrn1722. Number: 8 Publisher: Nature Publishing Group.

Helle S Waagepetersen, Hong Qu, Ursula Sonnewald, Keiko Shimamoto, and Arne Schousboe. Role of glutamine and neuronal glutamate uptake in glutamate homeostasis and synthesis during vesicular release in cultured glutamatergic neurons. *Neurochemistry international*, 47(1-2):92–102, 2005. ISSN 0197-0186. Publisher: Elsevier.

Gilad Wallach, Jules Lallouette, Nitzan Herzog, Maurizio De Pittà, Eshel Ben Jacob, Hugues Berry, and Yael Hanein. Glutamate mediated astrocytic filtering of neuronal activity. *PLoS Comput Biol*, 10(12):e1003964, 2014. ISSN 1553-7358. Publisher: Public Library of Science.

Marie Xun Wang, Lori Ray, Kenji F Tanaka, Jeffrey J Iliff, and Jeffrey Heys. Varying perivascular astroglial endfoot dimensions along the vascular tree maintain perivascular-interstitial flux through the cortical mantle. *BioRxiv*, 2020. Publisher: Cold Spring Harbor Laboratory.

Xiaohai Wang, Nanhong Lou, Qiwu Xu, Guo-Feng Tian, Wei Guo Peng, Xiaoning Han, Jian Kang, Takahiro Takano, and Maiken Nedergaard. Astrocytic Ca 2+ signaling evoked by sensory stimulation in vivo. *Nature neuroscience*, 9(6):816–823, 2006. ISSN 1546-1726. Publisher: Nature Publishing Group.

Quan Wen, Armen Stepanyants, Guy N Elston, Alexander Y Grosberg, and Dmitri B Chklovskii. Maximization of the connectivity repertoire as a statistical principle governing the shapes of dendritic arbors. *Proceedings of the National Academy of Sciences*, 106(30):12536–12541, 2009. ISSN 0027-8424. Publisher: National Acad Sciences.

Ulrika Wilhelmsson, Eric A Bushong, Diana L Price, Benjamin L Smarr, Van Phung, Masako Terada, Mark H Ellisman, and Milos Pekny. Redefining the concept of reactive astrocytes as cells that remain within their unique domains upon reaction to injury. *Proceedings of the National Academy of Sciences*, 103(46):17513–17518, 2006. ISSN 0027-8424. Publisher: National Acad Sciences.

Mark R Witcher, Sergei A Kirov, and Kristen M Harris. Plasticity of perisynaptic astroglia during synaptogenesis in the mature rat hippocampus. *Glia*, 55(1):13–23, 2007. ISSN 0894-1491. Publisher: Wiley Online Library.

Alexandra Witthoft, Jessica A. Filosa, and George Em Karniadakis. Potassium Buffering in the Neurovascular Unit: Models and Sensitivity Analysis. *Biophysical Journal*, 105 (9):2046–2054, November 2013. ISSN 0006-3495. doi: 10.1016/j.bpj.2013.09.012. URL http://www.sciencedirect.com/science/article/pii/S0006349513010321.

Susanne Wolf, Stephan Grein, and Gillian Queisser. Employing NeuGen 2.0 to automatically generate realistic morphologies of hippocampal neurons and neural networks in 3D. *Neuroinformatics*, 11(2):137–148, 2013. ISSN 1539-2791. Publisher: Springer.

J. R. Wolff, K. Stuke, M. Missler, H. Tytko, P. Schwarz, A. Rohlmann, and T. I. Chao. Autocellular coupling by gap junctions in cultured astrocytes: a new view on cellular autoregulation during process formation. *Glia*, 24(1):121–140, September 1998. ISSN 0894-1491.

Thomas A Woolsey, Carl M Rovainen, Stephanie B Cox, Martin H Henegar, Griffith E Liang, Daqian Liu, Yuri E Moskalenko, Jing Sui, and Ling Wei. Neuronal units linked to microvascular modules in cerebral cortex: response elements for imaging the brain. *Cerebral Cortex*, 6(5):647–660, 1996. ISSN 1460-2199. Publisher: Oxford University Press.

Guangjin Xu, Wei Wang, Harold K. Kimelberg, and Min Zhou. Electrical coupling of astrocytes in rat hippocampal slices under physiological and simulated ischemic conditions. *Glia*, 58(4):481–493, 2010. ISSN 1098-1136. doi: 10.1002/glia.20939. URL https://onlinelibrary.wiley.com/doi/abs/10.1002/glia.20939.

Yoshihiko Yamazaki, Yasukazu Hozumi, Kenya Kaneko, Satoshi Fujii, Kaoru Goto, and Hiroshi Kato. Oligodendrocytes: facilitating axonal conduction by more than myelination. *The Neuroscientist*, 16(1):11–18, 2010. ISSN 1073-8584. Publisher: SAGE Publications Sage CA: Los Angeles, CA.

Masoumeh Zarei-Kheirabadi, Alexander R. Vaccaro, Vafa Rahimi-Movaghar, Sahar Kiani, and Hossein Baharvand. An Overview of Extrinsic and Intrinsic Mechanisms Involved in Astrocyte Development in the Central Nervous System. *Stem Cells and Development*, 29(5):266–280, December 2019. ISSN 1547-3287. doi: 10.1089/scd.2019.0189. URL https://www.liebertpub.com/doi/full/10.1089/scd.2019.0189. Publisher: Mary Ann Liebert, Inc., publishers.

Marielba Zerlin and James E. Goldman. Interactions between glial progenitors and blood vessels during early postnatal corticogenesis: Blood vessel contact represents an early stage of astrocyte differentiation. *Journal of Comparative Neurology*, 387(4):537–546, 1997. ISSN 1096-9861. doi: 10.1002/(SICI)1096-9861(19971103)387:4<537::AID-CNE5>3.0.CO;2-3. URL https://onlinelibrary.wiley.com/doi/abs/10.1002/%28SICI%291096-9861%2819971103%29387%3A4%3C537%3A%3AAID-CNE5%3E3.0.CO%3B2-3.

Berislav V Zlokovic. Neurovascular pathways to neurodegeneration in Alzheimer's disease and other disorders. *Nature Reviews Neuroscience*, 12(12):723–738, 2011. ISSN 1471-0048. Publisher: Nature Publishing Group.

F Zubler and R Douglas. CX3D: a java package for simulation of cortical development in 3D. 2008.

Eleftherios Zisis

Curriculum Vitae

✉ *elef.zisis@gmail.ch*

Technical Skills

Languages	PYTHON, C/C++, JAVA, C#, SQL, BASH
Numerical	Matlab, Mathematica, Scipy
Other	Webots, STochastic Engine for Pathway Simulation (STEPS)
Experience with:	Computational geometry, Machine Learning(unsupervised, supervised and reinforcement) and Optimization, Molecular Simulations via ODEs and PDEs and systems biology, Computer Vision

Education

2015-2020 **Ph.D. candidate in Computational Neuroscience**, *École Polytechnique Fédérale de Lausanne*, Switzerland.
Dissertation Title: Structural Architecture of the Neuronal-Glial-Vascular Systems

2013-2015 **Master in Life Sciences and Technology**, *École Polytechnique Fédérale de Lausanne*, Switcherland.
Orientation of Neuroscience and Neuroengineering, Minor in Computational Neuroscience
Dissertation Title : *Indoor drone navigation via the detection of visual markers*

2006-2013 **Master-Equivalent Degree(5-year) of Applied Physics and Mathematics**, *National Technical University of Athens*, Greece.
Orientation of Applied Physics
Dissertation Title : *Comparative study of nuclear magnetic resonance conventional techniques with nuclear magnetic resonance spectroscopy imaging, single and multiple voxel, in human brain gliomas*

Projects

2015 **Internship/Master Project in Life Sciences and Technology**, *Pix4D SA. under the supervision of Dr. Cristoph Strecha and Prof. Felix Schürmann*, Switzerland.
- implementation of tag detection algorithm
- localization of drone and trajectory prediction
- corrections based on visual feedback from tag detection in 3D space

2014 **Computational Neuroscience : Development of Walking Gait in Webots Mouse Model**, *École Polytechnique Fédérale de Lausanne*, Supervisor : Prof. Marc-Oliver Gewaltig.
- implemented Central Pattern Generator architecture of coupled oscillators for joint movement
- successfully applied genetic optimization strategy to extract the model's parameters to achieve a walking gait
- implemented multiple robot clones that receive genotypes(parameter sets) and evaluate their fitness in parallel

2013 **Philosophy in Life Sciences : A Bionic Brain Through the Looking Glass**, *École Polytechnique Fédérale de Lausanne*, Supervisor : Prof. Christian Sachse.
- argued whether it is possible or not to render a human brain artificial without loosing self-identity in the process

2012-2013 **Internship/Master Project in Applied Physics & Mathematics**, *Euromedica Encephalos*, Greece.
- Quantum Mechanical Analysis of Nuclear Magnetic Resonance Spectroscopy
- Experiments with both conventional MRI and Single/Multiple Voxel MRS techniques in patients with brain gliomas
- Comparison of the above in terms of resolution, specificity and detectability

Work Experience

2014 **Lab Immersion Electrophysiology**, *Laboratory of Neural Microcircuitry*, Switzerland.
- patch-clamping, electrophysiology, staining workflow in Rat Interneurons
- Analysis and feature extraction of recorded cells via eCode
- Morphological Reconstruction of Martinotti Cell with axon in Neurolucida

2013 - 2015 **Part-Time Internship in Subcellular Simulations and toolchain development in Python**, *The Blue Brain Project*, Switcherland.

- systematic and in-depth analysis of long term plasticity through enzymatic pathway dynamical simulations
- generalization of existing kinetic systems using Michaelis-Menten mechanistic theory of enzymes and Non-Essential Cooperation functions
- developed tools in Python for molecular simulations using STEPS, sql and xml models

2013 **Internship in Nuclear Magnetic Resonance Imaging**, *Diagnostic Center "Euromedica Encefalos"*, Greece.

- Application and Assessment of diagnostic ability and accuracy of conventional and advanced MRI techniques

Languages

Greek **Native**, English **Fluent**, French **Basic**

Extracurricular Activities

.

- reading books/watching movies
- writing stories based on simplified concepts from philosophy/mathematics/neuroscience etc.
- teaching myself how to make video games from scratch